DEVELOPMENT OF A FULLY INTEGRATED ACID FRACTURE MODEL

A Dissertation

by

MURTADA SALEH H AL JAWAD

Submitted to the Office of Graduate and Professional Studies of
Texas A&M University
in partial fulfillment of the requirements for the degree of

DOCTOR OF PHILOSOPHY

Chair of Committee,	Ding Zhu
Co-Chair of Committee,	Eduardo Gildin
Committee Members,	Alfred Daniel Hill
	Micah Green
Head of Department,	Duane A. McVay

August 2018

Major Subject: Petroleum Engineering

ABSTRACT

Acid fracturing in heterogeneous carbonate formations is extremely challenging to model. To obtain an acceptable acid penetration distance and fracture surface etched-width profile, a reliable fracture propagation model must be incorporated. Fracture fluid and formation temperatures have an impact on the acid concentration profile, particularly when using weak acids or injecting into dolomite formations. The model provided in this study considers these factors as fractures propagate, in order to obtain the fracture conductivity distribution and evaluate the improvement in well productivity.

The pseudo three-dimensional fracture model developed here is able to provide the domains for the acid dissolution at each time step. A transient acid convection and diffusion equation is solved and the fracture etched-width profile is calculated. An iterative procedure is implemented in a temperature-dependent kinetic model, which stops when both the temperature and acid solutions converge. The model includes an injection of multiple fluid systems that can be either reactive (e.g., straight, emulsified, and gelled acid) or non-reactive (e.g., pad fluid and flush). The model incorporates multiple layer formations with different rock and kinetic properties. Leakoff is calculated for each layer and the wormhole effect is included if reaction takes place. When injection stops, the acid concentration and etching are solved as the fracture closes. As the final etching profile is generated, conductivity is calculated using a correlation that considered formation heterogeneity. Finally, the well productivity is numerically calculated by simulating the reservoir fluid flow and considering the obtained fracture with variable conductivity.

Coupling the fracture geometry and acid models has a significant impact on the final solution. Simulations of acid injection on a non-coupled, constant fracture geometry always overestimate the acid penetration distance and provide inaccurate etched-width profiles. The temperature-dependent kinetic model has a noticeable effect on the etched-width distribution and acid penetration distance for dolomite formations, both are directly related to fracture performance.

The model illustrated here is computationally efficient, which allows for optimizing the design parameters to create a fracture with maximum productivity for a given acid treatment size. More importantly, the optimum acid treatment size for a certain simulated reservoir volume can be determined.

DEDICATION

To my family (especially my Mom)

ACKNOWLEDGEMENTS

I would like to thank Professor Ding Zhu for serving as the chair of my committee during the course of this study. She provided guidance, knowledge, and unconditional support. She was patient and always believed in my ability to finish this work. I would like to extend this appreciation to Professor Dan Hill who served as a committee member. He made sure to discuss my research progress (alongside width Professor Ding Zhu) in a weekly basis, even though he was busy serving as the department chairman. Serving as co-chair, Professor Eduardo Gildin was always available to discuss my approach to tackle numerical problems. His contribution is highly regarded. I am also grateful to Professor Micah Green for serving as a committee member. Progress in my research would not be as smooth without attending his course “Numerical Methods in Chemical Engineering”.

This work would not be as enjoyable without the help of friends and colleagues. I would like to take the chance to thank my colleagues from the acid fracture research group, especially Mateus Schwallbert. Many hours were spent discussing how to improve the developed model. Many thanks go to my close friend Dr. Zuhair Al Yousef. Words cannot express my gratitude toward him.

Finally, I would like to thank the following entities: King Fahd University of Petroleum and minerals (KFUPM) and Saudi ARAMCO. I am fully sponsored by them to earn a Ph.D. degree and then return to serve my country.

CONTRIBUTORS AND FUNDING SOURCES

This work was supervised by a dissertation committee consisting of Professor Ding Zhu who served as committee chair, Professor Eduardo Gildin who served as co-adivsor, Professor Dan Hill of the Department of Petroleum Engineering, and Professor Micah Green of the Department of Chemical Engineering. The productivity model was provided by Mateus Schwallbert. I am fully sponsored by the Saudi Arabian Cultural Mission (SACM).

TABLE OF CONTENTS

Page

LIST OF FIGURES

Page

LIST OF TABLES

CHAPTER I

INTRODUCTION

1.1 Acid Fracturing Overview

Acid fracturing is a well stimulation method performed in carbonate formations. Such operations consist of injecting viscous pad fluid at high pressure to initiate and propagate a fracture. Then, acid is injected to etch the fracture walls in non-uniform patterns. In many cases, acid and pad fluids are injected in alternating stages. A water flush is usually the final stage, because it reduces equipment corrosion by driving the acid deeper inside the fracture. When fluid injection stops, the fracture pressure drops as fluids leak out; this allows for fracture closure. However, asperities and channels created at the fracture surfaces from the acid differential etching prevent the fracture from completely achieving closure. The result is a conductive path along which reservoir fluids can flow from the formation's matrix to the wellbore.

Proppants, which are small sand or bauxite particles, can serve as an alternative to the acid stage. These solid materials are able to hold the fracture open after closure, providing conductivity. Proppants are usually favored over acid injection because the outcome is easier to predict and conductivity can be better maintained at high closure stresses. However, acid is a cheaper option that is easier to pump and does not suffer from proppants' complications with screen out. Acid fracturing is avoided in homogeneous or deep carbonate formations where fracture conductivity can easily be diminished. Conversely, an engineer may favor acid fracturing when treating a naturally fractured formation in order to create a network of conductive pathways. A complete study of the formation properties should be performed to determine the more applicable option.

Acid can also be injected at lower rates, resulting in wormholes that extend from the wellbore. This process is called matrix acidizing, and occurs when the treatment pressure does not exceed the formation breakdown pressure. This is most often used when wormholes are believed to extend beyond the damage zone, in order to bypass near wellbore damage. In cases of severe damage, acid fracturing can be an option for bypassing formation damage, given that wormhole radii cannot extend beyond the damage radius.

The level of improvement in wellbore productivity that results from acid fracturing is determined by the distance of acid penetration and distribution of conductivity. Retarded acid systems can create longer fractures with lower conductivity; this is in contrast to straight acid, which provides shorter, more highly conductive fractures. For a given acid treatment volume, there is an optimum acid penetration distance and conductivity distribution that are functions of the formation properties, especially formation size and permeability. Conductivity distribution can be estimated from the obtained acid etched-width distribution; this is accomplished using a conductivity correlation.

The goal of any acid fracturing simulator is to estimate the acid etched-width profile along the acid penetration length. This requires an understanding of the fracture geometry propagation, acid convection and diffusion, reaction kinetics, and fracture temperature changes occurring throughout the process. Difficulties with modeling acid fracturing operations arise from the acid reactivity with a seldom homogenous formation. Acid creates wormholes along fracture surfaces, resulting in leakoff behavior that is difficult to predict and that serves as a significant input when calculating the fracture geometry. The minerology distribution along the fracture length can be difficult to measure, often resulting in inaccurately simulated etched-width profiles. Even if a precise etched-width profile can be obtained, the estimated conductivity from the conductivity correlations available from the literature is at best, questionable. However, this should not discourage the modeling of acid fracturing operations since it provides a qualitative understanding of the process and quantitatively educated guesses with regards to outcomes.

Early work on quantifying acid penetration distance and the amount of dissolved rock was experimental. Acid was injected into fractured core samples oriented either vertically or horizontally. Based on this foundational work, correlations were developed between the acid penetration distance and spent acid concentration (Barron et al., 1962). Later, the temperature effects on acid spending were studied and the correlations modified accordingly (Coulter et al., 1974). However, the developed correlations were only valid for the types of rock and acid used at the lab's specified temperature and concentration.

Later, analytical methods were introduced to design acid fracturing jobs. This was possible because of the development of Terrill's (1965) heat transfer analytical solution to fluid flow between parallel porous plates. Williams and Nierode (1972) used Terrill's method to solve for the acid concentration, providing a procedure for calculating acid penetration distance and acid etched-width; from these values, they were able to estimate improvement in the well's productivity. Roberts and Guin (1975) provided both analytical and numerical methods to account for finite reactivity, a process that considers the reactivity of weak acids and dolomite formations.

Improvements in computational power encouraged the development of numerical models, eliminating many restrictive assumptions. Lo and Dean (1989) developed a one-dimensional (1D) acid solution coupled with a multiple-fluid geometry model. Settari et al. (2001) introduced a more comprehensive transient two-dimensional (2D) acid model, where the acid concentration was resolved along the fracture width. A three-dimensional (3D) acid model had earlier been suggested by Romero et al. (2001), based on an assumed 3D analytical fluid flow velocity profile. Oeth et al.

(2014) used Mou et al.’s (2010) approach to develop a fully 3D numerical acid model using the Semi-Implicit Method for Pressure Linked Equations (SIMPLE) algorithm to resolve the acid velocity profile.

Combining a fully numerical 3D acid model with fracture propagation, heat transfer, and reservoir models can be numerically unstable and computationally expensive. Therefore, an efficient and computationally stable pseudo-3D (P3D) acid model was developed in this research to accomplish the same goal. The model resolves acid concentration in all fracture dimensions and provides a 2D fracture surface etching profile. Optimizing the design parameters to create the maximum well productivity using the developed model is time efficient. The model also simulates acid spending and heat transfer during fracture closure; other models do not take these parameters into consideration.

1.2 Literature Review

Acid has been used to improve well performance for more than a century. In 1895, Standard Oil Company used hydrochloric acid to stimulate the Lima formation in Ohio. Acid fracturing was first observed in 1935, when Schlumberger injected acid at a pressure higher than the formation breakdown pressure (Kalfayan, 2007). Since then, acid fracturing has been a common practice for well stimulation. However, it did not receive substantial research attention until the 1960s.

1.2.1 Fracture Conductivity Correlations

A critical phenomenon that researchers are trying to understand is the relationship between a fracture surface etching profile and its ability to conduct fluids. Nierode and Kruck (1973) provided a conductivity correlation based on 25 lab experiments on small core samples that were cut in tension to create uneven surfaces. The correlation related fracture conductivity, wk_f, to the dissolved rock equivalent conductivity, $DREC$, rock impediment strength, RES, and formation closure stress, σ_c. The Nierode-Kruk conductivity correlation can be found in Equations 1.1 to 1.3.

$$wk_f = C_1 \exp(-C_2\sigma_c) \tag{1.1}$$

$$C_1 = 0.265\ (DREC)^{0.822} \tag{1.2}$$

$$C_2 * 10^3 = \begin{Bmatrix} 19.9 - 1.3\ln(RES) \;\; 0 < RES < 20{,}000 psi \\ 3.8 - 0.28\ln(RES)\; 20000 \le RES \le 500{,}000\ psi \end{Bmatrix} \tag{1.3}$$

This correlation assumes that fracture conductivity is proportional to the amount of etched rock, but that the value exponentially declines as the formation closure stress increases. This correlation is widely accepted in the industry. Many correlations developed subsequently use the same model but with different experimentally determined constants.

Other researchers developed conductivity correlations based on theoretical conclusions. Gangi (1978) showed that the cubic root of the fracture conductivity is a function of the closure stress, to an exponent determined based on the fracture surface asperities distribution. Walsh (1981) found that the cubic root of the fracture conductivity logarithmically declines with closure stress. Gong et al. (1999) developed a theoretical conductivity correlation that considers both the rock’s surface roughness and mechanical properties. Constants in the correlation were tuned by fitting 55 acid fracture experiments. Pournik et al. (2009) ran 62 acid fracture experiments and selected those showing surface roughness patterns as a means of updating the Nierode-Kruk correlation constants.

Understanding fracture conductivity requires a consideration of the stochastic nature of formation rocks. Deng et al. (2012) stated that heterogeneity in formation mineralogy and permeability is a major factor in differential etching. Permeability distribution is represented by the correlation length in the horizontal direction, $\lambda_{D,x}$, and vertical direction, $\lambda_{D,z}$, as well as the normalized permeability standard deviation, σ_D. Natural bedding makes the horizontal correlation length larger than the vertical. Higher fracture conductivity can be expected when $\lambda_{D,x}$ and σ_D are high but $\lambda_{D,z}$ is low, a situation in which channels are believed to develop and become preserved. Minerology distribution is represented by the percentage of calcite and dolomite in the formation. The fracture conductivity increases as the percentage of calcite increases, but it will begin to decrease when the calcite content is greater than 50%. These statistical parameters can be used to calculate constants from the Nierode-Kruk correlation.

1.2.2 Acid Fracture Design

One of the earliest attempts at designing acid fracturing jobs was made by Williams and Nierode (1972). Their method depended on the analytical heat transfer solution for fluid flow between parallel porous walls (Terrill, 1965). The acid mass balance equation, analytical solution, and Peclet number, N_{Pe}, are shown in Eqs. 1.4 to 1.6:

$$u(x,y)\frac{\partial C_A}{\partial x} + v(x,y)\frac{\partial C_A}{\partial y} = D_A\frac{\partial^2 C_A}{\partial y^2} \tag{1.4}$$

$$\frac{\bar{C}}{C_i} = \sum_{n=0}^{\infty} G_n(1-\frac{x}{x_f})^{2\lambda_n^2/3N_{Pe}} \tag{1.5}$$

$$N_{Pe} = \frac{\bar{v}_L\bar{w}}{2D_A} \tag{1.6}$$

where x is the fracture's length direction, y is the fracture's width direction, u is the velocity in the x direction, v is the velocity in the y direction, C_A is the acid concentration, D_A is the effective mixing acid diffusion coefficient, $\bar{C}$ is the average acid concentration, C_i is the initial acid concentration, x_f is the fracture half-length , λ_n and G_n are eigenvalues, $\bar{v}_L$ is the average leakoff velocity, and $\bar{w}$ is the fracture's average width. A graphical form of the solution at different N_{Pe} values is presented in Figure 1.1. At low N_{Pe} values, the diffusive forces dominate and acid concentration quickly diminishes, while at high N_{Pe} values the convective forces dominate and acid concentration is preserved to travel longer distances.

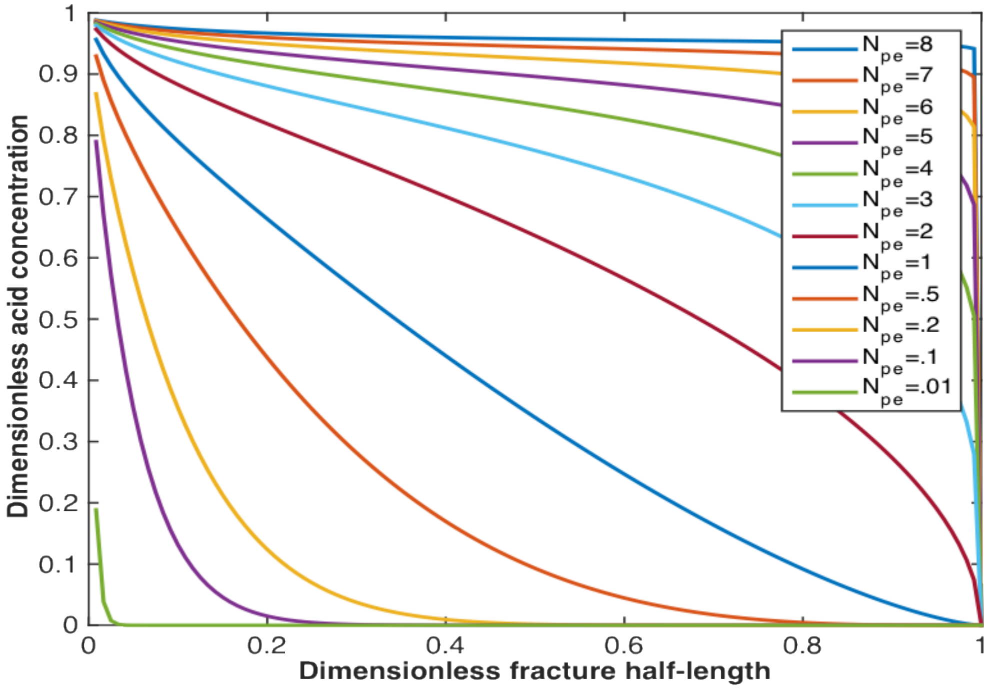

Figure 2.1: Terrill's acid solution at different Peclet numbers adapted from Schechter (1992).

Berman's (1953) solution was used by Terrill to obtain velocity profiles in the x and y directions, satisfying both the continuity and momentum balance equations. The approach used by Williams and Nierode assumed a laminar incompressible Newtonian fluid, constant width, uniform leakoff velocity, steady state condition, and infinite acid reaction rate at the fracture walls.

Roberts and Guin (1975) used the same approach to design acid fracturing operations, but instead of assuming a zero concentration at the fracture surfaces, they introduced the boundary condition shown in Eq. 1.7:

$$D_A \frac{\partial C_A}{\partial y} = k_r {C_w}^{n_r} \tag{1.7}$$

where k_r is the reaction rate constant, n_r is the reaction exponent, and C_w is the acid concentration at the fracture walls. The boundary condition states that acid reaches the fracture walls by diffusion to react at the fracture surfaces. The acid reaction is called “mass transfer limited” when the reaction rate is the fastest step, and “reaction rate limited” when the acid mass transfer rate is faster than the reaction rate. By introducing this boundary condition, it is possible to design for dolomite formations and weak acid reactions. The acid solution is averaged in 1D by introducing the mass transfer coefficient, k_g, presented in Eq. 1.8:

$$k_g = D_A \frac{\partial C_A}{\partial y} / (C_w - \bar{C}) \tag{1.8}$$

An analytical solution is derived for a first order reaction under constant leakoff; otherwise, the finite difference method is used to solve for the acid concentration. Lo and Dean (1989) used Robert and Guin’s approach but assumed zero concentration at the fracture walls. Their major contribution was their modeling of multiple fluid injections, which is common practice in acid fracturing operations. Settari (1993) eliminated the steady state assumption by introducing the transient term to both continuity and acid mass balance equations. The wormhole effect is included by varying the leakoff velocity, accordingly.

Settari et al. (2001) introduced a 2D acid fracture model by resolving the acid concentration in the fracture width dimension. These researchers concluded that the 1D model consistently underestimated the acid etched-width profile. Romero et al. (2001) introduced a 3D acid fracture model. The velocity profile they suggested was analytical; the height dimension velocity profile was assumed to be similar to that of the fracture length dimension. Mou et al. (2010) numerically solved for the velocity profile applying the SIMPLE algorithm in a 3D non-regular fracture shape.

The velocity profile was required to obtain the acid concentration profile in three dimensions, from which they created an intermediate-scale acid fracture model. Oeth et al. (2014) modified Mou's model to produce a field scale acid fracture model. However, it was not coupled with the fracture propagation and heat transfer models. For such computationally rigorous models, numerical stability can be an issue. Aljawad et al. (2016) used Oeth model to study which fluid system should be selected to acid fracture low and high permeability formations. Lyons et al. (2016) developed a pore-scale acid fracture model using a lattice Boltzmann method to solve for the acid concentration and temperature profiles. The objective of their model was to capture heterogeneity effects on the dissolution patterns.

The acid etched-width profile can be analytically calculated by assuming total consumption of the acid at the fracture surfaces (Schechter, 1992). The solution is derived by applying Terrill's solution which assumed the reaction rate is infinite. It was observed that the higher the Peclet number, the more uniform the etching is along the fracture, as shown in Figure 1.2. Etched-width distribution as a function of distance is shown in Eq. 1.9:

$$w_i = \frac{\beta q_i t_e C_i}{2\rho h_f (1-\varphi)} \sum_{n=0}^{\infty} G_n \left(1 + \frac{2\lambda_n^2}{3N_{Pe}}\right)\left(1 - \frac{x}{x_f}\right)^{2\lambda_n^2/3N_{Pe}} \tag{1.9}$$

where w_i is the ideal fracture width, q_i is the fluid injection rate, h_f is the fracture height, ρ is the fluid density, φ is the formation porosity, t_e is the total time of acid injection, and β is the gravimetric dissolving power. With the development of acid fracture numerical models, the etching profile could be calculated numerically to account for the volume of acid consumed creating wormholes out of the fracture surfaces.

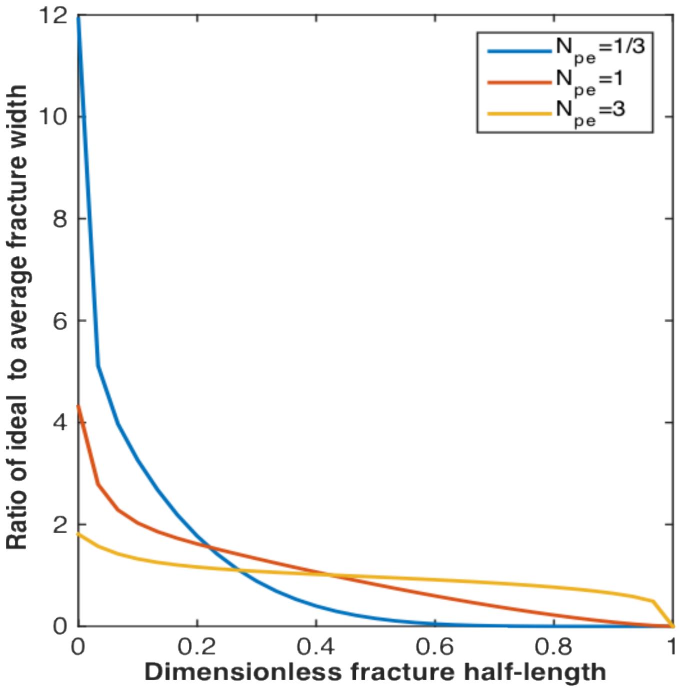

Figure 1.2: Ideal fracture widths at different Peclet numbers adapted from Schechter (1992).

1.2.3 Fracture Temperature Models

Realizing the significance of fracture temperature modeling, Dysart and Whitsitt (1967) introduced one of the earlies analytical models. Their 1D fracture temperature model neglects the transient heat accumulation term and assumes non-reactive fracture fluids. The fracture fluid leakoff is assumed to be constant along the fracture length. To evaluate the heat flux from the formation to the fracture, a decoupled formation-transient heat conduction equation is solved, assuming a constant fracture temperature. One drawback of the model is that it neglects the cooling effect of the leaked fracture fluid on the formation. Whitsitt and Dysart (1969) developed a more rigorous fracture temperature solution that requires numerical integration. The updated model assumes that the fracture fluid leakoff rate increases linearly towards the fracture tip. The formation and fracture heat transfer equations are coupled to account for the fracture fluid cooling effect resulting from leakoff. Wheeler (1969) solved the heat transfer equation for hot fluid injection in a vertical fracture. The solutions provided in his work account for fracture heat accumulation and assumes that the heat fluxes towards the formation.

Lee and Roberts (1980) presented a heat transfer model that considers the heat of reaction effects arising from the exothermic acid reactions occurring at carbonate fracture surfaces. The model neglects fracture heat accumulation (the transient term) and uses Whitsitt and Dysart’s heat flux equation to account for heat transfer from the formation to the fracture. At the fracture walls, the heat flux from the formation (in addition to the heat of reaction) is equated to the heat conducted towards the fracture. The problem is averaged in 1D by introducing the heat transfer coefficient in the fracture width direction. The researchers concluded that the heat of the reaction effect was significant, more than 40 ^{o}C, and must be included to correctly model the acid fracturing operations. Guo et al. (2014) investigated the heat of reaction as a function of temperature and pressure. They used the same model introduced by Lee and Roberts, but included the effects of the variable heat produced by such reactions. Their approach showed that the heat of reaction could raise the fracture temperature in certain position up to 15 ^{o}C, which is significantly lower than what Lee and Roberts predicted.

1.2.4 Fracture Geometry Models

Early fracture geometry models assumed a constant fracture height and only allowed for the fracture length and width to change. Perking and Kern (1961) incorporated Sneddon’s (1946) elasticity equation into the fluid pressure drop equation inside an ellipse to develop their 2D width equation. Nordgern (1972) modified Perking and Kern’s (1961) model, including the fluid loss and accumulation effects on the fracture width; the result was the well-known PKN model. Khristianovic and Zheltov (1955) and Geertsma and de Klerk (1969) produced a model (KGD), a

2D approach that assumes horizontal plane strain that is contrary to the vertical plane strain assumed in the PKN model. When the fracture half-length is longer than the height, the PKN model consistently produces narrower fracture widths than does the KGD model.

Fracture height can be assumed constant only when the confining stress contrast approaches infinity. The need to determine the fracture height for non-confined formation layers led to the development of the P3D fracture propagation model. This type of model uses the KGD model to describe the growth of the fracture height, while applying the PKN approach to estimate the lateral growth (Cleary, 1980; Meyer, 1986). More rigorous 3D fracture propagation models were subsequently developed and numerically solved using finite or boundary element methods (Cleary et al., 1983; Morita et al., 1988).

1.2.5 Fracture Productivity Evaluation

In the production life of a reservoir, fluid flow can be transient, pseudo-steady, or steady state. The flow is considered transient early in the production time, until the fluid pressure drop reaches the reservoir boundaries. After that, the flow is considered pseudo-steady state, a condition in which the reservoir pressure drops at a constant rate. Nevertheless, if a pressure support exists or is provided to the reservoir (such as by a water aquifer or water injection), the flow is described as steady state, where no significant changes in reservoir pressure are observed.

Improvement in wellbore productivity is the incentive behind creating fractures in reservoirs. Primarily, a fracture's acid penetration distance and conductivity, wk_f, determine the level of enhancement that can be realized. McGuir and Sikora (1960) provided a graphical method of determining improvement in productivity, assuming a pseudo-steady flow and uniform vertical fracture conductivity. By estimating the ratios of fracture length to drainage radius and fracture conductivity to formation permeability, the improvement in productivity can be estimated.

Evaluating acid fracture productivity using the above method may not always be accurate, though, because fracture conductivity is seldom uniform. Raymond and Binder (1967) derived a productivity formula that considers variable fracture conductivity under a pseudo-steady flow. When reservoir permeability is low, it may take a long time for the flow to reach a pseudo-steady state. In such scenarios, numerically generated type curves are used to estimate well productivity, assuming an infinite level of fracture conductivity (Wattenbarger et al., 1998).

1.3 Research Objectives

The objective of this study is to develop a fully integrated acid fracture model that can predict well performance for acid fractured wells. This engineering tool will be used to determine the optimum acid treatment volume and how to achieve better fluid placement in a formation. The model consists of geometry, acid, heat transfer, and reservoir models that have been integrated to achieve this objective. The integrated model is computationally efficient in a manner that does not jeopardize the solution’s accuracy.

To obtain a correct solution, it is necessary to couple fracture geometry propagation with the acid model at each time step. The goal is to quantify the difference in acid solutions between the coupled and constant geometry assumptions. The geometry model was developed to handle multiple fluid injections, such as viscous pads and water flushes, both before and after acid injection. The possible effects of each on the distance of acid penetration and etched-width distribution will be examined below.

The heat transfer model was incorporated to correctly model the temperature-dependent reaction rate of acids with dolomite formations. The goal was to study temperature’s effects on the etching profile and level of acid penetration. The effects the heat of reaction has on the temperature and acid solutions was also considered in this study, as was the importance of the pad fluid's cooling on the level of reactivity during the acid stage.

Predicting and comparing wellbore performances for different acid fracture designs will assist in determining the optimum design parameters. This is possible only by joining the reservoir simulator to the acid fracture model; it is from there that any improvement in productivity can be calculated. The integrated model determines the optimum acid treatment volume, which is a significant parameter in acid fracture design.

CHAPTER II

MODEL DEVELOPMENT [*]

The approach used in this research integrates the acid model with the fracture propagation, heat transfer, and reservoir models. Figure 2.1 illustrates the workflow of the approach. After reading the input data, the fracture dimensions were calculated, providing a domain for the acid solution. Iterations between the fracture geometry and leakoff coefficients were performed until convergence. The leakoff coefficients were first calculated based on an assumed fracture height, then updated according to the new height calculated from the geometry file. Convergence was declared when both the fracture height and leakoff coefficients showed no changes in their values. The acid concentration and temperature profiles were iteratively resolved along the fracture dimensions until the solution converged. This procedure was performed at each time step, until the final injection time was reached.

An analytical solution was first used to speculate on the temperature profile from which the reaction rate constant would be determined. Then, the acid solution was calculated, feeding the temperature model with the reaction rate. Next, the heat of reaction was evaluated based on the calculated reaction rate, in order to update the temperature profile. When the difference between two consecutive concentration and temperature solutions was less than a certain error percentage, convergence was declared. The acid concentration and temperature profiles were also computed at each time step during the fracture closure time. Then, the fracture conductivity was estimated from the obtained fracture surface etching profile using Mou-Deng correlation (Deng et al., 2012).

---

[*] Part of this section is reproduced with permsionss from “Temperature and Geometry Effects on the Fracture Surfaces Dissoution Patterns in Acid Fracturing” by Aljawad, M.S., Zhu, D. and Hill, A. D. 2018. Copyright 2018, Society of Petroleum Engineers. Further reproduction prohibited without permission.

Finally, the reservoir model was used to calculate the productivity improvement from the given fracture conductivity distribution.

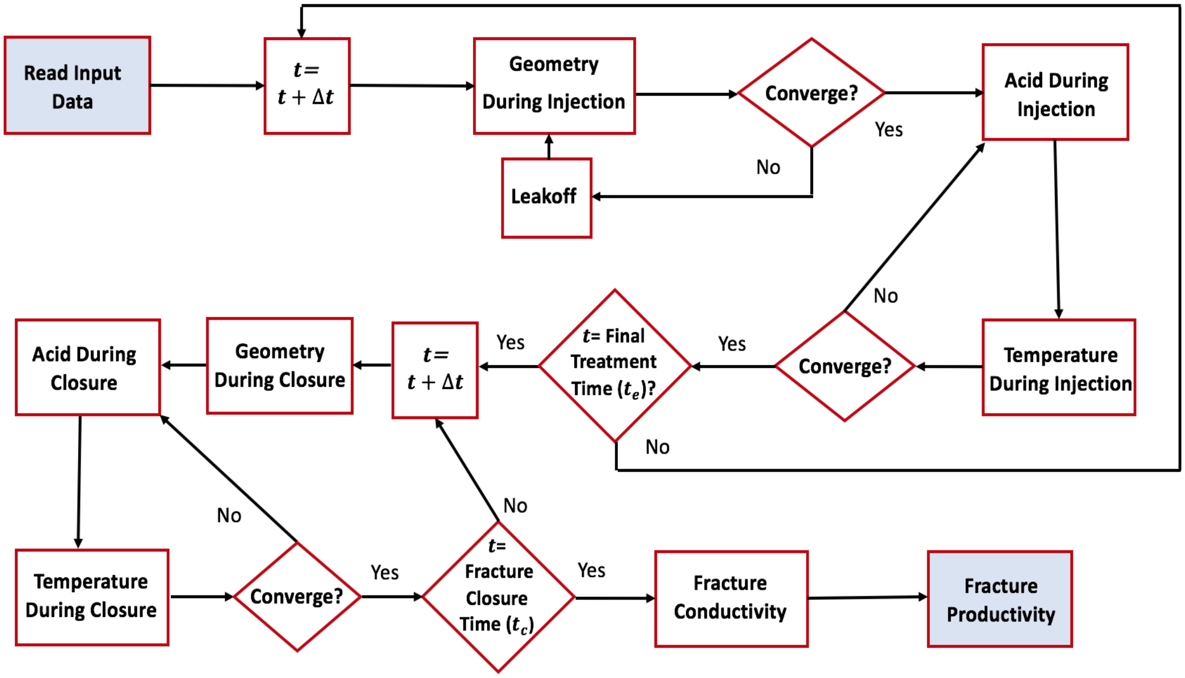

Figure 2.1: Algorithm for the developed model.

2.1 Fracture Propagation Model

An analytical pseudo-three dimensional (P3D) fracture propagation model was deployed to obtain the fracture half-length, x_{f}, maximum width at entrance, $w_{\max,0}$, height, h_f, net pressure, P_{net}, and leakoff coefficient, C_{L}, at each time step. The following sections describe the major elements of the geometry model.

2.1.1 Fracture Width

A PKN model was implemented to calculate the fracture width (see Fig. 2.2). The approach was derived by substituting Sneddon’s (1946) elasticity equation, assuming a vertical plane strain, into

Lamb's (1932) fluid pressure drop equation inside an elliptical-shaped body. Sneddon, Lamb, and the plane strain modulus, $\grave{E}$, equations are shown in Eqs. 2.1 to 2.3:

$$w_{max,0} = \frac{2h_f P_{net}}{\grave{E}} \tag{2.1}$$

$$\frac{dP_{net}}{dx} = -\frac{64\mu q_i}{\pi w_{max,0}^3 h_f} \tag{2.2}$$

$$\grave{E} = \frac{E}{1-v^2} \tag{2.3}$$

where μ is the apparent fluid viscosity, q_i is the fluid injection rate, E is Young's modulus, and v is Poisson's ratio. The substitution resulted in the following equation:

$$\frac{dP_{net}}{dx} = -\frac{8\mu q_i \grave{E}^3}{\pi h_f^4 P_{net}^3} \tag{2.4}$$

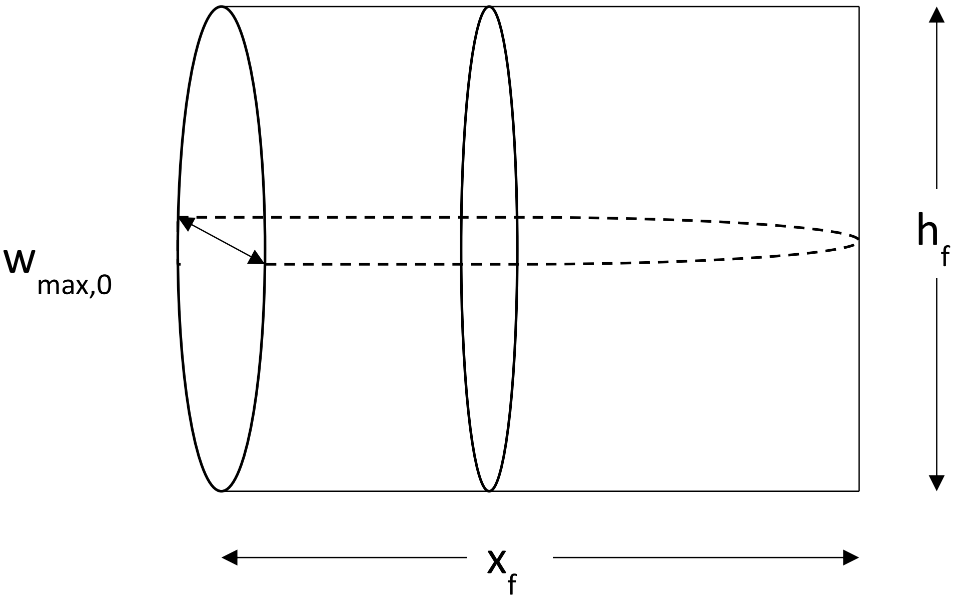

Figure 2.2: A PKN-shaped fracture adapted from Nordgren (1972).

By separating the variables, integrating over the fracture half-length, and then back-substituting Eq. 2.1 into the integrated equation, the Perkin-Kern (PK) width equation was obtained (Eq. 2.5). The net pressure at the fracture tip was assumed to be zero.

$$w_{max,0} = 3.57 * \left(\frac{\mu q_i x_f}{\grave{E}}\right)^{\frac{1}{4}} \tag{2.5}$$

Nordgren (1972) investigated the effects of fluid accumulation and loss on fracture width. The asymptotic solution to the long-time representation of large fluid loss resulted in changing the constant from 3.57 to 3.27 (Eq. 2.6).

$$w_{max,0} = 3.27 * \left(\frac{\mu q_i x_f}{\grave{E}}\right)^{\frac{1}{4}} \tag{2.6}$$

The Perkin-Kern-Nordgren equation (PKN) equation assumes a constant fracture height, zero net pressure at the fracture tip, and an elliptical fracture cross-section. Most of the fracturing fluids in this research were far from ideal; hence, a width equation for power law fluids was used. This was obtained by substituting an effective viscosity, μ_e, for the apparent viscosity in the PKN width equation (Valko and Economides, 1995). The power law fluid, effective viscosity, and non-Newtonian PKN width equation are shown in Eqs. 2.7 to 2.9:

$$\tau = K\dot{\gamma}^n \tag{2.7}$$

$$\mu_e = 2^{n-1} * \pi^{-1} \left[\frac{1 + (\pi - 1)n}{n}\right]^n K w_{max}^{1-n} * u_{avg}^{n-1} \tag{2.8}$$

$$\begin{aligned} w_{\mathrm{max,0}} = 9.15^{\frac{1}{2n+2}} * 3.98^{\frac{n}{2n+2}} * \left(\frac{1 + 2.14n}{n}\right)^{\frac{n}{2n+2}} K^{\frac{1}{2n+2}} \\ * \left(\frac{{q_i}^n h_f^{1-n} x_f}{\grave{E}}\right)^{\frac{1}{2n+2}} \end{aligned} \tag{2.9}$$

where τ is the shear stress, $\dot{\gamma}$ is the shear rate, K is the flow consistency index, n is the flow behavior index, and u_{avg} is the average fluid velocity. To obtain the average fracture width, $\overline{w}$, the fracture width, w, was integrated over the fracture height and length dimensions and divided by the fracture surface area (Eq. 2.10).

$$\overline{w} = \frac{1}{x_f h_f} \int_0^{h_f} \int_0^{x_f} w(x,z) dx dz = 0.628 * w_{max,0} \tag{2.10}$$

2.1.2 Material Balance

Assuming a constant fracture fluid density, the material balance became a volume balance over an element of the fracture (see Fig. 2.3). The 1D material balance consisted of three parts:

$$\begin{bmatrix} Volume \\ of\ Fluid \\ in \end{bmatrix} = \begin{bmatrix} Volume \\ of\ Fluid \\ out \end{bmatrix} + \begin{bmatrix} Volume \\ of\ Fluid \\ Accumulated \end{bmatrix} \tag{2.11}$$

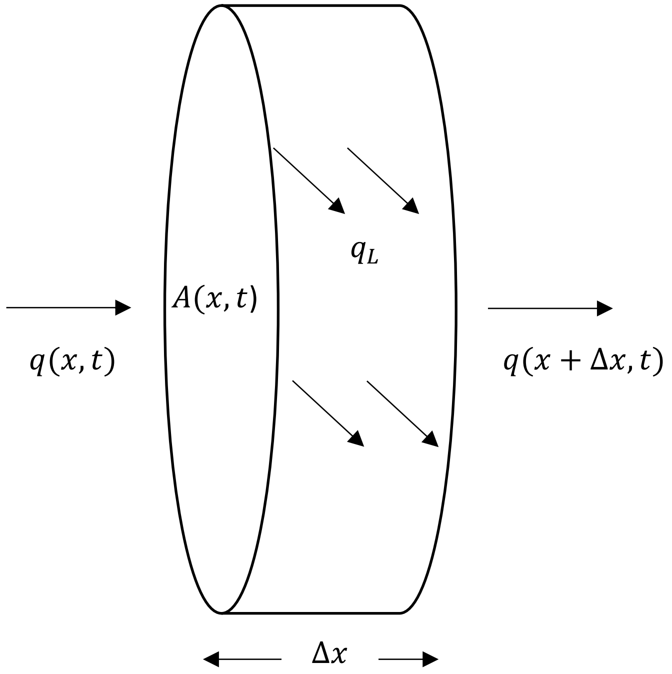

Figure 2.3: Material balance over a small element of the fracture adapted from Schechter (1992).

The volume of the fluid injected into the element over a certain time interval was:

$$\begin{bmatrix} Volume \\ of\ Fluid \\ in \end{bmatrix} = q(x,t)|_x\, \Delta t \tag{2.12}$$

where q is the flow rate and t is time. The volume of the fluid leaving the element by convection and leaking over the same time interval was:

$$\begin{bmatrix} Volume \\ of\ Fluid \\ out \end{bmatrix} = q(x,t)|_{x+\Delta x}\, \Delta t + q_L(x,t)\, \Delta x\, \Delta t \tag{2.13}$$

where q_L is the leakoff rate per unit length. The amount of fracture volume increase attributable to fluid accumulation was:

$$\begin{bmatrix} Volume \\ of\ Fluid \\ Accumulated \end{bmatrix} = A(x,t)|_{t+\Delta t}\, \Delta x - A(x,t)|_t\, \Delta x \tag{2.14}$$

The mathematical expression of the material balance was:

$$\begin{gathered} q(x,t)|_x\, \Delta t = [q(x,t)|_{x+\Delta x}\, \Delta t + q_L(x,t)\, \Delta x\, \Delta t] \\ + [A(x,t)|_{t+\Delta t}\, \Delta x - A(x,t)|_t\, \Delta x] \end{gathered} \tag{2.15}$$

If the equation is rearranged, divided by Δx and Δt, and the limit determined to be approaching zero, the differential form of the material balance is:

$$\frac{\partial q}{\partial x} + q_L + \frac{\partial A}{\partial t} = 0 \tag{2.16}$$

In this research, Carter’s equation (Carter, 1957) was then used to evaluate the fluid loss, as follows:

$$q_L = \frac{2C_L h_f}{\sqrt{t-\tau(x)}} \tag{2.17}$$

where C_L is the leakoff coefficient, and $\tau(x)$ is the time when the fracture reached position x.

To obtain the analytical form of the material balance, it was integrated over the fracture half-length, x_f, and injection time, t_e.

$$\int_0^{t_e}\int_0^{x_f}\frac{\partial q}{\partial x}dxdt + \int_0^{t_e}\int_0^{x_f}q_L\,dxdt + \int_0^{t_e}\int_0^{x_f}\frac{\partial A}{\partial t}dxdt = 0 \qquad (2.18)$$

To integrate the first term, the flow rate, q, was assumed to be a function of the position, but constant over time. Also, the flow rate at the fracture tip was zero, resulting in:

$$\int_0^{t_e}\int_0^{x_f}\frac{\partial q}{\partial x}dxdt = \int_0^{t_e}[\,q|_{x_f} - q|_0]dt = \, -q|_0\, t_e = \, -q_i/2\; t_e \qquad (2.19)$$

The second term was evaluated using Nolte's approach (Nolte, 1986), as follows:

$$\int_0^{t_e}\int_0^{x_f}q_L\,dxdt = 2x_f h_f(\kappa C_L\sqrt{t_e}) \qquad (2.20)$$

where κ is the opening time distribution factor. The third term was evaluated assuming the fracture cross-sectional area, A, was initially zero, resulting in:

$$\int_0^{x_f}\int_0^{t_e}\frac{\partial A}{\partial t}dtdx = \int_0^{x_f}[A|_{t_e} - A|_0]dx = \int_0^{x_f}\frac{\pi}{4}w_{max}(x)h_f\,dx = \,\bar{w}x_f h_f \qquad (2.21)$$

Putting the integrated terms together, the analytical solution as a function of time, t, and position, x, became:

$$\frac{q_i}{2}t - 2xh_f\big(\kappa C_L\sqrt{t_e} + S_p\big) - \bar{w}xh_f = 0 \qquad (2.22)$$

where S_p is the spurt loss coefficient that accounts for the initial amount of fluid lost before the formation of fracture fluid cake on the fracture surfaces.

2.1.3 Fracture Height Calculation

The fracture height was estimated at each time step by applying Liu and Valko's (2015) approach. The lower and upper tips of the fracture height will propagate if the stress intensity factor at the fracture tips, K_I, is greater than the bounding layers' toughness, K_{IC}. Thus, the fracture's upper and lower tip locations, and hence fracture height, were calculated as follows:

$$K_{I+} - K_{IC+} = 0 \tag{2.23}$$

$$K_{I-} - K_{IC-} = 0 \tag{2.24}$$

where the subscript (+) refers to the lower tip, and (-) refers to the upper tip. The definition of the stress intensity factor was:

$$K_{I+} = \frac{1}{\sqrt{\pi c}} \int_{-c}^{+c} P_{net}(z) * \sqrt{\frac{c+z}{c-z}}\, dz \tag{2.25}$$

$$K_{I-} = \frac{1}{\sqrt{\pi c}} \int_{-c}^{+c} P_{net}(z) * \sqrt{\frac{c-z}{c+z}}\, dz \tag{2.26}$$

where z is the position at the fracture height direction, and c is the fracture half-height to be estimated. The fracture pressure at any position was calculated by subtracting or adding the hydrostatic column difference to the reference pressure, P_{ref}. The reference depth, d_{ref}, was selected to be at the center of the pay zone and the middle fracture location, d_{midf}, was located at $z = 0$ (see Fig. 2.4). The fracture net pressure was calculated as follows:

$$\begin{aligned} P_{net}(z) &= \rho g z + P_{midf} - \sigma_i \\ &= \rho g z + \left(P_{ref} + \left(d_{midf} - d_{ref}\right)\rho g\right) - \sigma_i = mz + b_i \end{aligned} \tag{2.27}$$

where P_{midf} is the pressure at the center of the fracture, ρ is the fluid density, g is the gravity acceleration, σ_i is the ith formation layer's minimum horizontal stress, m is ρg, and b_i is $\left(P_{ref} + \left(d_{midf} - d_{ref}\right)\rho g\right) - \sigma_i$. The net pressure expression (Eq. 2.27) was substituted into the stress intensity factor formula (Eq. 2.25) and analytically integrated to obtain:

$$Int(z,b_i) = \frac{1}{\sqrt{\pi c}}\int_{-c}^{z}(mz+b_i) * \sqrt{\frac{c+z}{c-z}}\,dz$$

$$= \frac{\left(-\sqrt{(c-z)\,(c+z)}\,\left(2b_i + m(2c+z)\right) + 2c(2b_i + cm)ArcSin\left(\frac{\sqrt{\frac{c+z}{c}}}{\sqrt{2}}\right)\right)}{2\sqrt{\pi c}} \tag{2.28}$$

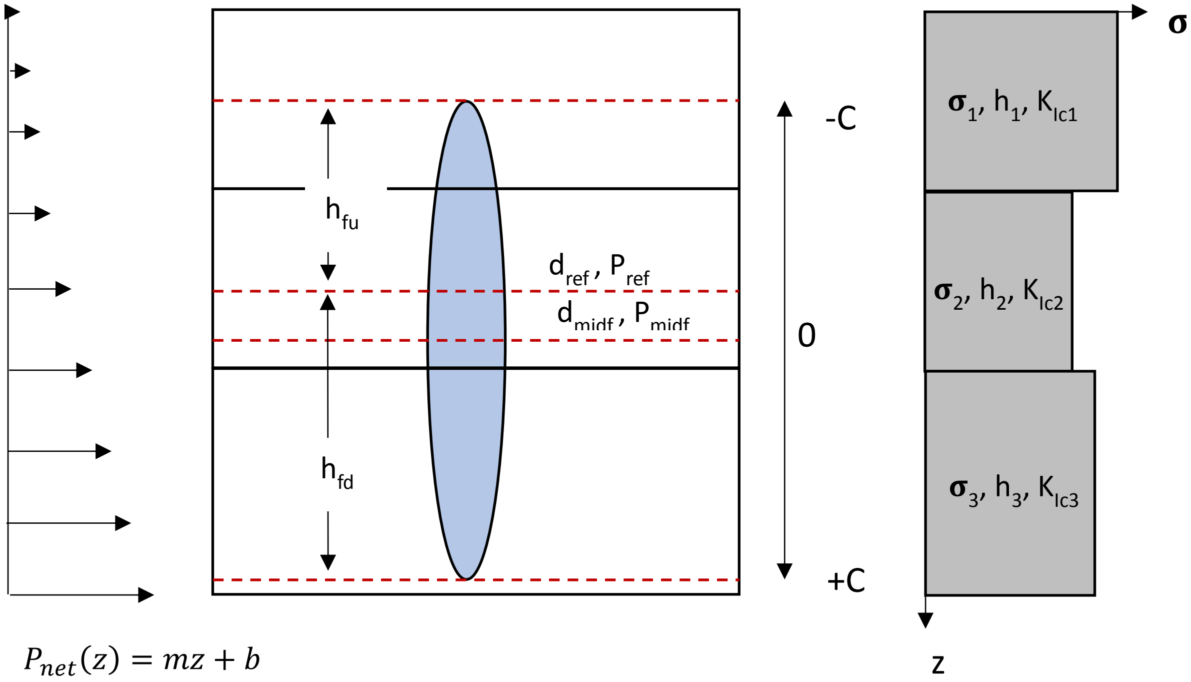

Figure 2.4: Fracture in a multi-layer formation adapted from Liu and Valko (2015).

To evaluate the stress intensity factor for the lower tip of a multi-layer formation, the integration was evaluated as follows:

$$K_{I+} = \sum_{i=1}^{n}\left(Int(z2_i, b_i) - Int(z1_i, b_i)\right) \tag{2.29}$$

where $z1_i$ is the upper boundary of the ith layer, $z2_i$ is the lower boundary of the same layer, and n is the number of layers. For the layers containing the fracture's upper and lower tips, the tip location needed to be substituted into the integral formula (Eq. 2.29) instead of the layer boundary location. The same approach was used to evaluate the upper tip stress intensity factor.

2.1.4 Multiple Fluid Injection

To correctly model the acid fracturing operations, the geometry model had to be able to handle multiple fluid injections. In this section, the approaches for three different fluids (pad, acid, and flush) are shown. To be able to handle the problem analytically, an equivalent leakoff coefficient, $C_{L,eq}$, was introduced. Figure 2.5 shows the geometry after injecting two different fluids, where x_{f2} is the fracture half-length occupied by the second fluid and x_{f1} is the fracture half-length occupied by the first. Assuming that there is an equivalent leakoff coefficient that can describe the leakoff behavior of both fluids during the total injection time, $C_{L2,eq}$, the total volume of the fluid leakoff can be described by Eq. 2.30, as follows:

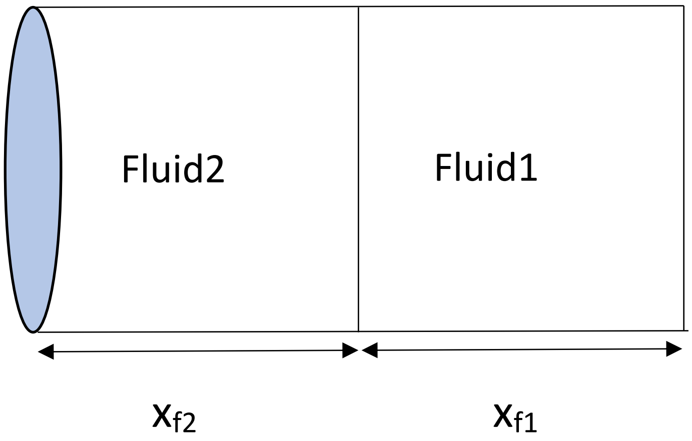

Figure 2.5: Geometry of two fluid systems.

$$Total\ Leakoff\ Volume\ = 2(x_{f1}+x_{f2})h_f(\kappa C_{L2,eq}\sqrt{t_{e1}+t_{e2}}) \tag{2.30}$$

where t_{e1} is the injection time of the first fluid and t_{e2} is the injection time of the second. To calculate the leakoff volume of the first fluid during the total injection time, the leakoff volume of the second fluid was subtracted from the total leakoff volume:

$$\begin{bmatrix} Fluid1 \\ Leakoff \\ Volume \end{bmatrix} = \begin{bmatrix} Total \\ Leakoff \\ Volume \end{bmatrix} - \begin{bmatrix} Fluid2 \\ Leakoff \\ Volume \end{bmatrix} \tag{2.31}$$

$$\begin{bmatrix} Fluid1 \\ Leakoff \\ Volume \end{bmatrix} = 2(x_{f1}+x_{f2})h_f(\kappa C_{L2,eq}\sqrt{t_{e1}+t_{e2}}) - 2x_{f2}h_f(\kappa C_{L2}\sqrt{t_{e2}}) \tag{2.32}$$

where C_{L2} is the second fluid leakoff coefficient. In this approach, it was assumed that the first fluid injection did not affect the leakoff behavior of the second. Since the second fluid was described as the reactive one, this assumption was valid, especially considering that the acid removed the filter cake created by the pad fluid injection.

Another approach to calculating first fluid leakoff volume assumed that it occupied the total fracture length (see Fig. 2.5). However, to account for real situations, the leakoff of the imaginary part of fluid1 that occupied the fluid2 position during t_{e2} was subtracted as follows:

$$\begin{bmatrix} Fluid1 \\ Leakoff \\ Volume \end{bmatrix} = 2(x_{f1}+x_{f2})h_f(\kappa C_{L1}\sqrt{t_{e1}+t_{e2}}) - 2x_{f2}h_f(\kappa C_{L1}\sqrt{t_{e2}}) \tag{2.33}$$

where C_{L1} is the fluid1 leakoff coefficient. To calculate the equivalent leakoff coefficient, Eq. 2.32 was equated to Eq. 2.33, and algebra was applied to obtain:

$$C_{L2,eq} = \frac{(x_{f1}+x_{f2})\ C_{L1}\sqrt{t_{e1}+t_{e2}} - x_{f2}C_{L1}\sqrt{t_{e2}} + x_{f2}C_{L2}\sqrt{t_{e2}}}{(x_{f1}+x_{f2})\ \sqrt{t_{e1}+t_{e2}}} \tag{2.34}$$

This approximate formula could then be generalized for n different fluid injections, as follows:

$$C_{Ln,eq} = \frac{(x_{ft})\, C_{L1}\sqrt{t_{et}} - (x_{ft} - x_{f1})\sqrt{t_{et} - t_{e1}}(C_{L1} - C_{L(n-1),eq})}{x_{ft}\ \sqrt{t_{et}}} \tag{2.35}$$

where x_{ft} is the total fracture half-length, t_{et} is the total injection time, $C_{Ln,eq}$ is the equivalent leakoff coefficient for n different fluid systems, and $C_{L(n-1),eq}$ is the equivalent leakoff coefficient for n different fluid systems except for fluid1. Individual fluid leakoff coefficient should be evaluated first to be able to obtain the equivalent leakoff coefficient. Next section describes how to evaluate the leakoff coefficient for a single fluid.

To completely describe the injection of n different fluid systems (see Fig. 2.6), n width and material balance equations were required. Lo and Dean's (1989) approach was used to calculate the fracture width for multiple power law fluids:

$$\begin{aligned} w_{max,i} = \Bigg\{ & \frac{128}{3\pi}(n_i + 1)K_i \frac{(1 - v^2)h_f}{E} * \left[\frac{(2n_i + 1)q_{i,i}}{n_i h_f}\right]^{n_i} x_{f,i} \\ & + w_{max,i-1}^{2n_i+2} \Bigg\}^{\frac{1}{2n_i+2}}, i = 2,3, \dots n \end{aligned} \tag{2.36}$$

After assuming that the fracture contained three different fluid systems (pad, acid, and flush), the material balance for each fluid could be formulated by implementing the equivalent leakoff concept. The material balance for the first fluid could then be described as follows:

$$\begin{aligned} & \frac{q_{i1}t_{e1}}{2} - 2\kappa h_f\left(x_{f1} + x_{f2} + x_{f3}\right)C_{L3,eq}\sqrt{t_{e1} + t_{e2} + t_{e3}} \\ & \qquad + 2\kappa h_f\left(x_{f2} + x_{f3}\right)C_{L2,eq}\sqrt{t_{e2} + t_{e3}} - \bar{w}_1 x_{f1} h_f = 0 \end{aligned} \tag{2.37}$$

Similarly, the second fluid material balance was:

$$\begin{aligned} & \frac{q_{i2}t_{e2}}{2} - 2\kappa h_f\left(x_{f2} + x_{f3}\right)C_{L2,eq}\sqrt{t_{e2} + t_{e3}} + 2\kappa h_f\left(x_{f3}\right)C_{L3}\sqrt{t_{e3}} \\ & \qquad - \bar{w}_2 x_{f2} h_f = 0 \end{aligned} \tag{2.38}$$

The third fluid material balance was:

$$\frac{q_{i3} t_{e3}}{2} - 2\kappa h_f(x_{f3}) C_{L3}\sqrt{t_{e3}} - \bar{w}_3 x_{f3} h_f = 0 \tag{2.39}$$

where q_{i1}, q_{i2}, and q_{i3} are the injection rates of the first, second, and third fluids.

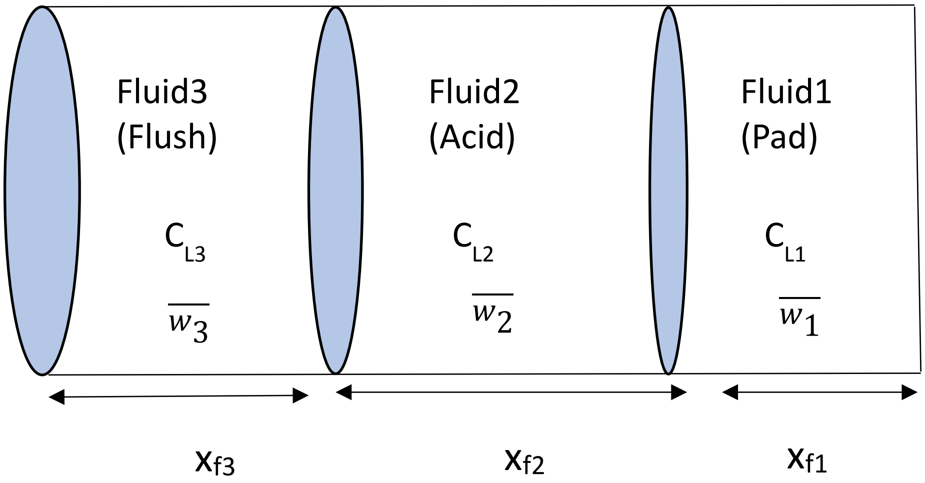

Figure 2.6: Fracture geometry of three fluid systems.

2.1.5 Leakoff Coefficient Evaluation

An accurate determination of a single fluid leakoff coefficient, C_L, is significant in evaluating the fracture geometry. The fracture dimensions and acid penetration distance were both affected by this parameter. Also, the value of the parameter determined the efficiency of the fracturing fluids, which was the ratio of the fracture volume to the injected fluid volume. A high leakoff coefficient could cause a premature job failure because the pressure cannot build up to the fracture lifting pressure. The leakoff coefficient consisted of three parameters, as shown in Figure 2.7. Schechter (1992) showed the mathematical derivation of these coefficients. The wall building, C_w, represented the first layer of the fracture wall resulting from the formation of a filter cake during injection. The term could be evaluated as follows:

$$C_w = m_w/2 \tag{2.40}$$

where m_w is the slope of the filtrate volume to square root time curve. Effluent viscosity formed the second layer of the fracture wall resulting from the fracture fluid filtrate penetrating the fracture wall's pores. The invaded zone leakoff coefficient, C_v, was evaluated as follows:

$$C_v = \left(\frac{k_{ef}\Delta P\varphi}{2\mu_{ef}}\right)^{\frac{1}{2}} \tag{2.41}$$

where φ is the formation porosity, k_{ef} is the relative permeability of the formed effluent fluid, μ_{ef} is the effluent fluid viscosity, and ΔP is the difference between the fracture and reservoir pressures. The third layer represented the reservoir fluid viscosity and compressibility. The leakoff coefficient of the third term, C_c, was evaluated as follows:

$$C_c = \Delta P\left(\frac{k_p c_t \varphi}{\pi\mu_r}\right)^{\frac{1}{2}} \tag{2.42}$$

where k_p is the reservoir fluid permeability, c_t is the formation's total compressibility, and μ_r is the reservoir fluid viscosity. There were several methods available to combine the three coefficients into one leakoff coefficient. One method combined C_v and C_c, as shown in Eq. 2.43, and compared the value with C_w, where the lower value coefficient was used as the total coefficient. Another method combined the total pressure drop contribution of each coefficient, leading to Equation 2.44 (Penny and Conway, 1989).

$$C_{vc} = \frac{2C_v C_c}{C_v + (C_v^2 + 4C_c^2)^{\frac{1}{2}}} \tag{2.43}$$

$$C_L = \frac{2C_v C_c C_w}{C_v C_w + [C_w^2 C_v^2 + 4C_c^2(C_v^2 + C_w^2)]^{\frac{1}{2}}} \tag{2.44}$$

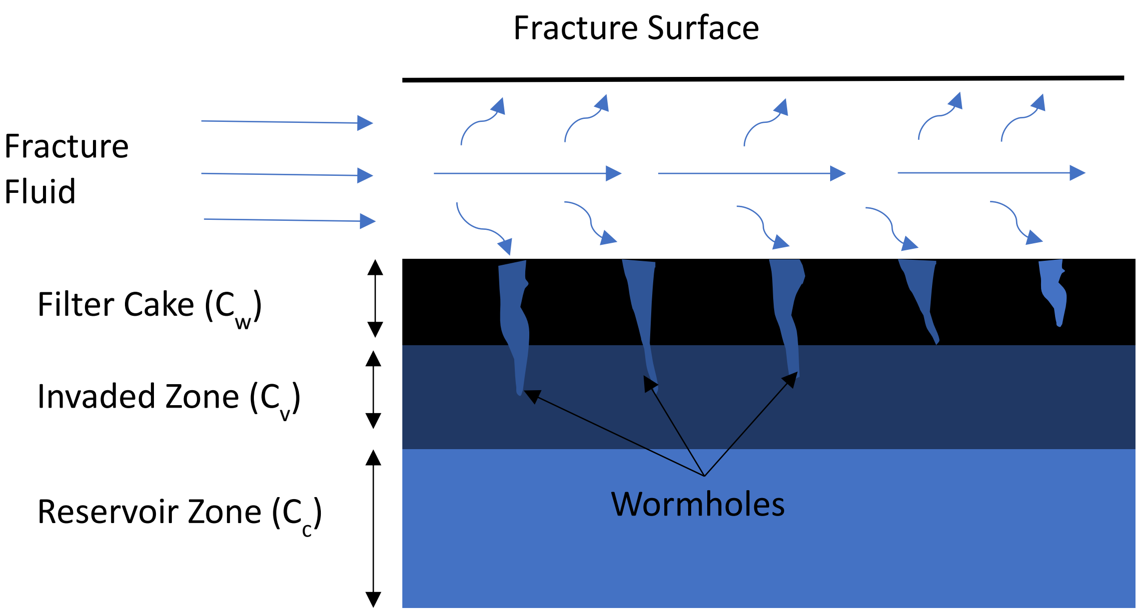

Figure 2.7: Leakoff parameters as they appeared in the fracture wall adapted from Hill et al. (1995).

Acid injection creates wormholes in fracture walls that affect the leakoff coefficient. The severity of this effect, which depends on the type of formation, is more noticeable in calcite than dolomite formations. This effect can be quantified by measuring the pore volume of acid needed for the wormhole to breakthrough. In the simulator, the value of the pore volume needed to breakthrough, Q_{ibt}, was 1.5 for calcite and 20 for dolomite. Then, the C_v value was corrected for the wormhole effect, as shown in Eq. 2.45. Assuming that C_w was large compared to C_v or C_c, the total leakoff coefficient, including the wormhole effect, could then be shown by Eq. 2.46 (Hill et al., 1995).

$$C_{v,wh} = \sqrt{\frac{Q_{ibt}}{Q_{ibt} - 1}} * C_v \tag{2.45}$$

$$C_L = \frac{-\frac{1}{C_c} + \sqrt{\frac{1}{C_c^2} + \frac{4}{C_{v,wh}^2}}}{2 * \left(\frac{1}{C_{v,wh}^2}\right)} \tag{2.46}$$

When the fracture penetrated different formation layers, the leakoff coefficient of the fluid system, $\bar{C}_{Li}$, was averaged according to the layers' thickness, h_j, as follows:

$$\bar{C}_{Li} = \frac{\sum_{j=1}^{j=n} C_{Li,j}\, h_j}{h_f} \tag{2.47}$$

where i stands for the fluid system, j indicates the formation layer, and $C_{Li,j}$ is the leakoff coefficient of a fluid system, i, in a formation layer, j.

2.1.6 Fracture Closure Geometry

Both the fracture height and half-length were assumed to be constant during fracture closure and equal to what was obtained at the final injection time. Therefore, fracture width and net pressure were the only parameters that should be calculated. Fracture width during fracture closure is used for both acid and temperature solutions. A differential material balance equation (Eq. 2.16) was used to balance the fluid volume during closure. The equation was integrated over the fracture half-length, as follows:

$$\int_0^{x_f} \frac{\partial q}{\partial x} dx + \int_0^{x_f} q_L\, dx + \int_0^{x_f} \frac{\partial A}{\partial t} dx = 0 \tag{2.48}$$

Since there was no fluid injection, the flow rate at both the inlet and outlet was zero, resulting in a removal of the first term. Substituting the expression for q_L (Eq. 2.17) and A in the previous equation resulted in:

$$\int_0^{x_f} \frac{2C_L h_f}{\sqrt{t-\tau(x)}} dx + \int_0^{x_f} \frac{\partial(h_f \overline{w})}{\partial t} dx$$
$$= \int_0^{x_f} \frac{2C_L}{\sqrt{t-\tau(x)}} dx + \int_0^{x_f} \frac{\partial(\overline{w})}{\partial t} dx = 0 \tag{2.49}$$

The equation indicates that the decrease in fracture volume is equal to the fluid loss rate. Nolte (1979) developed a method of integrating the fluid loss term during fracture closure by introducing the pressure decline function, $f(t)$, as follows:

$$f(t) = \sqrt{t_e}/x_f \int_0^{x_f} \frac{1}{\sqrt{t-\tau(x)}} dx = 2(\sqrt{1+t} - \sqrt{t}) \tag{2.50}$$

where Δt is the time interval after shut-in. Integrating Eq. 2.49 resulted in:

$$\frac{2C_L f(t)}{\sqrt{te}} = -\frac{d\overline{w}}{dt} \tag{2.51}$$

Introducing the dimensionless shut in time, δ, yielded the following:

$$\delta = \frac{\Delta t}{t_e} \tag{2.52}$$

Integrating Eq. 2.51 from zero to a dimensionless shut-in time produced the following:

$$-\left(\frac{1}{t_e}\right) \int_0^{\delta} \frac{d\overline{w}}{d\delta} d\delta = \frac{2C_L}{\sqrt{te}} \int_0^{\delta} f(\delta)\, d\delta \tag{2.53}$$

The result of this integration was the fracture width as a function of dimensionless shut-in time, as follows:

$$\overline{w}(\delta) = \overline{w}(0) - 2\, C_L \sqrt{t_e}\, g(\delta) \tag{2.54}$$

where $\overline{w}(0)$ is the fracture's average width at the final injection time, t_e, and $g(\delta)$ is the function obtained from integrating $f(\delta)$.

$$g(\delta) = 4/3[(1+\delta)^{\frac{3}{2}} - \delta^{\frac{3}{2}} - 1] \tag{2.55}$$

Assuming that the closure time is when the fracture width is equal zero, the $g(\delta)$ function could be obtained from Eq. 2.54, as follows:

$$g(\delta)=\frac{\overline{w}(0)}{2\,C_L\sqrt{t_e}} \tag{2.56}$$

The time it takes for the fracture to close was obtained by substitution Eq. 2.56 into Eq. 2.55 and solving for δ, from which Δt was obtained. The fracture net pressure during closure could then be obtained in a similar way (Nolte, 1979).

$$P_{net}(\delta)=P_{net}(0)-\frac{C_L\grave{E}\sqrt{te}}{h_f B_s}*\frac{4}{\pi}g(\delta) \tag{2.57}$$

where the term B_s is:

$$B_s=\frac{2n+2}{2n+3+a} \tag{2.58}$$

and where n is the flow behavior index and a is the viscosity behavior-dependent constant where $a=0$ was used in the model.

2.1.7 Fracture Propagation Model Assumptions

The geometric model introduced in this section was derived in response to the following assumptions and limitations:

1) There was a vertical plain strain with an elliptical shape crack.
2) There was a zero net fracture pressure at the fracture tip.
3) The fracture height was a function of the injection time, but not a function of position. Liu and Valko's approach was used to calculate the fracture height.
4) The fracture width represented an asymptotic large-time solution (PKN width).

5) Each fluid system was injected at a constant flow rate (but different fluid systems could have had different injection rates).
6) An integrated 1D material balance was used to calculate the fracture half-length.
7) The leakoff rate was approximated using Nolte's method.
8) There was an equivalent leakoff coefficient that described the leakoff of multiple fluid systems.

2.2 Acid Model

The acid model consisted of solving for the acid concentration profile along the fracture dimensions. Based on the reaction kinetics, the fracture etched-width distribution was calculated. The conductivity distribution of the fracture was then estimated based on the etching profile via a conductivity correlation. In the literature, the models were developed to calculate the etched-width profile during acid injection, assuming that the acid accumulating inside the fracture reacted completely at the fracture surfaces. The developed model solved for the acid concentration after the injection stopped in order to correctly model the reactions of weak acids and less-reactive formations such as dolomite. The following sections describe elements of the acid model.

2.2.1 Acid Solution Domain

At each time step, the fracture propagation model provided the domain for the acid solution. The fracture height could penetrate undesired, non-reactive layers, as shown in the upper left-hand corner of Figure 2.8. Acid simulation was only performed at the pay zone determined from the field data. The pay zone was gridded in the height direction, as can be seen in the upper right-hand corner of Figure 2.8; the number of grids was determined by the pay zone heterogeneity. Each layer was then assigned an average width and gridded in the fracture length, x, and width, y, directions, as can be seen in the lower left-hand corner of Figure 2.8. As the fracture propagated, the fracture width and length increased; therefore, more grid blocks were generated in the x direction, but the grids were only inflated in the y direction, as shown in the lower right-hand corner of Figure 2.8.

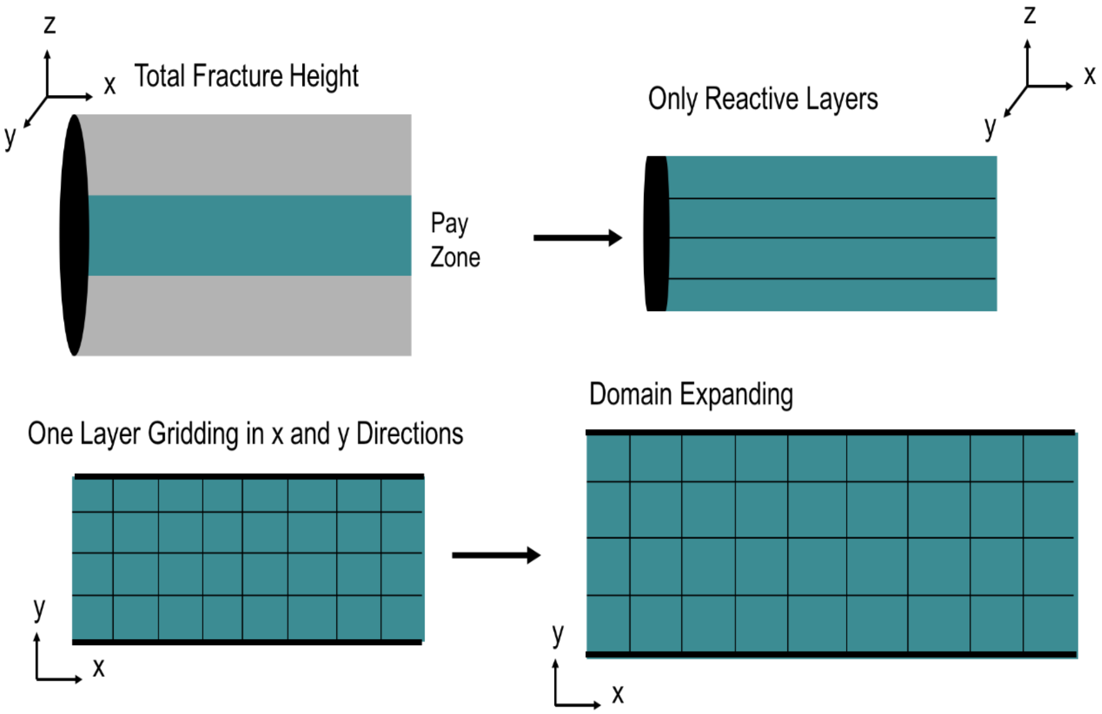

Figure 2.8: Acid solution domain.

2.2.2 Acid Mass Balance

Figure 2.9 shows the control volume from which the acid mass balance equation was derived. The total mass (or molar) flux of acid, N_A, in x direction was written as:

$$N_{A,x} = C_A u + J_{A,x} \tag{2.59}$$

The first term represents acid flux by convection, and the second term is the acid flux by diffusion.

Fick's law was used to evaluate acid flux by diffusion, as follows:

$$J_{A,x} = -D_{A,x}\frac{\partial C_A}{\partial x} \tag{2.60}$$

The mass (or molar) balance over the control volume was written as:

$$\begin{bmatrix} Acid \\ Mass \\ In \end{bmatrix} = \begin{bmatrix} Acid \\ Mass \\ out \end{bmatrix} + \begin{bmatrix} Acid \\ Accumulation \end{bmatrix} + \begin{bmatrix} Acid \\ Reaction \end{bmatrix} \tag{2.61}$$

The mass of acid entering the control volume at Δt was:

$$N_{A,x}\Delta y\Delta z\Delta t + N_{A,y}\Delta x\Delta z\Delta t + N_{A,z}\Delta x\Delta y\Delta t \tag{2.62}$$

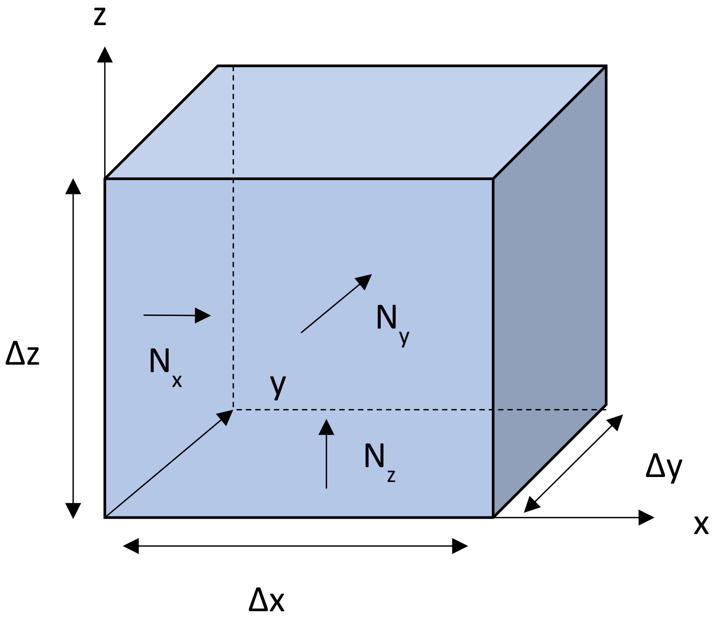

Figure 2.9: Acid mass balance control volume.

The mass of the acid leaving the control volume over the same period was:

$$N_{A,x+\Delta x}\Delta y\Delta z\Delta t + N_{A,y+\Delta y}\Delta x\Delta z\Delta t + N_{A,z+\Delta z}\Delta x\Delta y\Delta t \qquad (2.63)$$

The mass of the acid that accumulated was:

$$(C_A^{n+1} - C_A^n)\Delta x\Delta y\Delta z \qquad (2.64)$$

where n represents the time step. The amount of acid reaction in the control volume was:

$$R_{v,A}\Delta x\Delta y\Delta z\Delta t \qquad (2.65)$$

where $R_{v,A}$ is the mass (or molar) rate of the acid reaction per unit volume. Putting the terms together, dividing by $\Delta x\Delta y\Delta z\Delta t$, and rearranging the terms yielded the following:

$$\frac{(C_A^{n+1} - C_A^n)}{\Delta t} + \frac{(N_{A,x+\Delta x} - N_{A,x})}{\Delta x} + \frac{(N_{A,y+\Delta y} - N_{A,y})}{\Delta y} + \frac{(N_{A,z+\Delta z} - N_{A,z})}{\Delta z} = R_{v,A} \qquad (2.66)$$

The limits were taken as $\Delta x, \Delta y, \Delta z,$ and at Δt they approached zero.

$$\frac{\partial C_A}{\partial t} + \frac{\partial N_{A,x}}{\partial x} + \frac{\partial N_{A,y}}{\partial y} + \frac{\partial N_{A,z}}{\partial z} = R_{v,A} \qquad (2.67)$$

Substituting the total flux expression (Eq. 2.59) into the previous equation and rearranging it led to:

$$\frac{\partial C_A}{\partial t} + \frac{\partial (uC_A)}{\partial x} + \frac{\partial (vC_A)}{\partial y} + \frac{\partial (wC_{A)}}{\partial z} = \frac{\partial}{\partial x}(D_{A,x}\frac{\partial C_A}{\partial x}) + \frac{\partial}{\partial y}(D_{A,y}\frac{\partial C_A}{\partial y}) + \frac{\partial}{\partial z}(D_{A,z}\frac{\partial C_A}{\partial z}) + R_{v,A} \qquad (2.68)$$

where u is the velocity in the x direction, v is the velocity in the y direction, and w is the velocity in the z direction. Applying the continuity equation yielded:

$$\frac{\partial u}{\partial x} + \frac{\partial v}{\partial y} + \frac{\partial w}{\partial z} = 0 \qquad (2.69)$$

The final form of the mass balance considering Eq. 2.69 was as follows:

$$\frac{\partial C_A}{\partial t} + u\frac{\partial C_A}{\partial x} + v\frac{\partial C_A}{\partial y} + w\frac{\partial C_A}{\partial z} = \frac{\partial}{\partial x}(D_{A,x}\frac{\partial C_A}{\partial x}) + \frac{\partial}{\partial y}(D_{A,y}\frac{\partial C_A}{\partial y}) + \frac{\partial}{\partial z}(D_{A,z}\frac{\partial C_A}{\partial z}) + R_{v,A} \tag{2.70}$$

In acid fracturing operations, acid reactions happen at the fracture surfaces, but normally no acid reaction in the fluid phase is assumed; hence, the term $R_{v,A}$ was omitted here. Also, the diffusion coefficients of the acid in all directions were assumed to be the same. To simplify the model, the z direction convection and diffusion were ignored. However, the model solved for the acid concentration in the z direction to account for the minerology and fracture width distribution in each layer. The acid mass balance used in the model an applied to each layer was as follows:

$$\frac{\partial C_A}{\partial t} + u\frac{\partial C_A}{\partial x} + v\frac{\partial C_A}{\partial y} = \frac{\partial}{\partial x}(D_A\frac{\partial C_A}{\partial x}) + \frac{\partial}{\partial y}(D_A\frac{\partial C_A}{\partial y}) \tag{2.71}$$

To totally define the problem during acid injection, the following initial and boundary conditions were applied. Before injection began, the acid concentration was zero everywhere.

$$C_A(x, y, t = 0) = 0 \tag{2.72}$$

On the fracture entrance, the acid concentration was the same as the live acid concentration, C_i.

$$C_A(x = 0, y, t) = C_i \tag{2.73}$$

On the fracture surfaces, the acid diffusion towards the fracture surfaces was equal to the disappearance of the acid because of the reaction.

$$D_A\frac{\partial C_A}{\partial y} = k_r\left(C_w - C_{eq}\right)^{n_r}(1 - \varphi) \tag{2.74}$$

where k_r is the reaction rate constant, n_r is the reaction exponent, C_{eq} is the acid equilibrium concentration, and C_w is the acid concentration at the fracture walls.

When the injection stopped and the fracture started to close, acid convection in the fracture length direction became negligible; the governing equation could then be simplified as follows:

$$\frac{\partial C_A}{\partial t} + v\frac{\partial C_A}{\partial y} = D_A\frac{\partial^2 C_A}{\partial y^2} \tag{2.75}$$

To solve the differential equation, the following initial and boundary conditions were applied. Initially, the acid concentration in the fracture domain was the same as the concentration during the final injection time step.

$$C_A(x, y, t = 0) = C_A(x, y, t = t_e) \tag{2.76}$$

On the fracture inlet, there was no acid flux.

$$\frac{\partial C_A}{\partial x} = 0 \tag{2.77}$$

On the fracture surfaces, the boundary condition during fracture closure was similar to the boundary condition during acid injection (Eq. 2.74). For both differential equations, the finite volume formulation was used and the power law scheme implemented.

2.2.3 Velocity Profile

To solve for the acid concentration profile, the acid velocity distribution needed to be provided. In this model, Berman’s (1953) analytical solution was used to update the velocity profile. The solution was obtained by solving the continuity and momentum balance equations at the fracture length and width dimensions. The fluid was assumed to flow between parallel leaky channels.

$$\frac{\partial u}{\partial x} + \frac{\partial v}{\partial y} = 0 \tag{2.78}$$

$$\rho u\frac{\partial u}{\partial x} + \rho v\frac{\partial u}{\partial y} = -\frac{\partial p}{\partial x} + \mu(\frac{\partial^2 u}{\partial x^2} + \frac{\partial^2 u}{\partial y^2}) \tag{2.79}$$

$$\rho u\frac{\partial v}{\partial x} + \rho v\frac{\partial v}{\partial y} = -\frac{\partial p}{\partial y} + \mu(\frac{\partial^2 v}{\partial x^2} + \frac{\partial^2 v}{\partial y^2}) \tag{2.80}$$

where p is the fluid pressure and μ is the fluid viscosity. A solution by perturbation was implemented by Berman that assumed the following boundary conditions: no slip, a constant leakoff velocity at the fracture walls, and a symmetrical condition at the channel center. The solution was obtained as follows:

$$u(x,y) = \left[u_{in} - \frac{2v_L x}{\bar{w}}\right] f(\eta) \tag{2.81}$$

$$v(y) = v_L \grave{f}(\eta) \tag{2.82}$$

$$f(\eta) = \frac{3}{2}(1-\eta^2) * \left(1 - \frac{N_{Re_L}}{420} * (2 - 7\eta^2 - 7\eta^4)\right) \tag{2.83}$$

$$\grave{f}(\eta) = \frac{\eta}{2}(3-\eta^2) - \frac{N_{Re_L}}{280}\eta(2 - 3\eta^2 + \eta^6) \tag{2.84}$$

$$\eta = \frac{2\left(y - \frac{\bar{w}}{2}\right)}{\bar{w}}, \qquad y = \frac{\bar{w}}{2}, \qquad N_{Re_L} = \frac{\rho v_L \bar{w}}{2\mu} \tag{2.85}$$

where η is the dimensionless position at the width direction, u_{in} is the velocity at the inlet, and N_{Re_L} is the leakoff Reynold's number. The following were assumed for this solution:

1) An incompressible Newtonian fluid in a steady state condition;
2) Constant channel width;
3) Constant leakoff velocity;
4) No convection in the channel height direction; and
5) $N_{Re_L} < 7$.

In acid fracturing operations, N_{Re_L} is usually smaller than 1. For example, a straight acid that was injected for 30 minutes and had the following properties: 62.4 $\text{lb}_\text{m}/\text{ft}^3$ density, 1 cp viscosity, and $4\text{x}10^{-3}$ $\text{ft/min}^{0.5}$ leakoff coefficient that created an average fracture width of 0.2 inch resulted in $N_{Re_L} = 0.85$. In this example, the average leakoff velocity was calculated, assuming $\kappa = 1.5$, as follows (Schechter, 1992):

$$v_L = \frac{\kappa C_L}{\sqrt{t_e}} \tag{2.86}$$

If assuming a constant leakoff velocity is inaccurate, as leakoff velocity is believed to follow Carter's method (Eq. 2.17), the acid solution domain was divided into smaller domains, each representing a constant leakoff velocity. The Berman solution was applied to each domain, and the outlet velocity from one domain was assumed to be the inlet for the next. When a power law fluid injection was simulated, the viscosity in Eq. 2.86 was replaced by the effective viscosity given in Eq. 2.8.

During fracture closure, Berman's solution is no longer valid. Hence, another velocity profile needed to be implemented. From the derivation of the continuity equation during fracture closure over the control volume, the following equation was obtained:

$$\frac{\partial \bar{w}}{\partial t} + \bar{w}\frac{\partial}{\partial y}(v) = 0 \tag{2.87}$$

where the first term represents the decrease in fracture width and the second term is the fluid convection by leakoff. The first term was then evaluated using Eq. 2.51, resulting in:

$$\bar{w}\frac{d}{dy}(v) = \frac{2C_L f(t)}{\sqrt{te}} \tag{2.88}$$

Integrating the equation from the fracture center to a location y led to:

$$\bar{w}\int_{v=0}^{v} d(v) = \int_{\frac{\bar{w}}{2}}^{y} \frac{2C_L f(t)}{\sqrt{te}}\,dy \tag{2.89}$$

Rearranging the equation after integration obtained the following:

$$v(y) = \frac{\frac{C_L f(t)}{\sqrt{te}}\left(y - \frac{\bar{w}}{2}\right)}{\frac{\bar{w}}{2}} \tag{2.90}$$

The leakoff velocity during fracture closure could then be defined as:

$$v_L = \frac{C_L f(t)}{\sqrt{te}} \tag{2.91}$$

Hence, the velocity profile at the fracture width linearly increased towards the fracture walls, as follows:

$$v(y) = v_L \frac{\left(y - \frac{\overline{w}}{2}\right)}{\frac{\overline{w}}{2}} = v_L \eta \tag{2.92}$$

2.2.4 Acid Reaction and Etched Fracture Width

The molecular reaction between the hydrochloric acid, HCl, and minerals of the calcite or dolomite rocks, respectively, was described as follows:

$$2HCl + CaCO_3 \rightarrow CaCl_2 + CO_2 + H_2O \tag{2.93}$$

$$4HCl + CaMg(CO_3)_2 \rightarrow CaCl_2 + MgCl_2 + 2CO_2 + 2H_2O \tag{2.94}$$

where $CaCO_3$ represents the minerology of calcite rocks and $CaMg(CO_3)_2$ represents that of dolomite rocks. The rate law describes the rate of reaction, R, in moles per unit time and as the product of a reaction rate constant, k_r, with the reactants concentrations $[A]$ and $[B]$, each to a certain exponent, n_{rA} and n_{rB}, as follows:

$$R = k_r [A]^{n_{rA}} [B]^{n_{rB}} \tag{2.95}$$

Since the reaction occurred at the rock surface, the rock mineral concentration was omitted. The acid reaction rate, r, in moles per unit surface area and time, with these rock minerals could then be written as follows:

$$r = k_r C_w^{n_r} \tag{2.96}$$

However, when the reaction was incomplete because of a weak acid reaction, the reaction rate was written as follows:

$$r = k_r \left(C_w - C_{eq}\right)^{n_r} \tag{2.97}$$

where C_{eq} is the acid concentration at equilibrium. In acid fracturing operations, the reaction occurs at the surfaces of porous rocks. Hence, the reaction rate was modified as follows:

$$r = k_r\left(C_w - C_{eq}\right)^{n_r}(1-\varphi) \tag{2.98}$$

where φ is the rock porosity. Table 2.1 shows the reaction rate constants and exponents used in this study for the calcite and dolomite rocks (Schechter, 1992).

Table 2.1: Reaction Kinetics Constants for the Reaction between HCl-Calcite and HCl-Dolomite

Mineral	n_r	$k_r^0[\frac{kg\ moles\ HCl}{m^2.s.\left(\frac{kgmoles\ HCl}{m^3\ acid\ solution}\right)^{n_r}}]$	$\frac{\Delta E}{R}\ (K)$
Calcite	0.63	7.314x10^7	7.55x10^3
Dolomite	$\frac{6.32\text{x}10^{-4}T}{1-1.92\text{x}10^{-3}T}$	4.48x10^5	7.9x10^3

The reaction rate constant is temperature sensitive, and described by the Arrhenius formula, as follows:

$$k_r = k_r^0\exp(-\frac{\Delta E}{RT}) \tag{2.99}$$

where k_r^0 is the reaction rate constant, ΔE is the activation energy, R is the universal gas constant, and T is the absolute temperature.

To calculate the mass of rock dissolved per a certain mass of acid, the gravimetric dissolving power, β, was introduced by Williams et al. (1979), as follows:

$$\beta = \frac{v_{mineral}\,MW_{mineral}}{v_{acid}\,MW_{acid}} \tag{2.100}$$

where v is the stoichiometric coefficient appearing in Eqs. 2.93 to 2.94, and MW is the molecular weight. The concept is valid only when the acid reaction with minerals is complete. The gravimetric dissolving power for 100% HCl reacting with calcite and dolomite rocks, β_{100}, was calculated to be 1.37 $\frac{Kg\ CaCO_3}{Kg\ HCl}$ and 1.27 $\frac{Kg\ CaMg(CO_3)_2}{Kg\ HCl}$, respectively. To convert β to a ratio of the volume of rock dissolved by a certain volume of acid solution, the dissolving power, $\mathcal{X}$, was introduced by Williams et al. (1979), as follows:

$$\mathcal{X} = \beta(\frac{\rho_{acid\ solution}}{\rho_{mineral}}) \tag{2.101}$$

where β at a certain acid weight fraction, C_A, is:

$$\beta = C_A\beta_{100} \tag{2.102}$$

To calculate the etched-width profile, the volume of acid reaching the fracture walls and reacting was described in convection and diffusion terms. The incremental volume of acid, ΔV_{acid}, reacting at an incremental area of rock surface, ΔA_f, during an incremental time, Δt, was:

$$\Delta V_{acid} = \left(f_a v_L C_w - D_A \frac{\partial C_A}{\partial y}\bigg|_w \right) \Delta t\ \Delta A_f \tag{2.103}$$

where f_a is the fraction of leaking acid reacting at the fracture walls. The first term on the right-hand side of Eq. 2.103 represents the reacting fraction of leaking acid, and the second term represents the acid flux by diffusion. The incremental volume of porous rock dissolved, ΔV_{rock}, could then be described as follows:

$$\Delta V_{rock}(1-\varphi) = \mathcal{X}\left(f_a v_L C_w - D_A \frac{\partial C_A}{\partial y}\bigg|_w \right) \Delta t\ \Delta A_f \tag{2.104}$$

The incremental etched-width, Δw_e, was defined as:

$$\Delta w_e = \frac{\Delta V_{rock}}{\Delta A_f} \tag{2.105}$$

Rearranging Eq. 2.104 and taking the limit as Δt and approaching zero, the etched-width equation obtained was:

$$\frac{\partial w_e}{\partial t} = \frac{\mathcal{X}}{1-\varphi}\left(f_a v_L C_w - D_A \frac{\partial C_A}{\partial y}\bigg|_w\right) \tag{2.106}$$

2.2.5 Fracture Conductivity (Mou-Deng Correlation)

The final step of the acid model was to calculate the fracture conductivity distribution. The Mou-Deng correlation was selected because it accounts for formation heterogeneity. Deng et al. (2012) used an exponential function (Eq. 2.107) to correlate fracture conductivity, wk_f, with the closure stress, σ_c. This was the same model used by Nierode-Kruck (1973), but the constants (α, β) were determined using many numerical experiments. To determine these constants, three cases were discussed:

$$wk_f = \alpha e^{-\beta\sigma_c} \tag{2.107}$$

1) Permeability dominated distribution

In this case, the mineralogy distribution was assumed to be moderately homogenous, but the leakoff coefficient was assumed to be greater than 0.004 ft/(min)$^{.5}$, or approximately 0.001 ft/(min)$^{.5}$. Because the leakoff was high and the minerals were either 100% calcite or 100% dolomite, the permeability effect prevailed. In their correlations, they used the average fracture etched-width, $\widetilde{w}$ (Eqs. 2.108-2.109), instead of the etched-width, w_e (volume of the rock dissolved over the fracture area).

$$\widetilde{w} = 0.56\,\mathrm{erf}(0.8\sigma_D)\, w_e^{.83} \quad C_L > 0.004\ \mathrm{ft/(min)^{.5}} \tag{2.108}$$

$$\widetilde{w} = 0.2\,\mathrm{erf}(0.78\sigma_D)\, w_e^{.81} \quad C_L \approx 0.001\ \mathrm{ft/(min)^{.5}} \tag{2.109}$$

To begin with, the conductivity at zero closure stress, wk_{f_0}, needed to be evaluated (Eq. 2.110). This value was incorporated into α with other statistical parameters for the permeability distributions, $\lambda_{D,x}, \lambda_{D,z}$, and σ_D, while the Young's modulus, E, was incorporated into β (Eqs. 2.111-2.112).

$$(wk_f)_0 = 4.4 * 10^9\, \widetilde{w}^3 \Big[1 + [a_1 \operatorname{erf}\Big(a_2\big(\lambda_{D,x} - a_3\big)\Big) - a_4 \operatorname{erf}\Big(a_5\big(\lambda_{D,z} - a_6\big)\Big)]\sqrt{e^{\sigma_D} - 1}\Big] \tag{2.110}$$

$$a_1 = 1.82,\ a_2 = 3.25,\ a_3 = 0.12,\ a_4 = 1.31,\ a_5 = 6.71,\ a_6 = 0.03$$

$$\alpha = (wk_f)_0 \left[0.22\big(\lambda_{D,x}\sigma_D\big)^{2.8} + 0.01\left(\big(1 - \lambda_{D,z}\big)\sigma_D\right)^{0.4}\right]^{.52} \tag{2.111}$$

$$\beta = [14.9 - 3.78\ln(\sigma_D) - 6.8\ln(E)] * 10^{-4} \tag{2.112}$$

2) Mineralogy dominated distribution

In this case, the leakoff coefficient was assumed to be less than 0.0004 ft/(min)$^{.5}$ and both the dolomite and calcite minerals existed in the formation. The fraction of calcite, $f_{calcite}$, was needed in the correlation; the permeability distribution's statistical parameters were no longer used in the correlations (Eqs. 2.113-2.115).

$$(wk_f)_0 = 4.48 * 10^9[1 + 2.97(1 - f_{calcite})^{2.02}]\big[0.13 f_{calcite}^{0.56}\big]^3 w_e^{2.52} \tag{2.113}$$

$$\alpha = (wk_f)_0(0.811 - 0.853 f_{calcite}) \tag{2.114}$$

$$\beta = [1.2e^{0.952\, f_{calcite}} + 10.5E^{-1.823}] * 10^{-4} \tag{2.115}$$

3) Competition between the mineralogy and permeability distributions

In this case, the leakoff coefficient was medium, approximately 0.001 ft/(min)$^{.5}$, and both minerals existed in the formation. The conductivity correlations for this case are shown in Eqs. 2.116 to 2.118:

$$(wk_f)_0 = 4.48 * 10^9 \Big[1 + a_1 + \Big(a_2 \operatorname{erf}\Big(a_3\big(\lambda_{D,x} - a_4\big)\Big) - a_5 \operatorname{erf}\Big(a_6\big(\lambda_{D,z} - a_7\big)\Big)\Big) \sqrt{e^{\sigma_D} - 1}\Big] \big[a_8 f_{calcite}^{a_9} + a_{10}\sigma_D\big]^3 w_e^{a_{11}} \tag{2.116}$$

$$a_1 = 0.2, a_2 = 1.0,\ a_3 = 5.0, a_4 = 0.12, a_5 = 0.6, a_6 = 3.5, a_7 = 0.03, a_8 = 0.1,\ a_9 = 0.43,\ a_{10} = 0.14,\ a_{11} = 2.52$$

$$\alpha = \ (wk_f)_0[0.21\lambda_{D,x}^{0.16} + 0.046\ln(\sigma_D) + 0.15\lambda_{D,z}^{-0.17}] \tag{2.117}$$

$$\beta = [53.8 - 4.58\ln(E) + 18.9\ln(\sigma_D)] * 10^{-4} \tag{2.118}$$

2.2.6 Acid Model Limitations

The model presented in this section relied on the following assumptions and limitations:

1) Berman's solution for velocity profile was used, which neglects the effect of fluid convection in the fracture height direction. The limitations of Berman's solution are discussed in Section 2.2.3.
2) Each layer was represented by one mineral and an average fracture width.
3) Only acid diffusion toward the fracture walls contributed to fracture surface etching. Acid leakoff was assumed to contribute to wormhole generation.

2.3 Heat Transfer Model

The need to include the heat transfer model arose from the dependency of the reaction and diffusion rates on the temperature profile. The acid became heated as it was injected into the fracture because of the heat flux from the reservoir. The heat of reaction was another source of the fluid temperature increase. The following sections describe this element of the heat transfer model.

2.3.1 Fracture Energy Balance Formulation

Before developing the fracture's thermal heat equation, the following assumptions were made:

1) The change in kinetic energy was negligible.

2) The work done on the system by gravity and fluid compressibility was negligible.
3) Frictional heat dissipation was omitted.
4) There was no source of heat inside the control volume because the reaction occurred only at the fracture surfaces.
5) Fluid properties such as density, heat capacity, and thermal conductivity were constant.

The energy balance was performed over a control volume like the acid mass balance. The total energy flux in x direction, E_x, could then be described as:

$$E_x = q_x + e_x \tag{2.119}$$

where q_x is the conductive heat flux. The other term, e_x, contains the internal, U, and kinetic energies entering or leaving the control volume boundaries. Since the kinetic energy was neglected, e_x could be defined as follows:

$$e_x = \rho U u \tag{2.120}$$

The conductive heat flux was defined by Fourier's first law, as:

$$q_x = -k_x \frac{\partial T}{\partial x} \tag{2.121}$$

where k is the fluid thermal conductivity. For the sake of simplicity, the fluid thermal conductivity in all directions was assumed to be the same. The energy balance over the control volume was:

$$[Eneryg\ in] = [Eneryg\ out] + [Accumulated\ Energy] \tag{2.122}$$

The energy entering the control volume over a time increment was:

$$[Eneryg\ in] = E_x \Delta y \Delta z \Delta t + E_y \Delta x \Delta z \Delta t + E_z \Delta x \Delta y \Delta t \tag{2.123}$$

The energy leaving the control volume over the same time was:

$$[Eneryg\ out] = E_{x+\Delta x} \Delta y \Delta z \Delta t + E_{y+\Delta y} \Delta x \Delta z \Delta t + E_{z+\Delta z} \Delta x \Delta y \Delta t \tag{2.124}$$

The energy accumulation was:

$$[Accumulated\ Energy] = (\ \rho U^{n+1} - \rho U^{n})\Delta x \Delta y \Delta z \tag{2.125}$$

Putting the terms together, rearranging, and taking the limits as Δx, Δy, and Δz, and with Δt approaching zero, resulted in:

$$\frac{\partial \rho U}{\partial t} + \frac{\partial E_x}{\partial x} + \frac{\partial E_y}{\partial y} + \frac{\partial E_z}{\partial z} = 0 \tag{2.126}$$

Substituting for the total energy flux in each direction and rearranging obtained:

$$\frac{\partial \rho U}{\partial t} + \frac{\partial e_x}{\partial x} + \frac{\partial e_y}{\partial y} + \frac{\partial e_z}{\partial z} = -\frac{\partial q_x}{\partial x} - \frac{\partial q_y}{\partial y} - \frac{\partial q_z}{\partial z} \tag{2.127}$$

The internal energy was then defined as:

$$dU = c_P dT - p d\hat{V} \tag{2.128}$$

where c_P is the heat capacity, p is fluid pressure, and $\hat{V}$ is the specific volume. Since an incompressible fluid was assumed, the internal energy could then be written as:

$$dU = c_P dT \tag{2.129}$$

The values of U, e_i, and q_i were then substituted in Eq. 2.127 and a constant ρ and $c_P$were assumed. Also, the continuity equation was applied to remove the velocity terms from the differential terms, obtaining:

$$\begin{aligned} &\rho c_P \left(\frac{\partial T}{\partial t} + u \frac{\partial T}{\partial x} + v \frac{\partial T}{\partial y} + w \frac{\partial T}{\partial z} \right) \\ &\qquad = \frac{\partial}{\partial x}(k \frac{\partial T}{\partial x}) + \frac{\partial}{\partial y}(k \frac{\partial T}{\partial y}) + \frac{\partial}{\partial z}(k \frac{\partial T}{\partial z}) \end{aligned} \tag{2.130}$$

Assuming that the heat transfer in the fracture height direction was negligible resulted in:

$$\rho c_P \left(\frac{\partial T}{\partial t} + u \frac{\partial T}{\partial x} + v \frac{\partial T}{\partial y} \right) = \frac{\partial}{\partial x}(k \frac{\partial T}{\partial x}) + \frac{\partial}{\partial y}(k \frac{\partial T}{\partial y}) \tag{2.131}$$

The following initial and boundary conditions were applied to totally describe the problem during injection. Before the fluid injection started, the temperature in the target formation was equal to the measured reservoir temperature, T_R.

$$T(x, y, t = 0) = T_R \tag{2.132}$$

On the fracture inlet, the temperature was equal to the injected fluid system at the surface, adjusted for heat transfer inside the wellbore, T_I.

$$T(x = 0, y, t) = T_I \tag{2.133}$$

On the fracture surfaces, the heat flow from the reservoir, in addition to the heat generated from the exothermic reaction, was equal to the heat conducted towards the fracture:

$$-k \frac{\partial T}{\partial y}\bigg|_w = |r * (\Delta H_r)| + q_r(t) \tag{2.134}$$

where ΔH_r is the heat of reaction, q_r is heat flux from the reservoir, and r is the reaction rate. The reaction rate constant, k_r, is a function of the system temperature and an input for both the acid and temperature models. Hence, an iterative procedure was implemented to insure the convergence of both solutions.

When the fluid injection stopped, the convection in the fracture length dimension was assumed to be insignificant. Also, the heat conduction at the fracture length was neglected because of the large aspect ratio of the fracture length to width. The differential equation was simplified as follows:

$$\rho c_p \left(\frac{\partial T}{\partial t} + v \frac{\partial T}{\partial y}\right) = k \frac{\partial^2 T}{\partial y^2} \tag{2.135}$$

To solve the heat transfer equation during fracture closure, the following initial and boundary conditions were applied. Initially, the temperature profile inside the fracture was equal to the temperature at the final injection time.

$$T(x, y, t = 0) = T(x, y, t = t_e) \tag{2.136}$$

On the fracture inlet, the heat flux was negligible.

$$\frac{\partial T}{\partial x} = 0 \tag{2.137}$$

On the fracture surfaces, the boundary condition was similar to what it was during fracture propagation (Eq. 2.134).

The assumption that there was no cross-flow in the height direction during fluid injection was not accurate, because of fracture height propagation. However, the effect may be insignificant to the temperature profile, and hence the etched-width distribution. During fracture closure, the no cross-flow assumption was reasonable because the fracture propagation was negligible and the only convection mechanism observed was fluid leaking through the fracture's porous walls.

2.3.2 Reservoir Heat Flux

To evaluate the heat flux from the reservoir towards the fracture, either a numerical reservoir simulator or simplified analytical solution can be implemented. The choice between the two options was based on the required solution accuracy and problem complexity. Since the added accuracy of developing a numerical reservoir temperature simulator might not have been worth the complexity and computational expense, an analytical solution was used. The solution chosen was developed by Whitsitt and Dysart (1970), and based on the following assumptions:

1) Fracture fluid leakoff was the only heat-convective mechanism moving towards the reservoir that was parallel to the heat flow direction.
2) Heat conduction occurred only through the reservoir rocks.
3) The rock and fracturing fluids' thermal properties were constant.
4) The rock and reservoir fluids' temperatures were identical at any position.

The energy balance over the control volume is shown in Figure 2.10; it resulted in the following reservoir matrix heat transfer equation:

$$\rho_{ma} c_{ma} (1-\varphi) \frac{\partial T_{ma}}{\partial t} + \rho c_p v_L \frac{\partial T_{ma}}{\partial y} = (1-\varphi) k_{ma} \frac{\partial^2 T_{ma}}{\partial y^2} \tag{2.138}$$

where ρ_{ma} is the formation matrix density, c_{ma} is the matrix heat capacity, k_{ma} is the matrix thermal heat conductivity, and T_{ma} is the matrix temperature. Whitsitt and Dysart solved the differential equation using Laplace transform method and assuming the following boundary conditions:

1) Initially, the temperature everywhere was the measured reservoir temperature:

$$T_{ma}(t=0, y) = T_R \tag{2.139}$$

2) At the fracture/reservoir interface, the temperature was the fracture temperature provided by the fracture's energy balance:

$$T_{ma}(t, y=0) = T \tag{2.140}$$

3) The temperature was the measured reservoir temperature at a far-away position:

$$T_{ma}(t, y=\infty) = T_R \tag{2.141}$$

The heat flux at the fracture reservoir interface was defined by Fourier's first law:

$$q_r = -k_{ma} \frac{\partial T_{ma}}{\partial y}\bigg|_{y=0} \tag{2.142}$$

The heat flux was then obtained by taking the derivative to the solution obtained from Eq. 2.138 and substituting the expression in the previous equation to obtain the following:

$$q_r(t) = \sqrt{\frac{(\rho_{ma} c_{ma} k_{ma})}{\pi t}} * (T_R - T_W) * \left[e^{-\xi^2} - \sqrt{\pi}\xi\, erfc(\xi)\right] \tag{2.143}$$

where

$$\xi = \frac{\rho c_p v_L}{2(1-\varphi)} * \sqrt{\frac{t}{\rho_{ma} c_{ma} k_{ma}}} \tag{2.144}$$

and where t stands for time, $erfc$ stands for the error function, and T_W represents the temperature at the fracture walls.

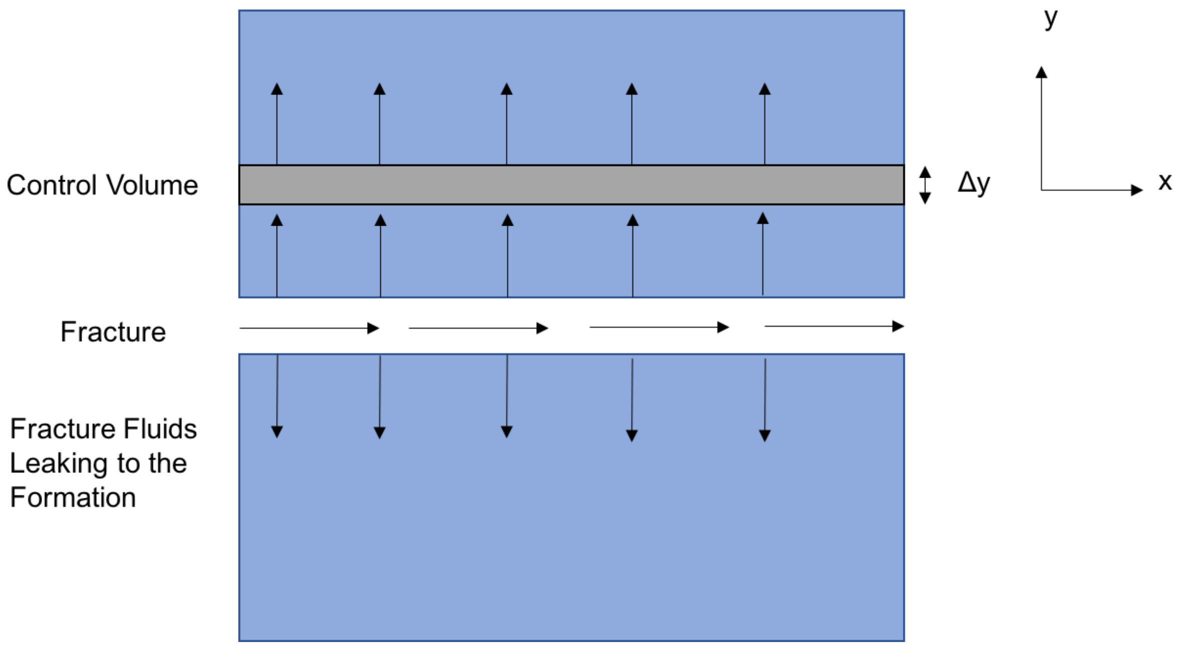

Figure 2.10: Formation's energy balance control volume adapted from Whitsitt and Dysart (1970).

2.3.3 Heat Transfer at the Wellbore

The fluids injected to create the fracture were heated inside the wellbore before entering the wellbore perforations. The increase in fluid temperature resulted from heat conduction from the reservoir. For a vertical wellbore, Ramey's (1962) analytical method was used; this is sufficiently accurate for acid fracturing applications in vertical wells. The following assumptions were made to derive the solution:

1) Incompressible, single fluid system.
2) A steady state heat equation for the wellbore.

3) Transient radial heat conduction for the reservoir.

The analytical solution derived for the injected incompressible fluid at the wellbore is:

$$T_I = g_G D + T_b - g_G Z + (T_s + g_G Z - T_b)e^{-D/Z} \tag{2.145}$$

$$Z = \frac{q_i \rho c_p (k_{ma} + f(t)\, r_1 U_t)}{2\pi k_{ma} r_1 U_t} \tag{2.146}$$

$$f(t) = -\ln\left(\frac{r_2}{2\sqrt{\alpha t}}\right) - 0.29 \tag{2.147}$$

$$\alpha = \frac{k_{ma}}{c_{ma}\rho_{ma}} \tag{2.148}$$

where T_I is the injected fluid temperature at wellbore perforations, g_G is the geothermal gradient, D is the vertical wellbore depth, T_s is the injected fluid temperature at the surface, T_b is the ambient temperature, r_1 is the inner casing or tubing radius, r_2 is the outer casing radius, and U_t is the overall heat transfer coefficient.

2.3.4 Diffusion Coefficient Dependence on Temperature

The diffusion coefficient is a significant parameter in determining the acid penetration distance and etched-width profile. It is difficult to estimate the diffusion coefficients for a component in a liquid mixture. There is no solid equation from which the diffusion coefficients of species in their liquid phase can be estimated. Thus, an experimental approach was the most accurate way of calculating the acid diffusion coefficients. In this study, the acid diffusion coefficient at the ambient temperature was assumed to be determined by the service company, and based on that, the coefficient was updated as the acid was heated inside the fracture. The Stokes-Einstein equation was used to correlate the diffusion coefficient of the liquid at different temperatures (Perry et al., 1997).

$$\frac{D_{T_2}}{D_{T_1}} = \frac{T_2}{T_1}\left(\frac{\mu_{T_1}}{\mu_{T_2}}\right) \tag{2.149}$$

The power law fluids' dependence on temperature was shown to be:

$$\mu = K\dot{\gamma}^{n-1}e^{\frac{T_0}{T}} \tag{2.150}$$

where T_0 is the reference temperature. The power law viscosities at two different temperatures were related according to the previous equation, as follows:

$$\frac{\mu_{T_1}}{\mu_{T_2}} = e^{\frac{T_2}{T_1}} \tag{2.151}$$

From that, the diffusion coefficients at two different temperatures were related, as follows:

$$\frac{D_{T_2}}{D_{T_1}} = \frac{T_2}{T_1}\left(e^{\frac{T_2}{T_1}}\right) \tag{2.152}$$

This equation was used to update the acid diffusion coefficient inside the fracture. The equation was obtained based on the assumption that n and K did not change with temperature.

2.3.5 Heat of Reaction

The acid reaction with the carbonate minerals was an exothermic reaction, meaning that heat was released during the reaction. The heat of reaction, ΔH_r, was calculated by subtracting the products' heat of formation, $\Delta H_{f,p}$, from reactants', $\Delta H_{f,r}$, as follows:

$$\Delta H_r = \sum_{i=1}^{n_{ps}} v_i\,\Delta H_{f,p} - \sum_{i=1}^{n_{rs}} v_i\,\Delta H_{f,r} \tag{2.153}$$

where n_{ps} is the number of produced species and n_{rs} is the number of reacting species. Data for the species' heat of formations at standard conditions are shown in Table 2.2 (Perry et al., 1997).

Table 2.2: Heat of Formation for Different Species at Standard Conditions

Species	H^+	$CaCO_3$	$CaMg(CO_3)_2$	Ca^{++}	Mg^{++}	CO_2	H_2O
$\Delta H_f{}^o$ (KJ/mol)	0	-1207	-2336	-543	-462	-393.5	-285.5

The ionic reactions of the acid at the calcite and dolomite surfaces, respectively, was:

$$2H^+ + CaCO_3 \rightarrow Ca^{++} + CO_2 + H_2O \tag{2.154}$$

$$4H^+ + CaMg(CO_3)_2 \rightarrow Ca^{++} + Mg^{++} + 2CO_2 + 2H_2O \tag{2.155}$$

Applying Eq. 2.153, the heat of reaction released for the calcite and dolomite, respectively, was:

$$\Delta H_r{}^o = -15 \frac{KJ}{mol\, reaction} = -7.5 \frac{KJ}{mol\, H^+}$$

$$\Delta H_r{}^o = -27.6 \frac{KJ}{mol\, reaction} = -6.9 \frac{KJ}{mol\, H^+}$$

where $\Delta H_r{}^o$ is the heat of reaction at standard conditions. A study of the temperature and pressure effects on the calcite heat of reaction was determined by Guo et al. (2014). However, in this study, the heat of reaction was assumed to be constant; the heat of reaction at an assumed average fracture temperature, 80 $°C$ (176 $°F$) , and average pressure, 5000 psi, was evaluated using the charts provided by Guo et al. (2014). The heat of reaction was determined to be:

$$\Delta H_r = -22 \frac{KJ}{mol\, reaction} = -11 \frac{KJ}{mol\, H^+}$$

This value was used as the heat of reaction for both the calcite and dolomite cases in this study.

2.3.6 Temperature Model Limitations

The model presented in this section relied on the following assumptions and limitations:

1) The fracture temperature model had the limitations presented in Section 2.3.1.

2) The heat flux from the reservoir towards the fracture was represented by the Whitsitt and Dysart analytical solution. The limitations of the solution are presented in Section 2.3.2.
3) The fracture fluid temperature at the vertical wellbore was represented by Ramey's analytical solution. The limitations of Ramey's solution are presented in Section 2.3.3.
4) The constant heat of reaction value was selected at the assumed average system temperature and pressure.
5) The diffusion coefficient was known at room temperature, and based on that it was calculated along the fracture dimensions.

2.4 Fracture Productivity Model

Well productivity is defined as the ratio between the production rate and pressure drop. Higher productivity means that the well can produce larger amounts of fluids at the same pressure drop level. Fractures created in the reservoir significantly help with increasing productivity. Analytical solutions of steady and pseudo-steady flows in a reservoir can be used to evaluate fracture well productivity. However, these solutions evaluate productivity by assuming a single average fracture conductivity. Because of the significant decline in fracture conductivity along its length, average conductivity cannot explain the flow in a fracture. Hence, using a numerical reservoir simulator that considers variations in fracture conductivity along the surface is indispensable. In this section, the theoretical approach used to estimate fractured well productivity is introduced. The derivations can be found in the reservoir engineering book written by Dake (2001). The productivity source code was joined to the acid fracture model to facilitate a productivity estimation.

The continuity equation in a porous media had the following mathematical formula:

$$\nabla.(\rho_r\vec{u}) = -\frac{\partial(\varphi\rho_r)}{\partial t} \tag{2.156}$$

where ρ_r represents the reservoir fluids' density. The velocity vector, $\vec{u}$, in a porous media was described by Darcy's law, as follows:

$$\vec{u} = -\frac{\overrightarrow{k_p}}{\mu_r}\nabla P \tag{2.157}$$

where $\overrightarrow{k_p}$ is the reservoir permeability vector, μ_r is the reservoir fluid viscosity, and ∇P is the pressure gradient. The total compressibility could then be defined as follows:

$$c_t = c_r + c_f = \frac{1}{\rho_r}\frac{\partial\rho_r}{\partial P} + \frac{1}{\varphi}\frac{\partial\varphi}{\partial P} \tag{2.158}$$

where c_r is the reservoir fluid compressibility and c_f is the formation rock compressibility. Substituting Darcy's law into the continuity equation and using the definition of compressibility to obtain the diffusivity equation led to:

$$\frac{\partial}{\partial x}\left(k_x\frac{\partial P}{\partial x}\right) + \frac{\partial}{\partial y}\left(k_y\frac{\partial P}{\partial y}\right) + \frac{\partial}{\partial z}\left(k_z\frac{\partial P}{\partial z}\right) = \mu\varphi c_t\frac{\partial P}{\partial t} \tag{2.159}$$

The fracture was placed in the middle of a rectangular-shaped reservoir (see Fig. 2.11). The computational domain was 1/4 the reservoir size. To totally describe the problem, the following initial and boundary conditions were applied:

1) Initially, the pressure everywhere was equal to the measured reservoir pressure.

$$P(x, y, z, t = 0) = P_r \tag{2.160}$$

2) At the outer boundaries, no flow condition was assumed.

$$\nabla P = 0 \tag{2.161}$$

3) Because of symmetry, at the inner boundaries no flow condition was applied (Eq. 2.161).

4) At the wellbore location, either a constant wellbore pressure, P_w:

$$P(x=0, y=0, z=0, t) = P_w \tag{2.162}$$

or a constant flow rate:

$$\frac{\partial P}{\partial x}(x=0, y=0, z=0, t) = constant \tag{2.163}$$

was assumed.

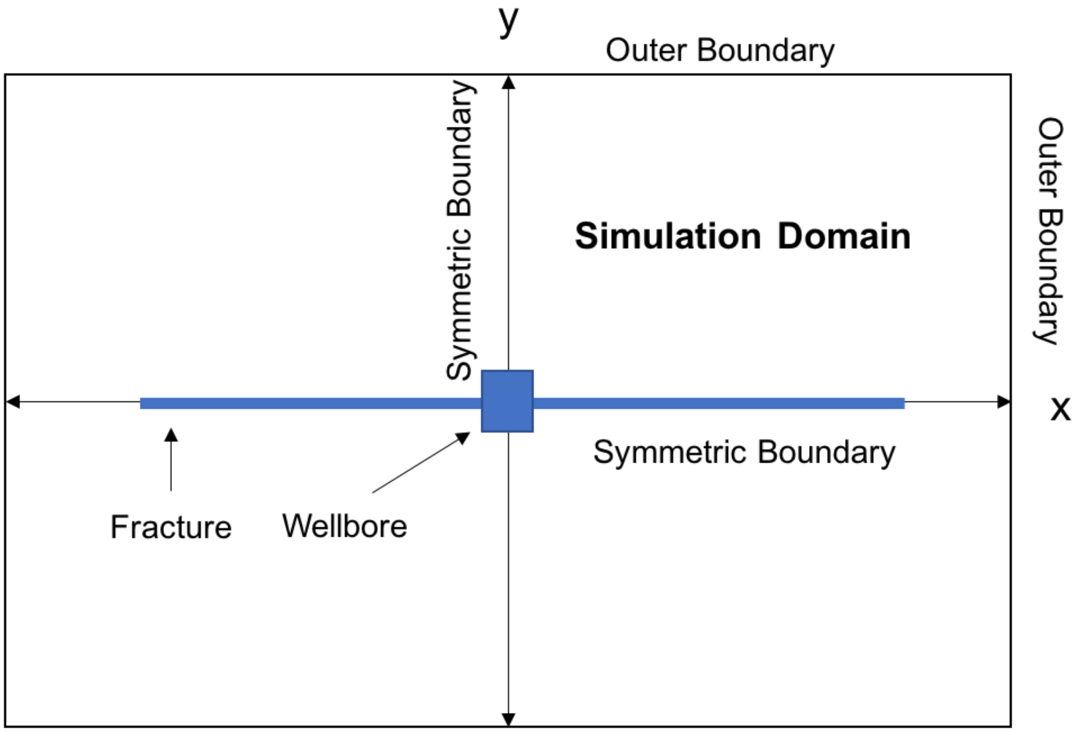

Figure 2.11: Reservoir productivity domain and boundary conditions.

The wellbore productivity, J, was calculated as follows (Economides et al., 1994):

$$J = \frac{q}{\bar{P} - P_w} \tag{2.164}$$

where q is the production rate and $\bar{P}$ is the average reservoir pressure. The dimensionless well productivity, J_D, was:

$$J_D = \frac{141.2B\mu_r}{\bar{k}_p h_{pay}} * \frac{q}{\bar{P} - P_w} \tag{2.165}$$

where B is the formation volume factor, $\bar{k}_p$ is the average reservoir permeability, and h_{pay} is the pay zone thickness. The fold of productivity increase, FOI, was described as:

$$FOI = \frac{J}{J_0} \tag{2.166}$$

where J_0 is the wellbore productivity before placing the fracture.

CHAPTER III

MODEL VALIDATION

In this chapter, the model is validated and compared to analytical solutions in the literature and commercial software. The convergence of numerical solutions was studied as a function of grid sizes and time steps. The validation of geometry propagation, acid, and temperature models will be studied in the following sections.

3.1 Geometry Propagation Model Validation

To validate the fracture propagation model, the fracture height was set as constant in order to compare with the 2D PKN model. The analytical solution was then compared to the Mfrac (commercial fracture modeling software) PKN numerical solution (Meyer, 2014). Because an asymptotic solution was used to estimate the fracture width and Nolte's assumption was employed to calculate the leakoff rate, the developed analytical model did not precisely match the Mfrac numerical solution. The numerical model solved for the fracture width, including the fluid loss and storage effects, as follows (Nordgren, 1972):

$$\frac{G}{64(1-v)\mu h_f}\frac{\partial^2 w_{max}^4(x,t)}{\partial x^2} = \frac{8C_L}{\pi\sqrt{t-\tau(x)}} + \frac{\partial w_{max}(x,t)}{\partial t} \tag{3.1}$$

where G is the shear modulus. The solution difference between the two models is presented in the following section.

3.1.1 The Developed 2D Model as Compared to Mfrac

The purpose of this section is to investigate the range of differences caused by the simplification made to obtain the analytical geometry model. Five cases, each representing different fluid and rock properties at a variety of flow rates and treatment volumes, were run against the MFrac PKN numerical model. The input data for all of the cases are presented in Table 3.1. The parameters investigated were the fracture's half-length, width, net pressure, and fluid efficiency (see Figs. 3.1-3.5). The Figures show a good match between the analytical and numerical solutions in different

Table 3.1: Input Data Comparing the Analytical 2D Geometry Model with Mfrac's PKN Model

Input	**Field Unit**	**Case 1**	**Case 2**	**Case 3**	**Case 4**	**Case 5**
Injection rate, q_i	bpm	20	10	15	30	20
Injection time, t_e	min	14.2	19.3	19.4	60.4	3.47
Fluid density, ρ	$\frac{\text{lb}_\text{m}}{\text{ft}^3}$	62.4	62.4	62.4	62.4	62.4
Power law exponent, n		1	0.56	0.86	0.8	1
Consistency index, K	$\frac{\text{lb}_\text{f}.\text{s}^\text{n}}{\text{ft}^2}$	0.001	0.008	0.005	0.05	0.005
Leakoff coefficient, C_L	$\frac{\text{ft}}{(\text{min})^{.5}}$	$5\text{x}10^{-4}$	10^{-4}	10^{-3}	10^{-4}	$4\text{x}10^{-4}$
Opening time distribution factor, κ		1.5	1.5	1.5	1.5	1.5
Spurt loss, S_p	$\frac{\text{gal}}{\text{ft}^2}$	0	0	0	0	0
Young's modulus, E	Mpsi	4.5	4.5	6.5	6	6
Poisson's ratio, v		0.25	0.25	0.25	0.25	0.25
Fracture height, h_f	ft	80	50	100	100	100

case scenarios. The average differences between the analytical and numerical models ranged from 1% to 3.5%. Considering the complex behavior of fractures in field conditions and the complexity of numerically solving a strongly non-linear equation with moving boundaries (Eq. 3.1), the difference produced by the analytical model was determined to be acceptable.

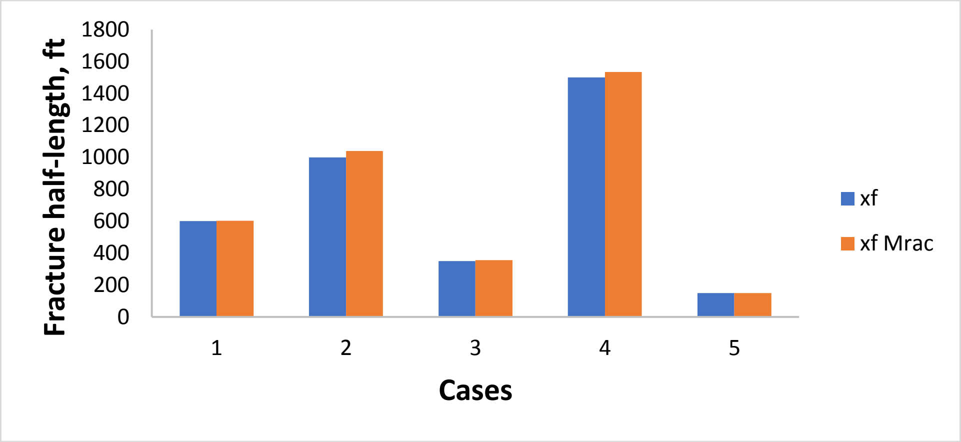

Figure 3.1: Fracture half-length comparison between the Mfrac numerical and developed analytical models for five different cases.

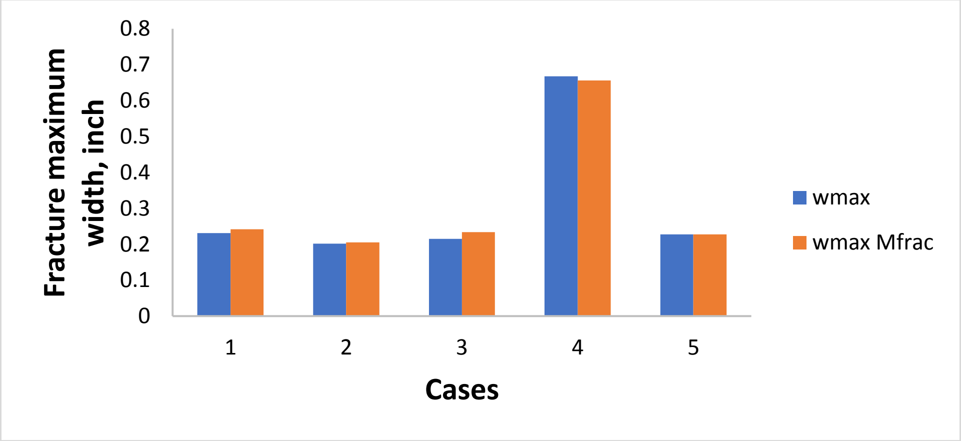

Figure 3.2: Fracture maximum width comparison between the Mfrac numerical and developed analytical models for five different cases.

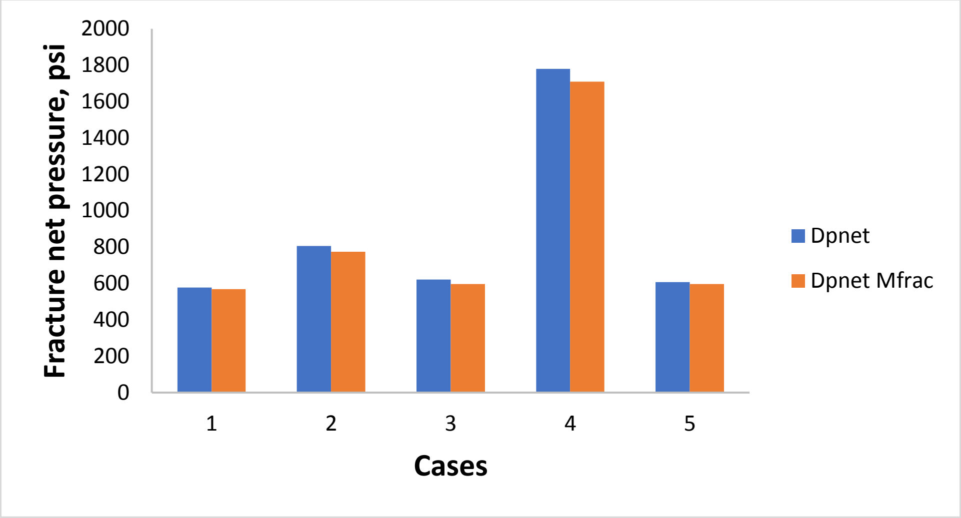

Figure 3.3: Fracture net pressure comparison between the Mfrac numerical and developed analytical models for five different cases.

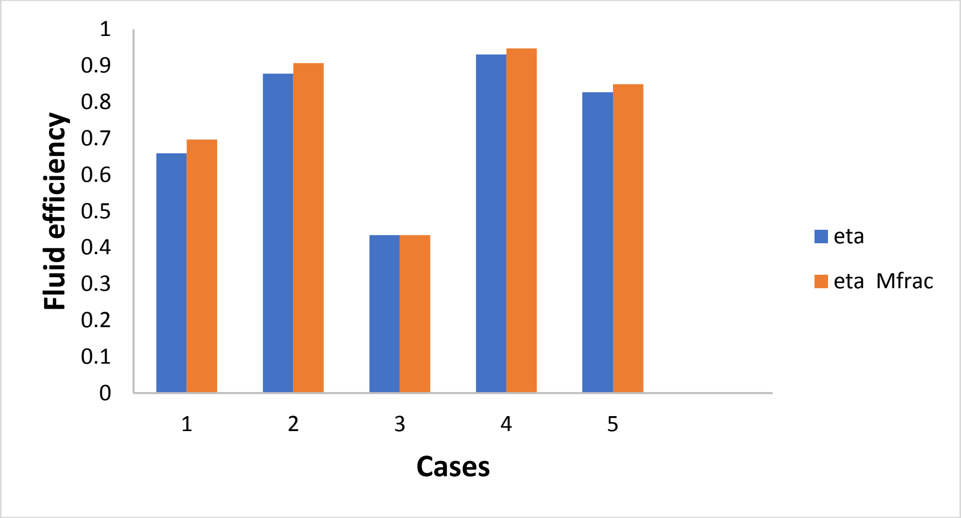

Figure 3.4: Fracture efficiency comparison between the Mfrac numerical and developed analytical models for five different cases.

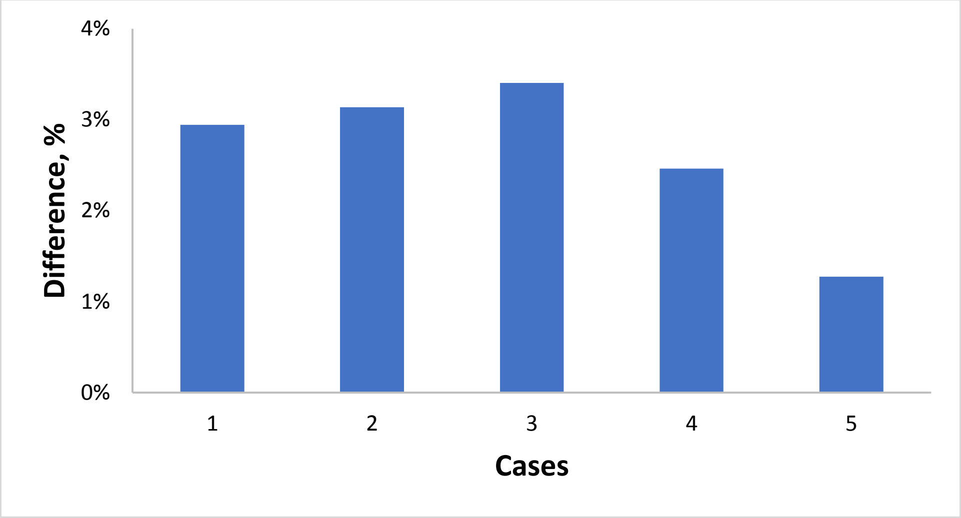

Figure 3.5: Average differences between the Mfrac numerical and developed analytical models for five different cases.

3.1.2 Multiple Fluid Approach Validation

The equivalent leakoff coefficient for multiple fluid systems was introduced to avoid having to numerically solve for a complex system of strongly non-linear equations with moving boundaries. In this section, this simplification is investigated to estimate the range of solution errors it produced. This was accomplished by running the multiple fluid system model against the single fluid model. For instance, a case with three fluid systems where each had the same fluid properties and one-third of the total injection time was run to obtain the final fracture geometry. Then, it was compared to an injection of one fluid that had the same properties and total treatment volume. Theoretically, both cases should have produced precisely the same final geometry. However, because of the approximate approach, there may have been a discrepancy in the solution.

Five different cases with different fluid properties and design parameters were run to estimate the difference caused by the approximation (see Figs. 3.6-3.9). The parameters investigated included fracture half-length, height, and maximum width. The input data used for the comparison are shown in Tables 3.2 to 3.3. The equivalent leakoff coefficient approach produced average differences ranging from 0.3% to around 3%. The approximate approach did not result in noticeable differences in fracture height and width. However, a noticeable difference in the fracture half-length was possible, especially at very low leakoff rates. That difference could

Table 3.2: Input Data for Validating the Multiple Fluid System Approach

Input	**Field Unit**	**Case 1**	**Case 2**	**Case 3**	**Case 4**	**Case 5**
Injection rate, q_i	bpm	40	20	60	10	30
Injection time, t_e	min	10	30	10	60	45
Fluid density, ρ	$\frac{\mathrm{lb_m}}{\mathrm{ft^3}}$	62.4	62.4	62.4	62.4	62.4
Power law exponent, n		0.9	0.8	0.85	0.9	0.95
Consistency index, K	$\frac{\mathrm{lb_f.\,s^n}}{\mathrm{ft^2}}$	0.005	0.001	0.03	0.05	0.0005
Leakoff coefficient, C_L	$\frac{\mathrm{ft}}{(\mathrm{min})^{.5}}$	$2\text{x}10^{-3}$	$5\text{x}10^{-4}$	$8\text{x}10^{-3}$	$9\text{x}10^{-3}$	$4\text{x}10^{-3}$
Opening time distribution factor, κ		1.5	1.5	1.5	1.5	1.5
Spurt loss, S_p	$\frac{\mathrm{gal}}{\mathrm{ft^2}}$	0	0	0	0	0
Fluid loss multiplier outside pay zone, f_m		0.25	0.25	0.25	0.25	0.25

be reduced to less than 1% for high leakoff coefficient cases. Acid fracturing is known for high leakoff rates because of the wormholes created at the fracture walls. Hence, on average, the equivalent leakoff approach for a multiple fluid system should result in less than a 1% difference for acid fracturing applications.

Table 3.3: Layer Data to Validate the Multiple Fluid System Approach

Layer Number	**Top of the Layer (ft)**	**Layer Thickness (ft)**	**Stress (psi)**	**Toughness ($\text{psi.inch}^{0.5}$)**	**Young’s Modulus (psi)**
1	0	7900	7000	1200	$4.5\text{x}10^{6}$
2	7900	100	5500	2200	$4.5\text{x}10^{6}$
3	8000	40	4000	1200	$5.5\text{x}10^{6}$
4	8040	40	4000	1000	$4.5\text{x}10^{6}$
5	8080	100	6000	2200	$5.5\text{x}10^{6}$
6	8180	500	8000	1200	$4.5\text{x}10^{6}$
Layer Number	**Poisson’s Ratio**	**Perforation**	**Minerology**	**Porosity**	**Permeability (md)**
1	0.25	No	Shale	0.10	0.10
2	0.25	No	Shale	0.10	0.10
3	0.25	Yes	Dolomite	0.10	0.10
4	0.25	Yes	Dolomite	0.10	0.10
5	0.25	No	Shale	0.10	0.10
6	0.25	No	Shale	0.10	0.10

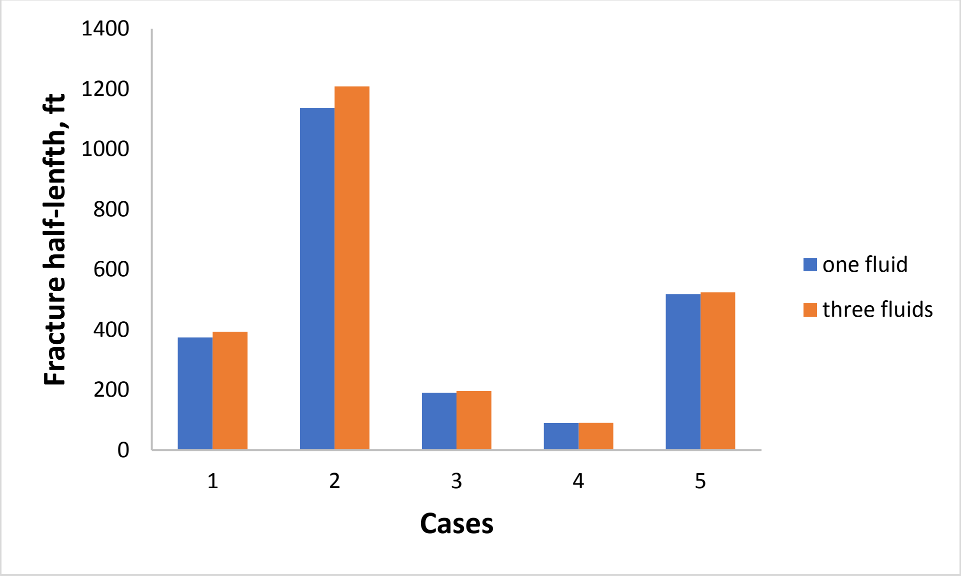

Figure 3.6: Fracture half-length comparison between one and three fluid systems for five different cases.

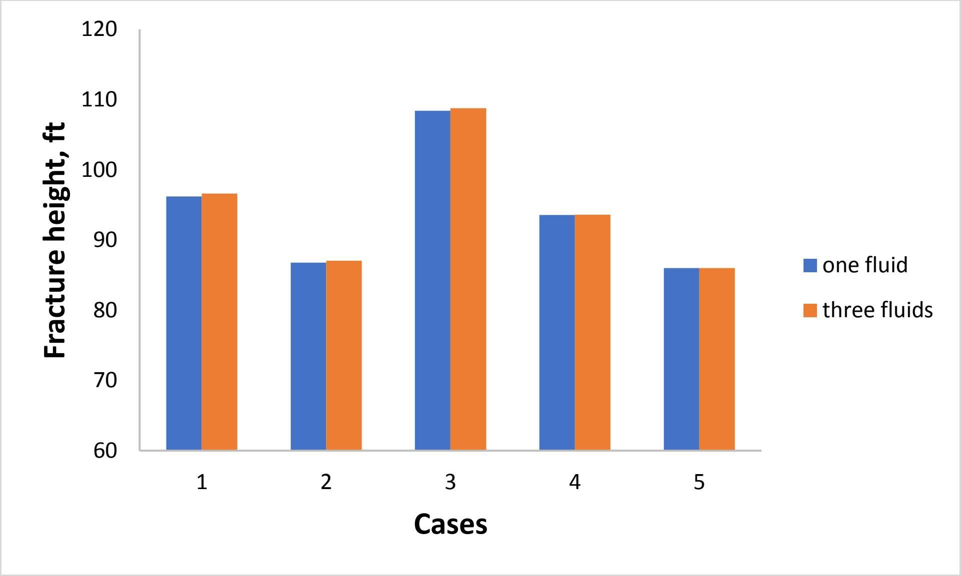

Figure 3.7: Fracture height comparison between one and three fluid systems for five different cases.

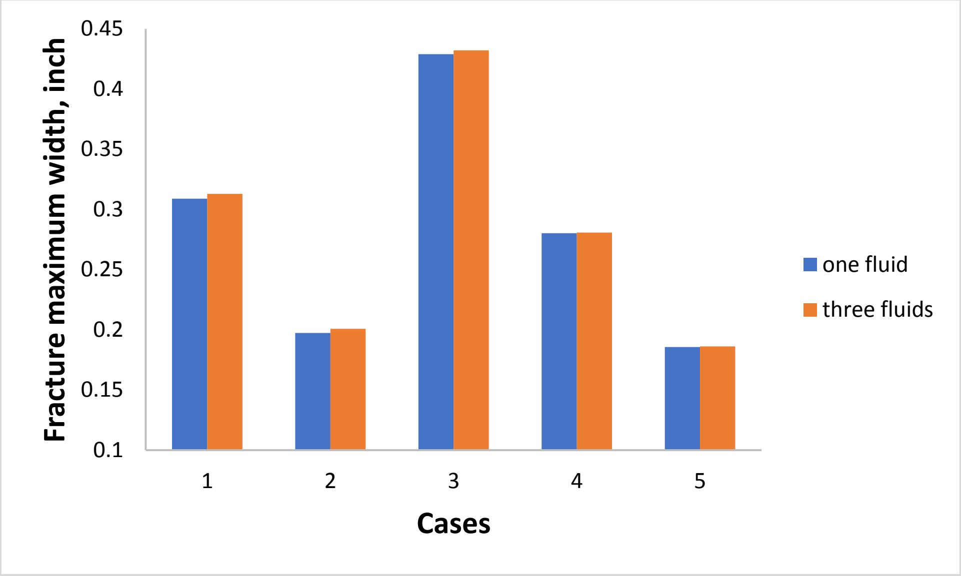

Figure 3.8: Fracture maximum width comparison between one and three fluid systems for five different cases.

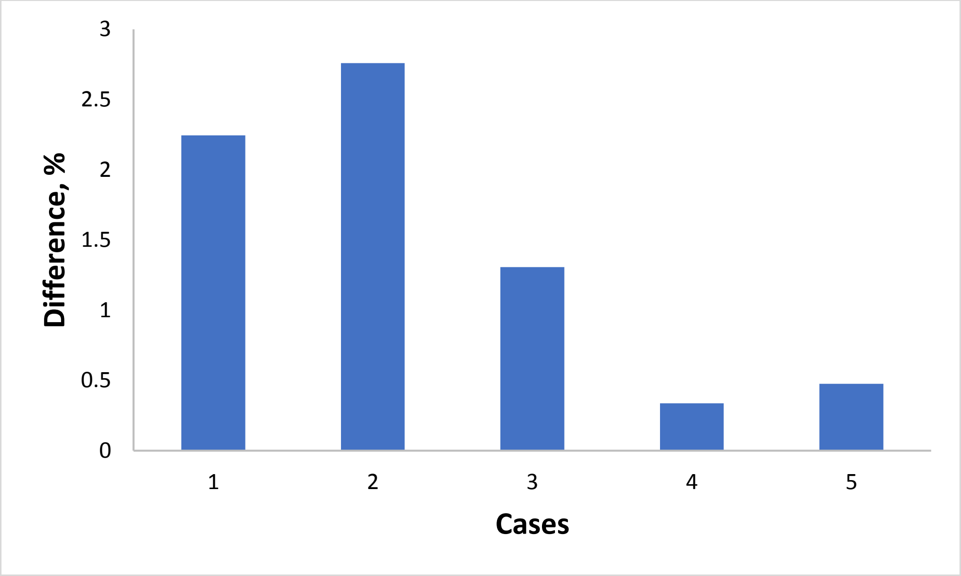

Figure 3.9: Average difference between the one and three fluid systems for five different cases.

3.2 Acid Model Validation and Convergence

One method of validating the numerical acid model was to simplify it to where it could be compared with an analytical solution. The convergence of the solution was investigated by refining the mesh size and observing the error reduction (as compared to that of a very fine mesh solution).

3.2.1 Comparison of Steady State Acid Model to Terrill's Analytical Solution

The acid model presented in Section 2.2 was simplified and compared with Terrill's analytical solution (Eq. 1.5). Assuming a steady state condition and zero acid concentration at the fracture walls (Eq. 1.4), the problem became similar to Terrill's. The model was decoupled from the

Table 3.4: Input Parameters for the Acid Model Validation

Input Data	**SI Unit**	**Field Unit**
Fracture half-length, x_f	30.5 m	100 ft
Fracture maximum width, w_{max}	0.0051 m	0.2 in
Fracture height, h_f	30.5 m	100 ft
Injection rate, q_i	0.052 m^3/s	20 bpm
Fracture fluid density, ρ	1000 Kg/m^3	62.4 lbm/ft^3
Fracture fluid viscosity, μ	0.001 Kg/(m.s)	1 cp
Initial concentration, C_i	0.15 weight fraction	
Number of x-direction grids, NX	300	
Number of y-direction grids, NY	100	

fracture geometry and temperature models to allow for an accurate comparison. To average the acid concentration at the fracture width dimension, the following formula was used:

$$\bar{C}(x) = \frac{\int uC_A(x,y)\,dy}{\int u\,dy} \tag{3.2}$$

where the trapezoidal method is implemented for numerical integration. The input data used for comparison are shown in Table 3.4.

Figure 3.10 shows the analytical and numerical acid concentration solutions, assuming a constant fracture geometry at different Peclet numbers. The Peclet number (Eq. 1.6) is the ratio of the convective to diffusive forces. A low Peclet number indicates a non-retarded acid system where diffusive forces dominate. In contrast, a high Peclet number means a retarded acid system where convective forces dominate. The numerical solution matched the analytical one but deviated at sharp gradient locations. An investigation of the root mean square errors (RMSEs) for the numerical and analytical solutions at different Peclet numbers is shown in Figure 3.11. The error decreased as the Peclet number increased, but increased at higher Peclet numbers. This behavior can be explained by the sharp acid concentration gradient at the fracture entrance for low Peclet numbers and at the fracture outlet for high Peclet numbers. The finite volume method was used to discretize the acid mass balance equation, which is the preferred method for mass conservation. However, one drawback of this method is that it makes it difficult to accurately capture steep gradients. In general, the magnitude range of the RMSE values was very small, which validated the numerical method approach. The RMSE was described mathematically, as follows:

$$RMSE = \sqrt{\frac{\sum_{i=1}^{n}\left(C(i)_{analytical} - \bar{C}(i)_{numerical}\right)^2}{n}} \tag{3.3}$$

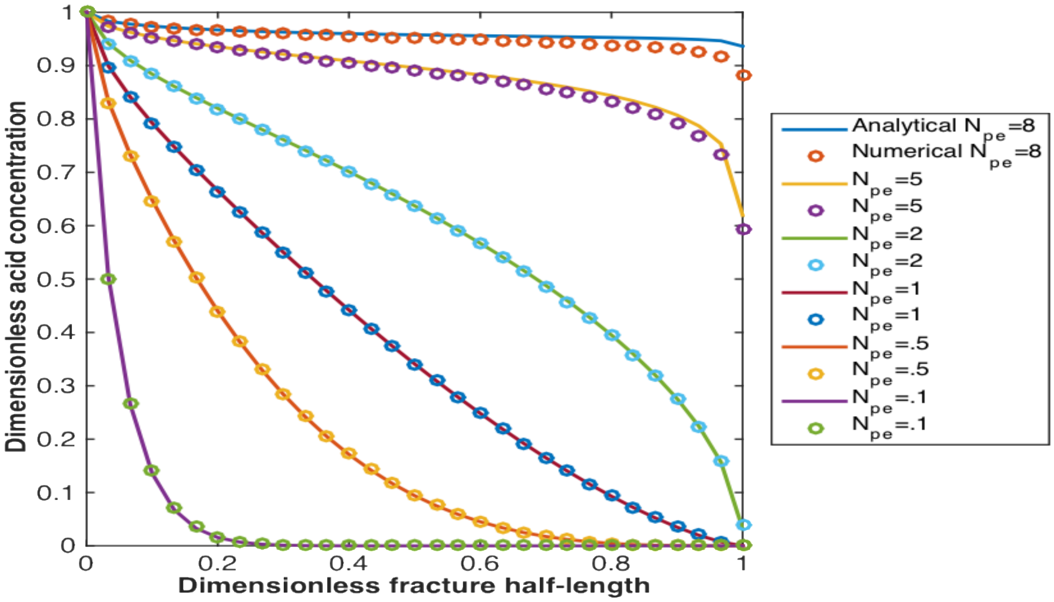

Figure 3.10: Comparison of steady state acid solutions at different Peclet numbers: numerical model and Terrill's solution.

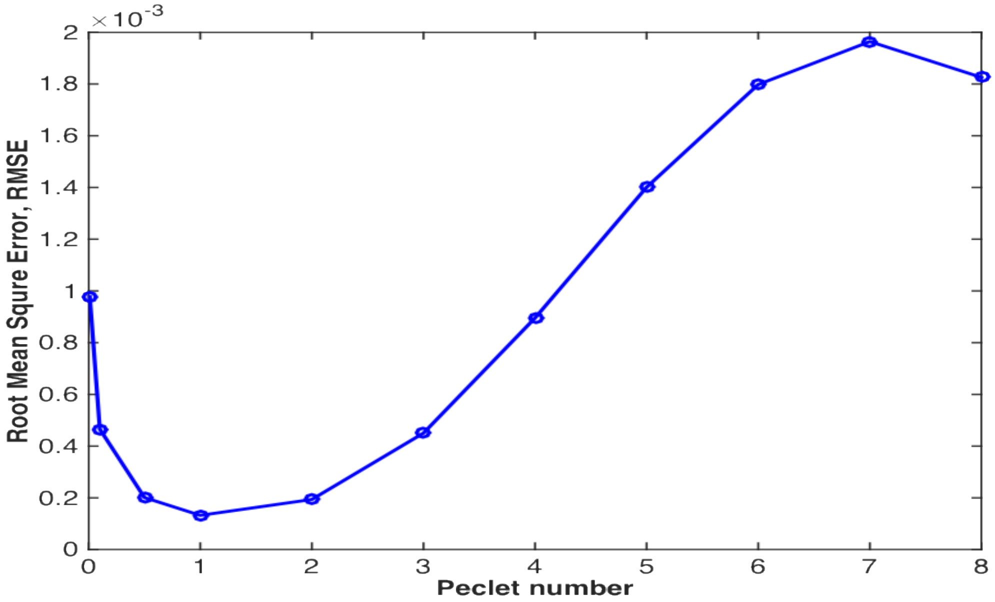

Figure 3.11: RMSE values at different Peclet numbers resulting from a comparison of the numerical and Terrill models.

3.2.2 Transient Acid Model Testing

To test the transient acid model, the model was run until reaching a steady state condition; it was then compared with Terrill's steady state solution (see Figs. 3.12-3.13). Two cases were investigated. The first represented a low Peclet number, $N_{Pe} = 0.5$, and the second represented a high Peclet number, $N_{Pe} = 5.0$. The input data used are shown in Table 3.4 and the number of time steps, Nt, was 50. The RMSE values between the final time steps and steady state solutions were 2x10^{-4} for the first case and 1.5x10^{-3} for the second. The RMSE values were reasonably low. It required 3 minutes for the solution to reach a steady state condition at the low Peclet number, and 14 minutes at the high Peclet number. Thus, the higher the Peclet number, the longer it took to reach a steady state condition.

Another factor affecting the time to reach a steady state condition was the fracture half-length. Figure 3.14 shows that at a constant $N_{Pe} = 5.0$, the longer the fracture, the more time it required to reach a steady state condition. The time to reach a steady state condition was determined based on RMSE = 1.5x10^{-3}, as compared to Terrill's steady state solution. The results imply that using a steady state solution for the acid concentration was invalid at high Peclet numbers, especially for long fractures. These results are based on a constant fracture geometry assumption. Since fractures propagate during injection, they may not reach a steady state condition during the treatment time.

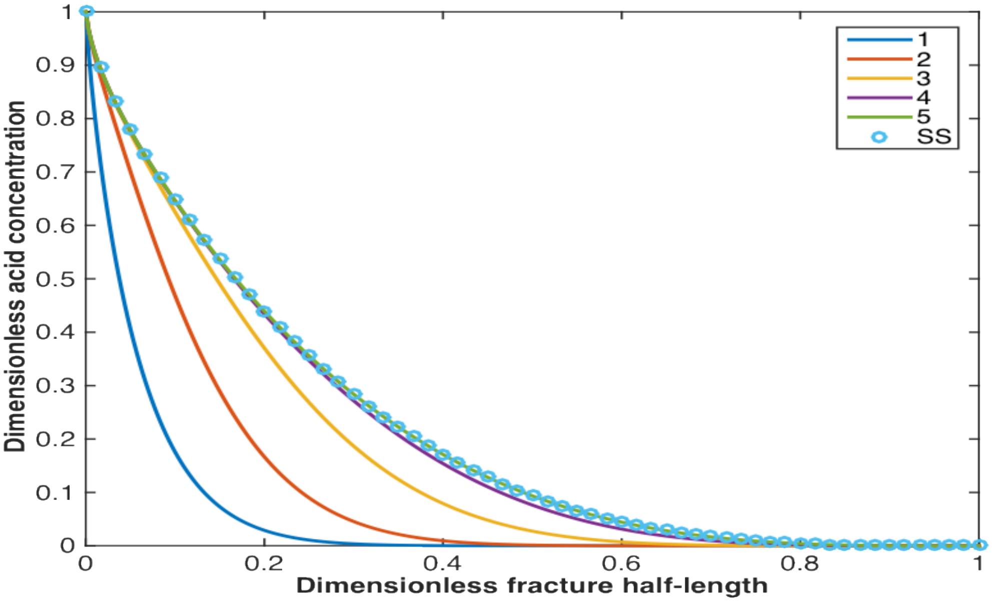

Figure 3.12: Match between the steady state in Terrill's solution and final time step of the transient numerical model at $N_{Pe} = 0.5$.

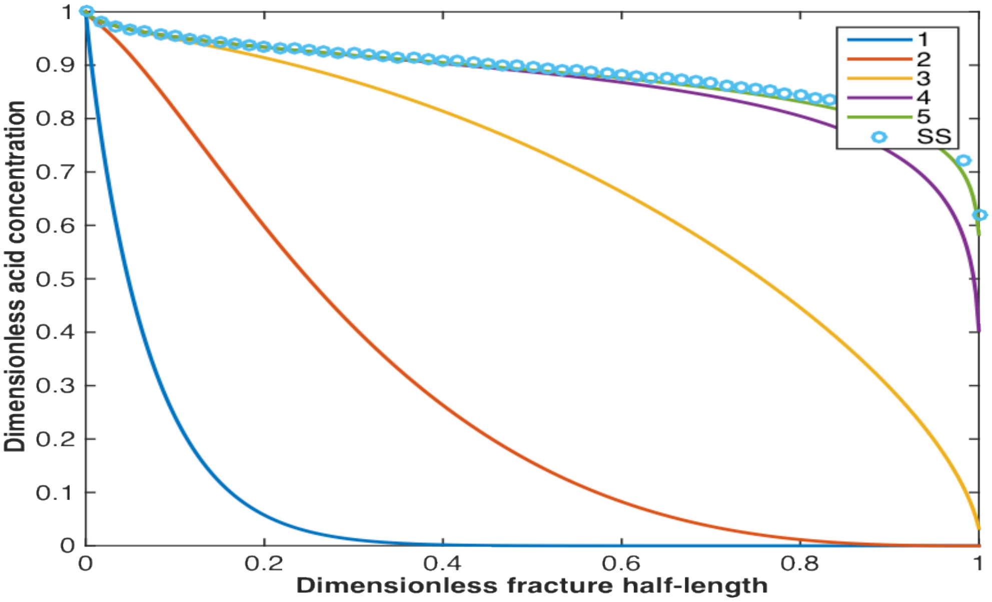

Figure 3.13: Match between the steady state in Terrill's solution and final time step of the transient numerical model at $N_{Pe} = 5$.

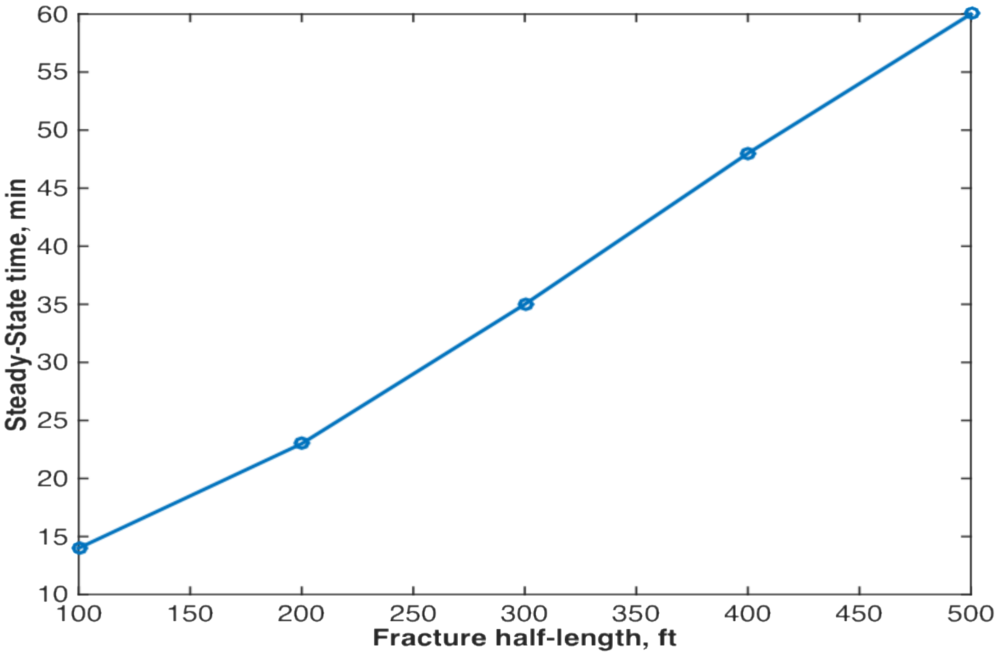

Figure 3.14: Time required for the acid solution to reach the steady state condition at different fracture half-lengths, considering $N_{Pe} = 5$.

3.2.3 Finite Reaction Acid Model Validation

In the previous sections, zero concentration at the fracture walls was applied, which is equivalent to the assumption of an infinite reaction rate. This assumption was found to be valid for the HCl acid reaction with calcite formations; however, it does not represent the reactivity of weak acids or the dolomite formations. Hence, the boundary condition shown in Eq. 2.74 was implemented; under this condition, the reactivity of the acids with different formations was characterized by the reaction rate constant, k_r, and the reaction exponent, n_r. To validate this part of the model, it was run at k_r and n_r values, representing the HCl reaction with the calcite formation (see Table 2.1). This resulted in a very fast reaction rate comparable to that of Terrill's infinite reaction rate solution. The input data for this case are shown in Table 3.4. Figure 3.15 illustrates the comparison between the finite (assuming an extremely fast reaction) and infinite approaches at $N_{Pe} = 2$; the RMSE was calculated to be approximately 1.9x10^{-4}. This small RMSE value validated the finite reaction approach used in the model.

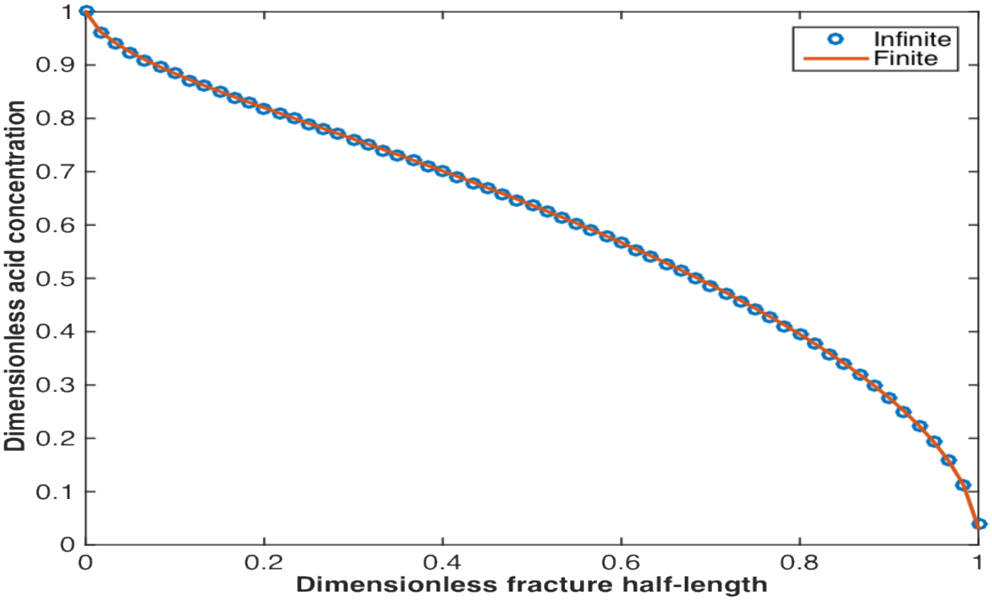

Figure 3.15: Match between the numerical finite reactivity and Terrill's infinite reactively solutions at $N_{Pe} = 2.0$.

3.2.4 Acid Etched-Width Validation

Schechter (1992) derived an analytical approach to calculate the fracture etched-width profile. The method was based on Terrill's analytical solution for acid concentration. The method used in this work was based on numerically resolving the acid concentration across the fracture width (Eq. 2.106). The comparison between the models in this section uses steady state, infinite reactivity, and constant geometry assumptions. The input data for Table 3.4 were used for this simulation, in addition to the input data from Table 3.5, which were used for the acid etched-width calculations. Figure 3.16 shows the etched-width profile comparison between Schechter's solution and the numerical model presented at different Peclet numbers. The Figure shows a good match between the models, except at the fracture entrance.

Table 3.5: Input Parameters for Acid Etching Validation

Input Data	SI unit	Field Unit
Injection time, t_e	6000 s	100 min
Dissolving power, β	1.37 unit mass $CaCO_3$/unit mass HCl	
Rock density, ρ_r	2710 Kg/m^3	169.1 lbm/ft^3
Formation porosity, φ	0.1 pore volume/total volume	

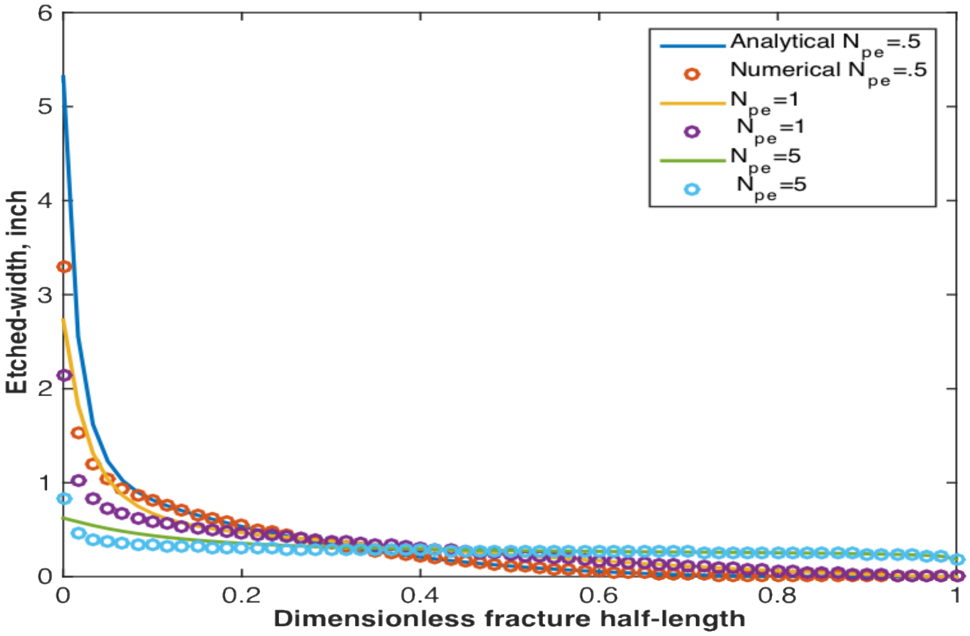

Figure 3.16: Match between the numerical and analytical acid-etched width profiles at different Peclet numbers.

The analytical and numerical models were also compared by investigating the conservation of acid mass at different Peclet numbers. The exact volume of rock that a certain volume of acid can dissolve is:

$$V_{rock} = \frac{\chi}{1-\varphi} q_i t_e C_i \tag{3.4}$$

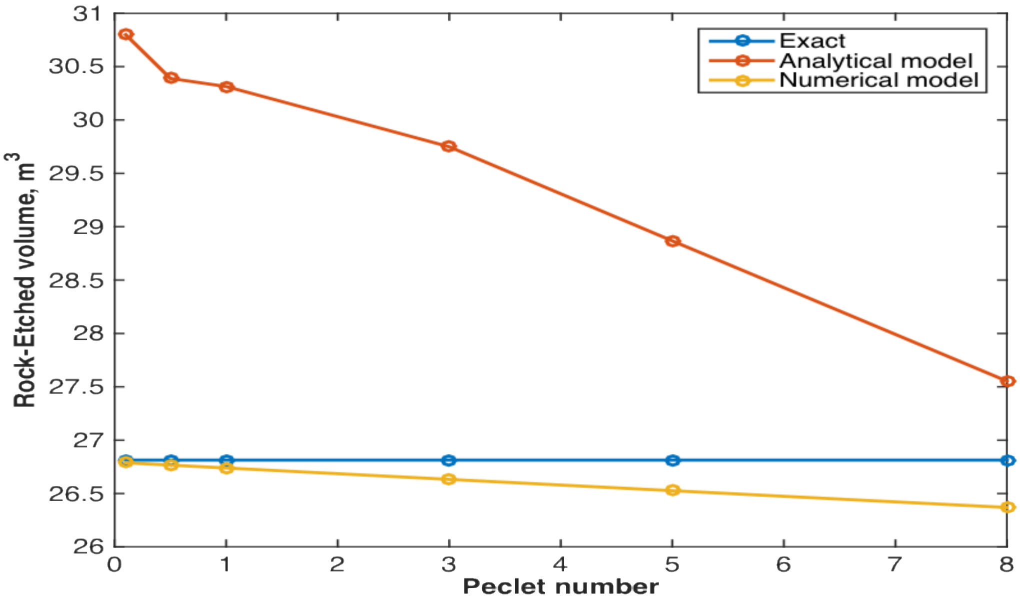

Figure 3.17: Acid mass conservation values for the analytical and numerical models compared to the exact solutions at different Peclet numbers.

To calculate the volume of rock dissolved in the analytical and numerical models, the etched-width versus fracture half-length curves were numerically integrated. Figure 3.17 shows that the numerical model conserved the acid mass better than the analytical model did. Figure 3.18 indicates that the maximum error produced by the developed numerical model was less than 2%, but did go up to 15% in the analytical model case. To reduce the error produced by the numerical model to less than 1%, a larger number of grid blocks in the fracture width direction needed to be generated. The error was calculated as follows:

$$Error = \frac{\left|V_{rock,model} - V_{rock,exact}\right|}{V_{rock,exact}} * 100 \qquad (3.5)$$

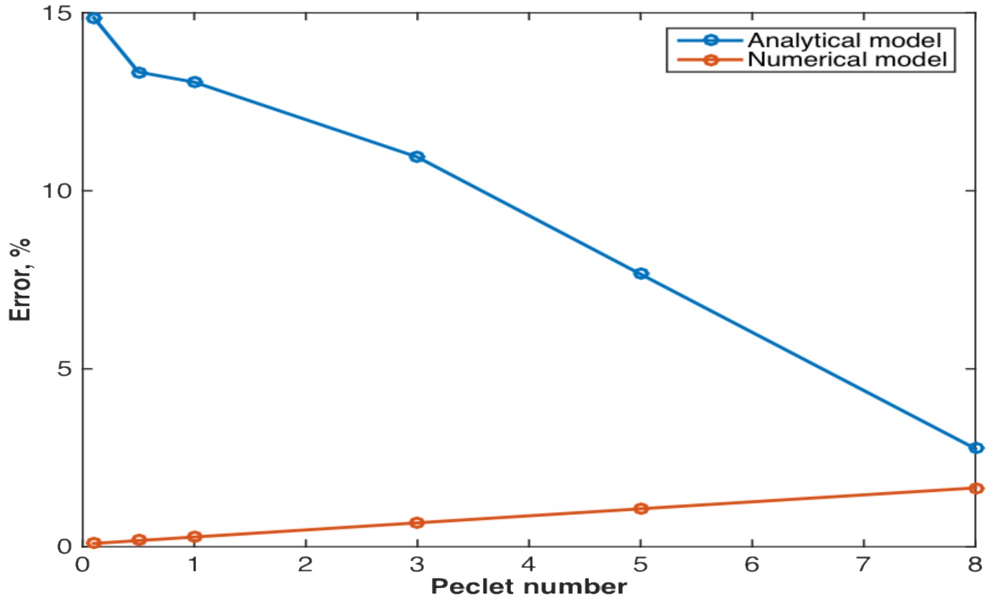

Figure 3.18: Acid mass conservation errors produced by the analytical and numerical models at different Peclet numbers.

3.2.5 Acid Model Convergence

An implicit scheme was used to solve for the acid concentration. The differential equation was linear where the wall boundary condition was the only source of non-linearity. Linearization of the wall boundary condition required using the concentration from the previous time step. The scheme formulation and boundary condition linearization are shown in Appendix A. The implicit convection diffusion problem was unconditionally stable. The convergence of the solution was investigated by refining the grid blocks sizes and time steps. The input data from Table 3.4 were used for this study. Figure 3.19 shows the acid solutions at $N_{Pe} = 0.1$ for different numbers of x-direction grid blocks, NX. Figure 3.20 shows the RMSE as NX increased at both low and high Peclet numbers. The RMSE was calculated against the most refined solution, which was at $NX = 18{,}750$ in this case. The solution converged as NX increased, but the convergence rate was faster at higher Peclet numbers. This implies that high Peclet number solutions require less NX to converge, as compared to lower Peclet numbers.

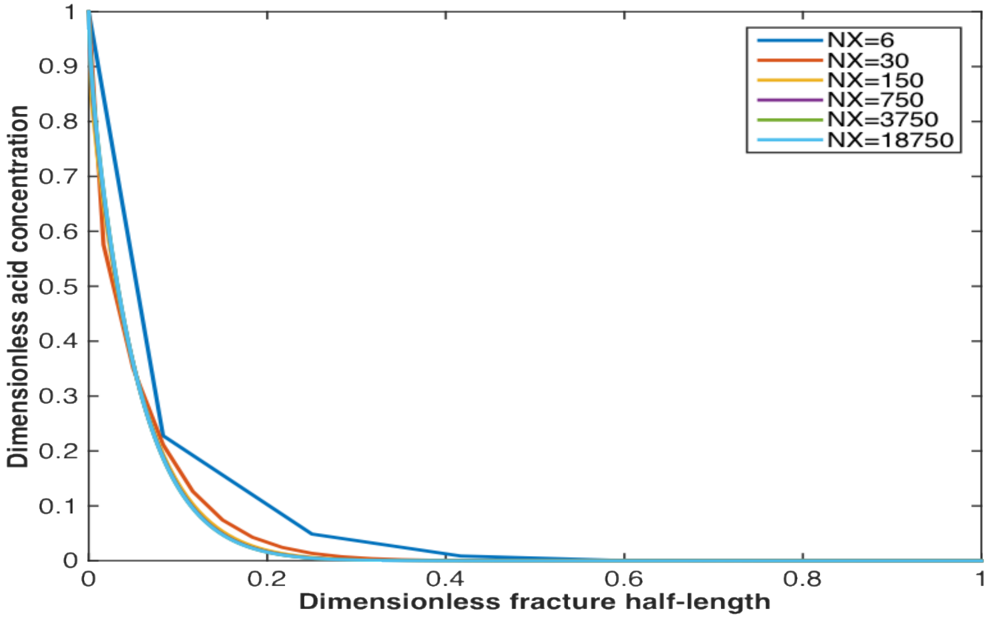

Figure 3.19: Acid solutions at different NX values for $N_{Pe} = 0.1$.

The solution convergence against the number of grid blocks in the fracture width direction, NY, at high and low Peclet numbers was also investigated. Figure 3.21 shows the acid concentration across the fracture width at the second grid block from the fracture entrance. Figure 3.22 shows the RMSE as the NY increased at low and high Peclet numbers. The RMSE values were calculated against the most refined solution, which was $NY = 6{,}250$ in this case. The solution converged as the NY increased, but the convergence rate was faster at lower Peclet numbers. This implies that solutions using higher Peclet numbers will require more NY to converge than will lower Peclet numbers. The reason is that the higher Peclet number cases show sharper acid gradient across the width, which require more NY to capture the behavior.

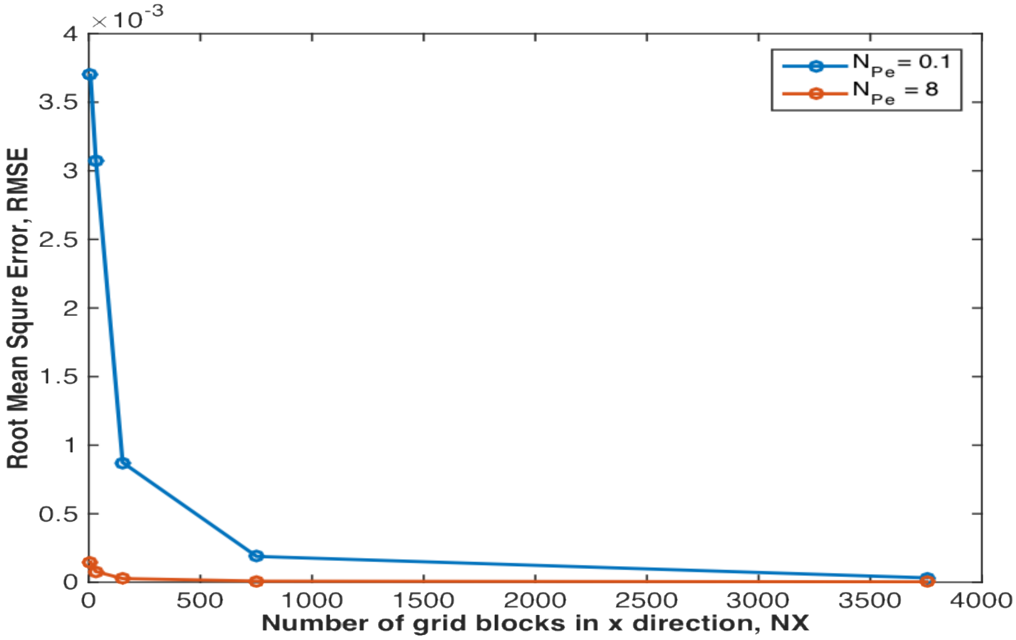

Figure 3.20: Solution convergence versus NX at high and low Peclet numbers.

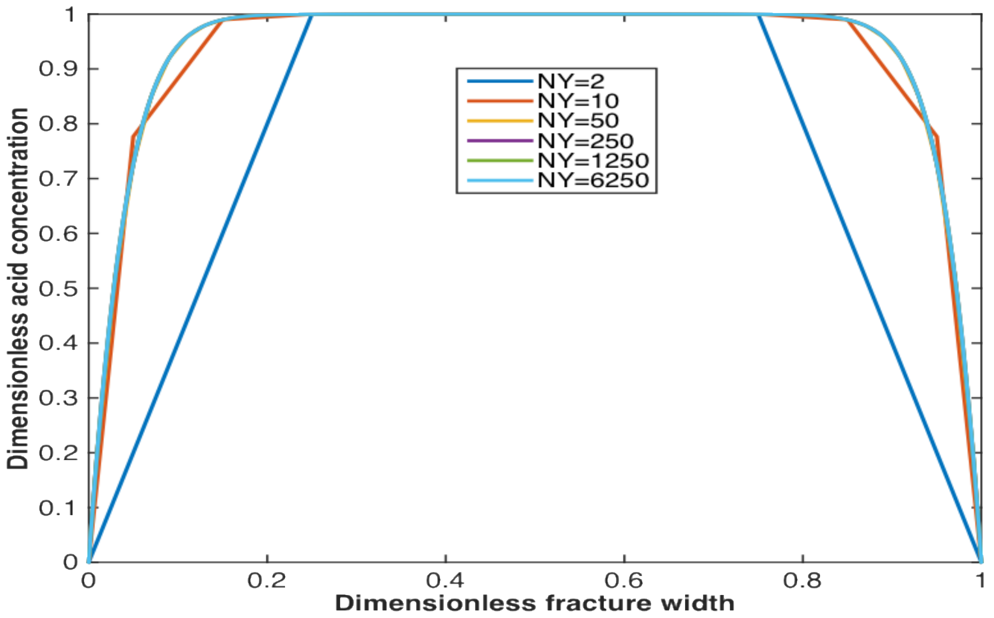

Figure 3.21: Second grid block from the fracture entrance acid solutions across fracture width at different NY values for $N_{Pe} = 8$.

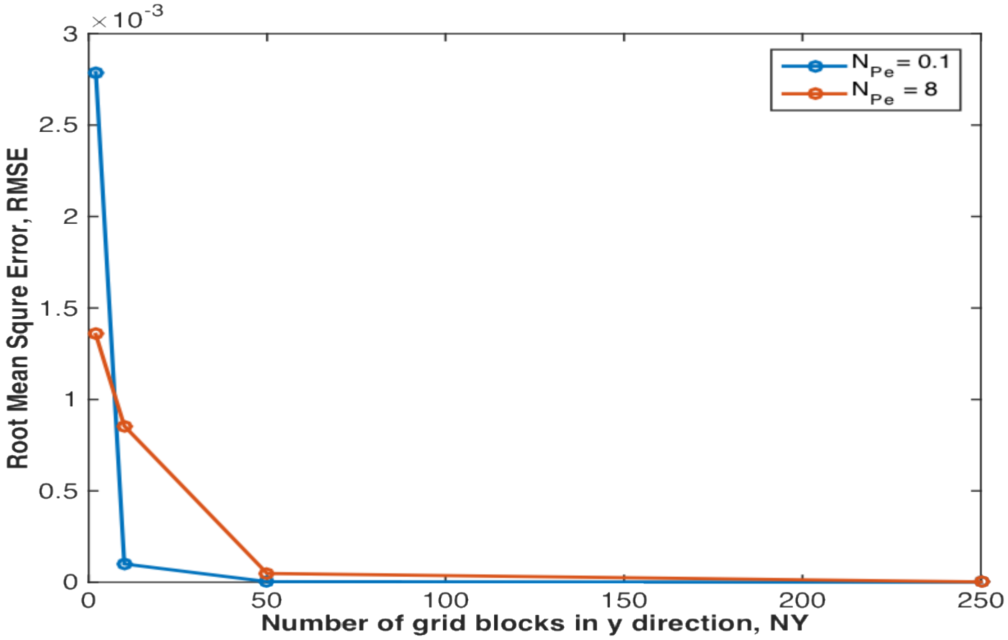

Figure 3.22: Solution convergence versus NY at high and low Peclet numbers.

The convergence of the acid solution against the number of time steps, Nt, was also studied. It was determined that the convergence rate depended on the acid flow condition. If the injection time was long enough for the acid solution to reach a steady state condition, the solution converged immediately (at $Nt = 1$). However, if the acid flow was still in a transient condition during the injection time, the convergence rate was slower. Figure 3.23 shows the solution after 1 minute of acid injection at $N_{Pe} = 5.0$ for different Nt values. The acid solution was transient, and showed a strong function of Nt.

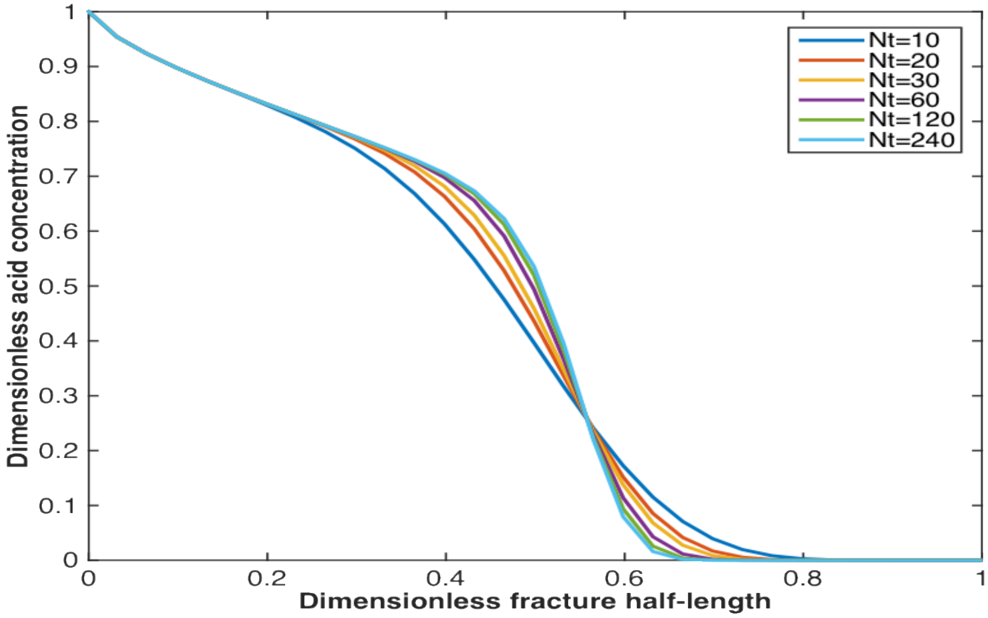

Figure 3.23: Transient acid solutions after 1 minute of acid injection at different Nt values for $N_{Pe} = 5$.

Figure 3.24 illustrates the RMSE as the Nt increased at transient and steady state conditions. The RMSE was calculated against the most refined solution, in this case $Nt = 240$.

The solution converged as Nt increased for the transient solution, but the solution did not show dependence on Nt for the steady state solution. The reason was that the transient solution was a strong function of the previous time step solution. However, the steady state solution could be predicted even without this knowledge. If a constant fracture geometry is assumed, it will take a longer time to reach a steady state condition when the Peclet number is high. When the fracture geometry propagates, the solution may not reach a steady state condition. Hence, a larger Nt was required to model the transient acid concentration solution.

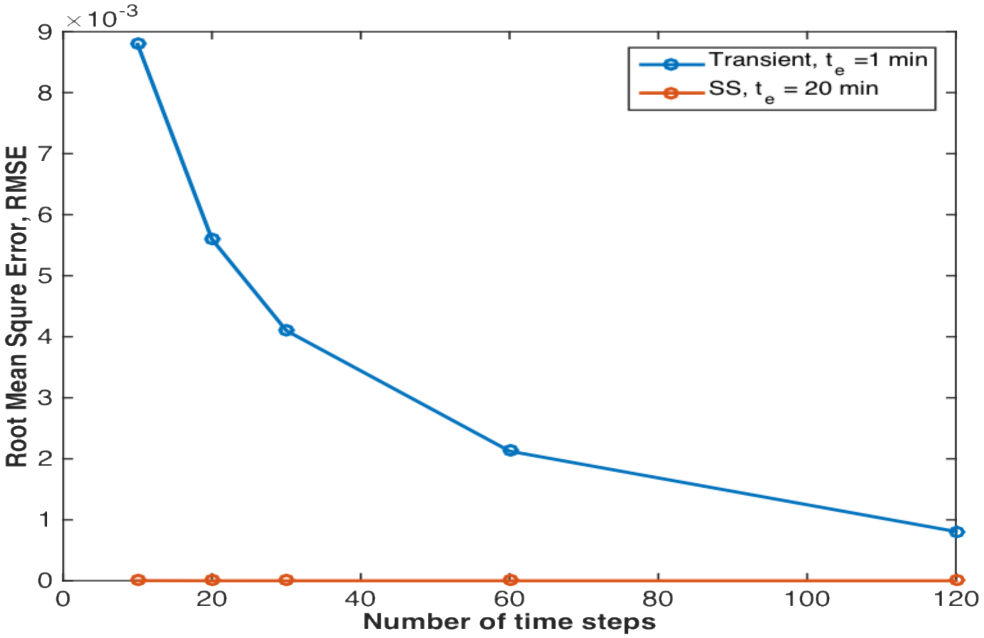

Figure 3.24: Solution convergence at different Nt values for the transient and steady state flow conditions for $N_{Pe} = 5$.

3.3 Temperature Model Validation and Convergence

The heat transfer equation is an analog to the acid mass balance equation. The same numerical scheme was used for both problems. Terrill's analytical solution was originally developed for the heat transfer problem of fluid flowing between parallel porous plates; it was then adopted for the analog acid mass conservation problem. The numerical convergence of the temperature solution as meshes or time steps was refined to be like that of the concentration solution (see Section 3.2.5).

Even though the temperature model could be validated against Terrill's steady state solution, it was validated against another transient analytical solution. The simple solution was presented by Seth et al. (2010) and assumed no fluid loss and a constant reservoir temperature. The 1D heat transfer equation was as follows:

$$\rho c_p \left(\frac{\partial T}{\partial t} + u \frac{\partial T}{\partial x} \right) = \frac{2}{\overline{w}} \left[h_l (T_R - T) \right] \tag{3.6}$$

where h_l is the heat transfer coefficient at the fracture face. The first term represents the heat accumulation, the second indicates the heat convection inside the fracture, and the third is the heat flux from the constant temperature reservoir. The problem was solved using a Laplace transformation, by defining the following initial and boundary conditions:

$$T(x, t = 0) = T_R \tag{3.7}$$

$$T(x = 0, t) = T_I \tag{3.8}$$

Initially, the temperature everywhere was equal to the reservoir temperature, T_R, while at the fracture inlet, the temperature was equal to the injected fracture fluid temperature, T_I. The fracture temperature solution as a function of time and position was:

$$\begin{cases} T_D = 0 & x - ut > 0 \\ T_D = e^{-x\frac{\eta}{u}} & x - ut < 0 \end{cases} \tag{3.9}$$

where:

$$T_D = \frac{T_R - T}{T_R - T_I} \tag{3.10}$$

$$\eta = \frac{2h_l}{\rho c_p \overline{w}} \tag{3.11}$$

The 1D analytical solution was compared to the 2D numerical model, after being simplified to the following governing equation:

$$\rho c_p \left(\frac{\partial T}{\partial t} + u\frac{\partial T}{\partial x}\right) = k\frac{\partial^2 T}{\partial y^2} \tag{3.12}$$

To totally describe the problem, initial and boundary conditions should be specified. Initially, the temperature was equal to the reservoir temperature:

$$T(x, y, t = 0) = T_R \tag{3.13}$$

At the fracture inlet, the temperature was equal to the injected fracture fluid temperature:

$$T(x = 0, y, t) = T_I \tag{3.14}$$

At the fracture walls, heat conducted from the reservoir was equal to the heat convected to the fracture.

$$k\left.\frac{\partial T}{\partial y}\right|_w = h_l(T_R - T) \tag{3.15}$$

The 2D solution was averaged to 1D by the following formula:

$$\bar{T}(x) = \frac{\int uT(x,y)dy}{\int udy} \tag{3.16}$$

where $\bar{T}$ is the average temperature. The input data in Table 3.6 was used to compare the two solutions. Figure 3.25 shows the matches between the models where the average error was less than 1%. The error was calculated as follows:

$$Error = \frac{\left|T_{analytical} - T_{numerical}\right|}{T_{analytical}} * 100 \tag{3.17}$$

The 2D solution exactly matched the 1D analytical solution when small values were used for the average fracture width. Figure 3.26 shows the errors between the models along the fracture half-length.

Table 3.6: Input Parameters for Temperature Model Validation

Input Data	**SI Unit**	**Field Unit**
Fracture half-length, x_f	30.5 m	500 ft
Fracture maximum width, w_{max}	0.0051 m	0.1 inch
Fracture height, h_f	30.5 m	100 ft
Injection rate, q_i	0.052 m^3/s	20 bpm
Injection time, t_e	6000 s	100 min
Fracture fluid density, ρ	1000 Kg/m^3	62.4 lbm/ft^3
Fracture fluid viscosity, μ	0.001 Kg/(m.s)	1 cp
Fracture fluid heat capacity, c_p	4.13 KJ/(Kg.^oC)	0.964 Btu/(lbm.^oF)
Fracture fluid thermal conductivity, k	$6x10^{-4}$ KJ/(m.s.^oC)	0.347 Btu/(hr.ft. ^oF)
Heat transfer coefficient, h_l	$60x10^{-3}$ KJ/(m^2.s.^oC)	10.57 Btu/(hr.ft^2.^oF)
Fracture fluid temperature, T_I	25 ^oC	77 ^oF
Reservoir temperature, T_R	100 ^oC	212 ^oF
Number of x-direction grids, NX	1500	
Number of y-direction grids, NY	100	
Number of time steps, Nt	50	

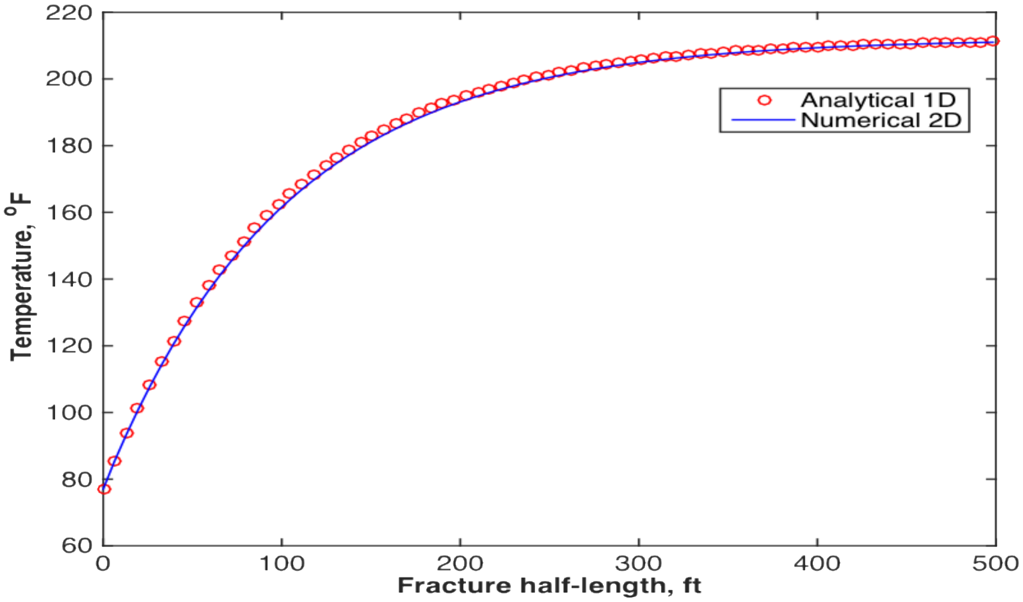

Figure 3.25: Match between the 1D analytical and 2D numerical temperature solutions.

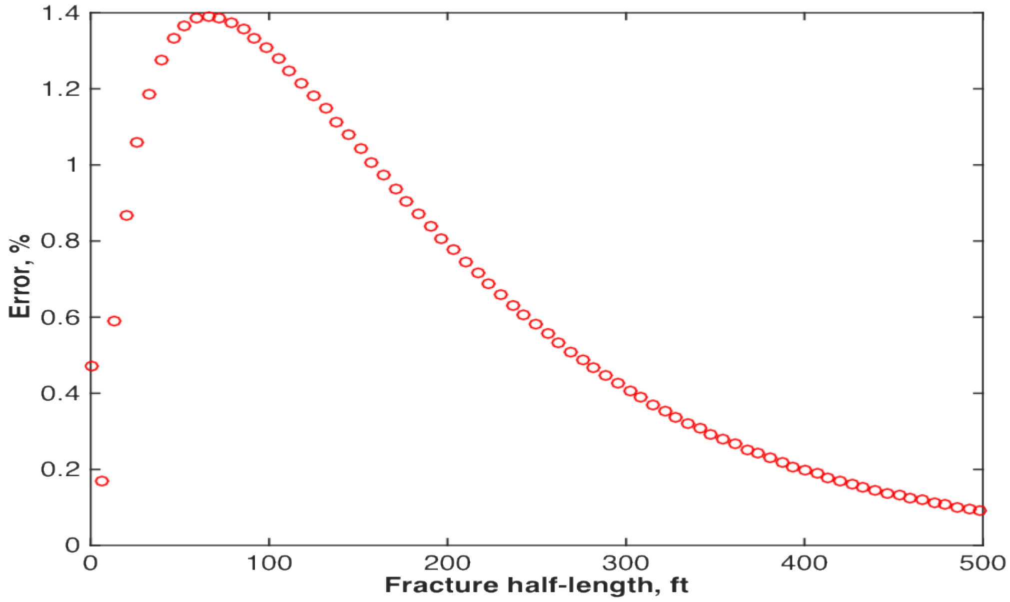

Figure 3.26: Solution differences between the 1D analytical and 2D numerical models along the fracture half-length.

CHAPTER IV

PARAMETRIC STUDY*

In this chapter, the effects of the design parameters on acid solutions are described. The studied parameter was changed while keeping the other parameters constant. This helped in understanding the relationships among the design parameter, acid etching behavior, and penetration length, which eventually affected the fracture productivity. The input data for the reservoir, wellbore, and acid properties used in this chapter are shown in Table 4.1. This table also includes the Mou-Deng correlation's constants, grid blocks, and time step sizes. The input data for the formation layers' properties are shown in Table 4.2. The reaction constants of calcite and dolomite with HCl acid are shown in Table 2.1.

Table 4.1: Input Data Used for the Parametric Study

Input Data	SI Unit	Field Unit
Wellbore Properties		
Wellbore radius, r_w	0.104 m	0.34 ft
Inner casing radius, r_1	0.0628 m	2.475 inch
Outer casing radius, r_2	0.0699 m	2.75 inch
Overall heat transfer coefficient, U_t	0.8 KJ/(s.m^2.^{o}C)	0.039 Btu/(hr.ft^2.^{o}F)
Ambient temperature, T_b	25 ^{o}C	77 ^{o}F
Reservoir/Formation Properties		
Reservoir pressure, P_r	2.0684x10^7 pa	3000 psi
Bottomhole pressure, P_w	1.0342x10^7 pa	1500 psi

---

* Part of this section is reproduced with permissions from "Temperature and Geometry Effects on the Fracture Surfaces Dissolution Patterns in Acid Fracturing" by Aljawad, M.S., Zhu, D. and Hill, A. D. 2018. Copyright 2018, Society of Petroleum Engineers. Further reproduction prohibited without permission.

Table 4.1: Continued

Input Data	SI Unit	Field Unit
Formation fluid density, ρ_f	850 Kg/m^3	54 lb$_m$/ft^3
Reservoir length, L_x	1000 m	3280 ft
Reservoir width, L_y	1000 m	3280 ft
Formation fluid viscosity, μ_f	0.0008 Kg/(m.s)	0.8 cp
Formation volume factor, B	1.3 volume at reservoir conditions/volume at standard conditions	
Total compressibility, c_t	2.26x10^{-9} pa^{-1}	1.56x10^{-5} psi^{-1}
Reservoir temperature, T_R	100 ^{o}C	212 ^{o}F
Formation rock density, ρ_{ma}	2600 Kg/m^3	162.24 lb$_m$/ft^3
Formation specific heat capacity, c_{ma}	0.879 KJ/(Kg. ^{o}C)	0.2099 Btu(lb.^{o}F)
Formation thermal conductivity, k_{ma}	1.57x10^{-3} KJ/(s.m. ^{o}C)	0.907 Btu/(hr.ft.^{o}F)
Acid Properties		
Density, ρ	1000 Kg/m^3	62.4 lb$_m$/ft^3
Injection rate, q_i	0.08 m^3/s	30 bpm
Treatment time, t_e	900 s	15 min
Power law exponent, n	0.9	
Consistency index, K	0.002 lb$_f$.s^n/ft^2	
Spurt loss, S_p	0 m	0 gal/ft^2
Fluid loss multiplier outside pay zone, f_m	0.25	
Opening time distribution factor, κ	1.5	
Acid initial concentration, C_i	0.15 mass HCl/mass solution	
Acid heat capacity, c_p	4.13 KJ/(Kg.^{o}C)	0.964 Btu/(lbm.^{o}F)
Acid thermal conductivity, k	6x10^{-4} KJ/(s.m. ^{o}C)	0.347 Btu/(hr.ft. ^{o}F)
Acid temperature at surface, T_s	27 ^{o}C	80.6 ^{o}F
Mou-Deng Conductivity Correlation Parameters		
Horizontal correlation length, $\lambda_{D,x}$	1.0	
Vertical correlation length, $\lambda_{D,z}$	0.05	
Normalized permeability standard deviation, σ_D	0.4	
Grid Blocks and Time Step Size		
Size of x-direction grids, DX	1 m	3.28 ft
Number of y-direction grids, NY	100	
Number of z-direction grids, NZ	8	
Number of time steps, Nt	100	

Table 4.2: Layer Input Data for the Parametric Study

Layer Number	**Top of Layer (ft)**	**Layer Thickness (ft)**	**Stress (psi)**	**Toughness (psi.inch$^{0.5}$)**	**Young's Modulus (psi)**
1	0	7900	6000	1200	$4.5\text{x}10^6$
2	7900	100	5500	2200	$4.5\text{x}10^6$
3	8000	60	4200	1200	$5.5\text{x}10^6$
4	8060	60	4000	1000	$4.5\text{x}10^6$
5	8120	40	4500	1200	$5.5\text{x}10^6$
6	8160	500	6000	2200	$4.5\text{x}10^6$
Layer Number	**Poisson's Ratio**	**Perforation**	**Minerology**	**Porosity**	**Permeability (md)**
1	0.25	No	Shale	0.10	1.5
2	0.25	No	Shale	0.08	1.2
3	0.25	Yes	Calcite/Dolomite	0.15	1.0
4	0.25	Yes	Calcite/Dolomite	0.14	1.0
5	0.25	No	Shale	0.13	0.5
6	0.25	No	Shale	0.10	0.1

4.1 Fracture Geometry

The fracture width and height have significant impacts on the acid etched-width distribution. Formation rock properties and stress distribution control the fracture dimensions and orientation. The injection condition such as fluid viscosity and injection rate, can also impact fracture propagation.

Assuming constant fracture dimensions, the effect of the fracture width on the acid penetration length and etched-width profile was investigated. The range of the fracture maximum widths ranged from .05 to 0.5 inches, while keeping 120 ft of fracture height, 300 ft of fracture half-length, and a 5×10^{-4} cm^2/s acid diffusion coefficient in calcite formation. The other input data are shown in Table 4.1. Figure 4.1 indicates that increasing the fracture width enhances the acid penetration distance and creates less etching at the fracture entrance (i.e., more uniform etching). It can be stated that the acid residence time is longer inside a wider fracture segment due to the lower injection velocity of a given injection rate. A longer residence time leads to acid consumption before a further distance is traveled, resulting in a shorter acid penetration length. However, the acid diffusion effect is more prominent where the acid is diffused at a slower rate, towards the reactive walls of wider fractures; overall, this results in a slower reaction rate and longer acid penetration length.

Similarly, the fracture height was studied assuming constant geometry over the treatment time. The range of the studied fracture height was from 40 to 200 ft, assuming a 0.2 maximum fracture width and 300 ft fracture half-length. As the fracture height increased, the acid penetration length decreased (see Fig. 4.2). At a given injection rate, the average acid velocity was slower when the fracture height was larger, resulting in a longer acid residence time and faster consumption of the acid. The maximum etched width decreased as well, because the acid was distributed over a larger area of fracture surfaces.

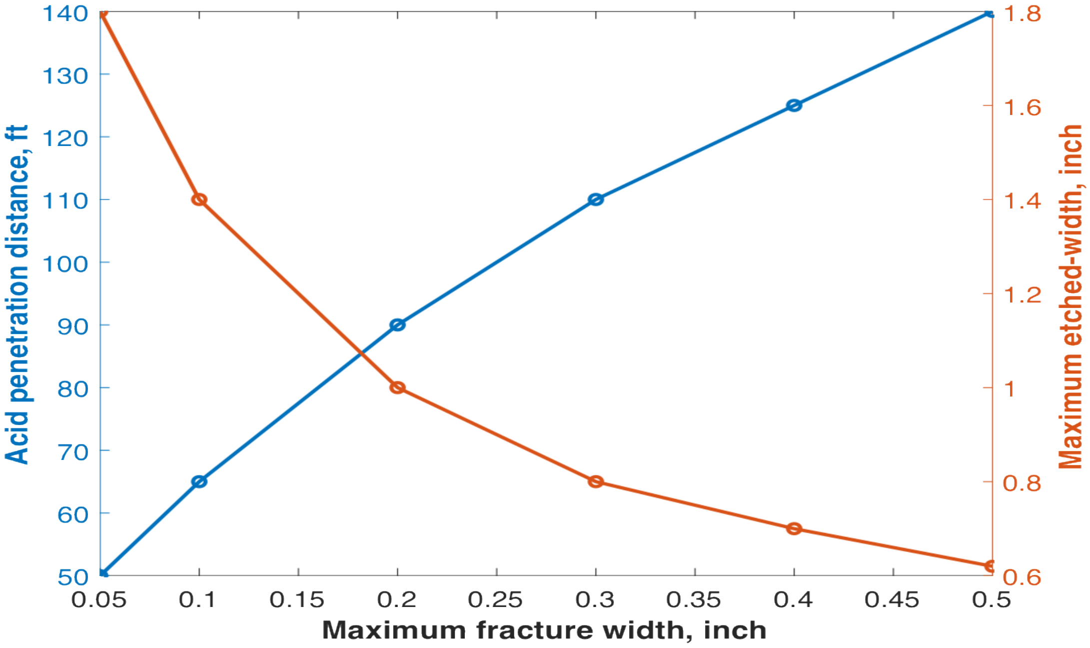

Figure 4.1: Fracture width effects on acid penetration distance and etched-width distribution.

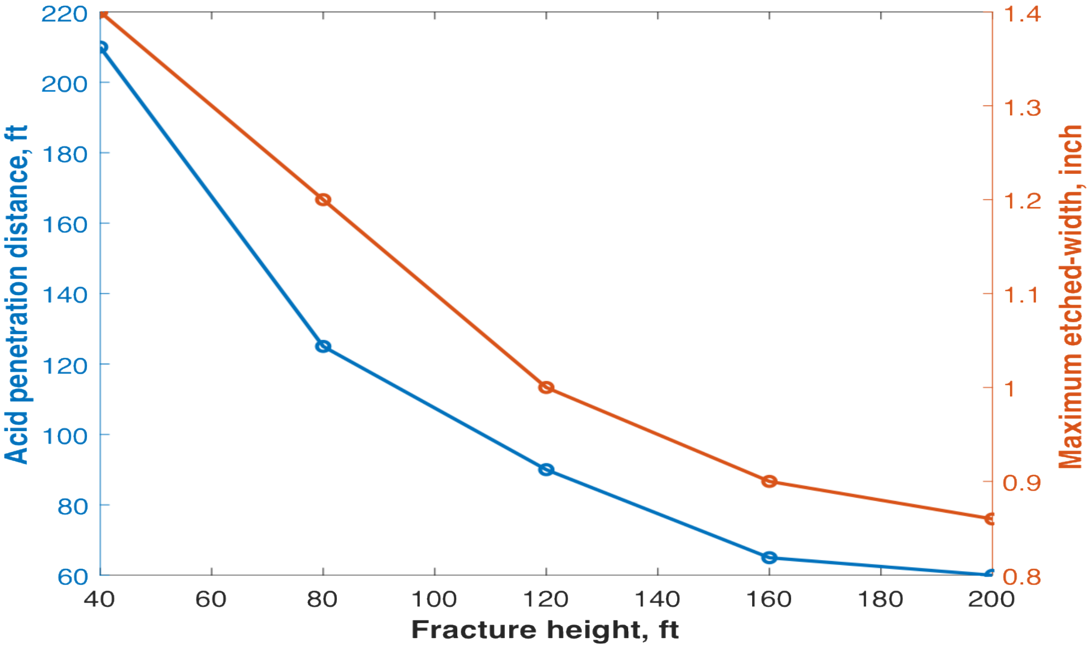

Figure 4.2: Fracture height effects on acid penetration distance and etched-width distribution.

4.2 Acid Diffusion Coefficient

The acid diffusion flux in a mixture depends on the magnitude of the acid concentration gradient and diffusion coefficient (Eq. 2.60). A higher acid diffusion coefficient leads to a higher acid flux rate. The viscosity of an acid system inversely affects the diffusion coefficient. For instance, straight acid is known for having a higher diffusion coefficient compared to more viscous gelled or emulsified acids. In contrast, temperature proportionally affects the diffusion coefficient. Figure 4.3 shows the effects of the diffusion coefficient's magnitude on the acid penetration length and maximum etched-width, assuming a calcite formation. The model predicted the fracture half-length to be approximately 230 ft, using the input data listed in Tables 4.1 and 4.2. The reaction between the HCl acid and calcite formation can be described as diffusion limited, which means that the reaction rate at the fracture surface is extremely fast and only the acid diffusion rate determines the rate of reaction. The higher the diffusion coefficient, the higher the reaction rate and shorter the acid penetration length. In contrast, the maximum etched-width was higher at higher diffusion coefficients because of the faster reaction rate. In these simulations, the acid diffusion coefficient was specified at room temperature and updated as the acid was heated inside the fracture.

The reaction between the HCl acid and dolomite formations was also diffusion limited at relatively high temperatures. Hence, the acid diffusion rate determined the acid penetration distance and etched-with profile. However, the diffusion coefficient effect was less dramatic than in the calcite formation case. At lower reservoir temperatures, the reaction rate can reaction limited because of slow dolomite reactivity. Hence, the acid diffusion rate, the faster step in this case, no longer dominates the acid reactivity of the dolomite formations.

Figures 4.3 and 4.4 show that the acid penetration distance was constant at a 10^{-5} to 10^{-6} cm^2/s diffusion coefficient range. This range represents the diffusion coefficients of gelled and emulsified HCl acids. Acid penetration is called fluid loss limited when the acid could reach longer distances but it is limited by the leakoff rate. In this case, acid systems at diffusion coefficients lower than 10^{-5} can reach longer distances than 230 ft, but the acid leakoff rate determined that distance. At higher diffusion coefficients, those representing the range of straight acid, the acid reacts before reaching the fracture tip, 230 ft, representing a reaction limited case (see Figs 4.3-4.4). In reaction limited cases, acid is consumed before reaching the tip of the created fracture.

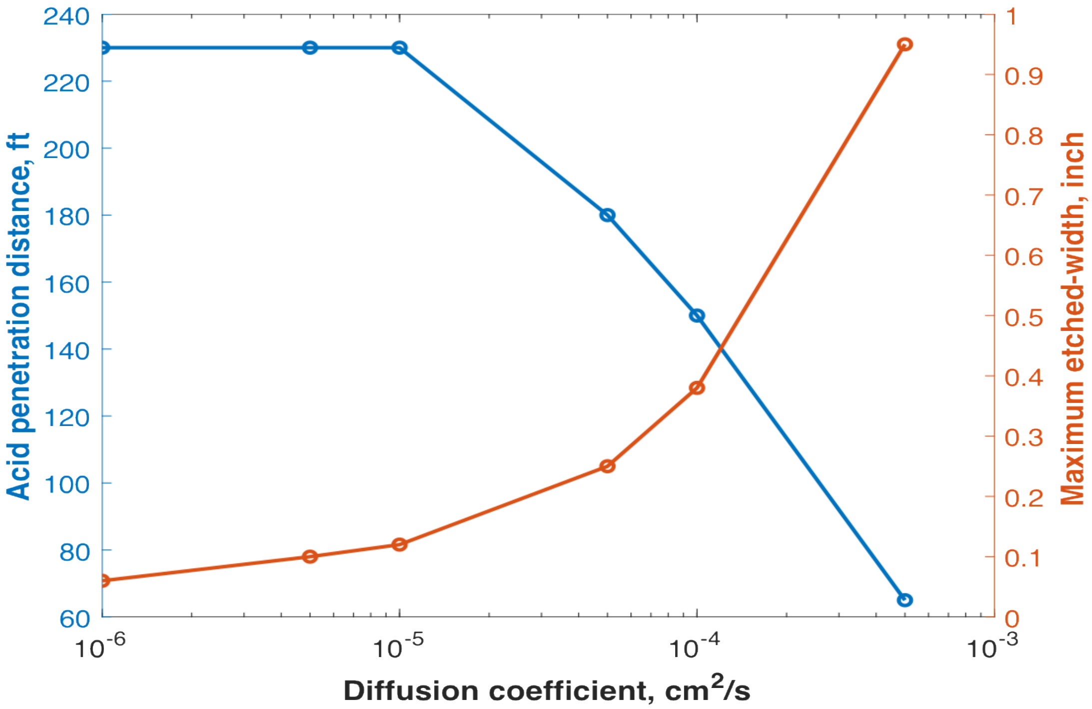

Figure 4.3: Acid diffusion coefficient effects on the acid penetration distance and etched-width distribution of a calcite formation.

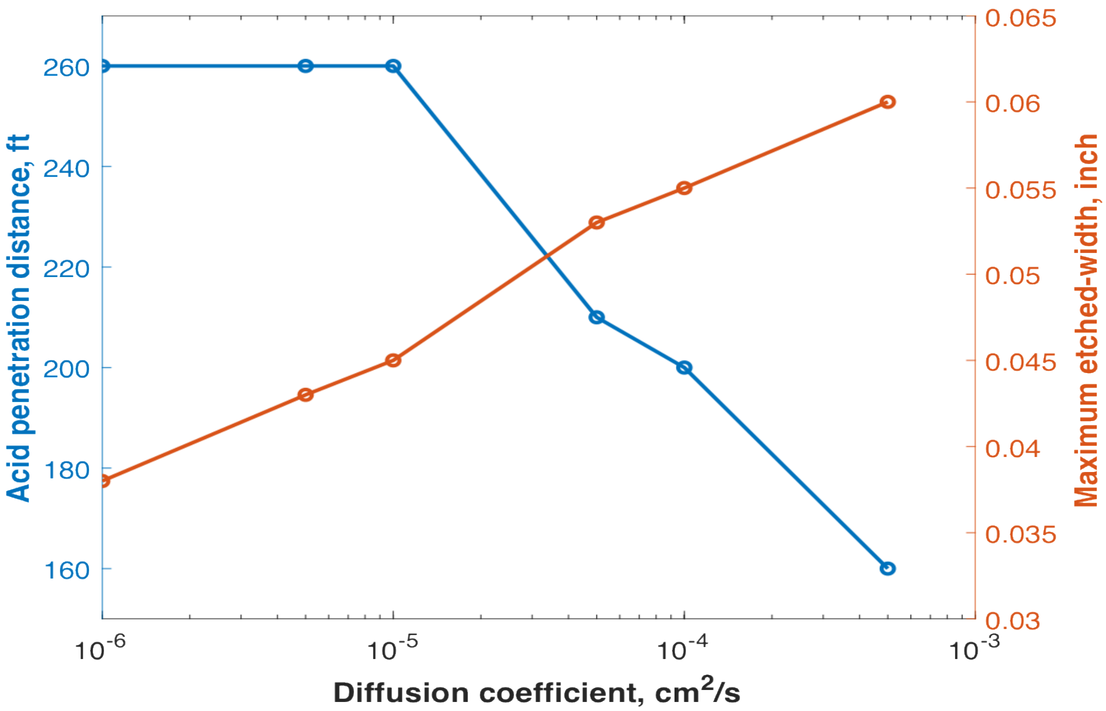

Figure 4.4: Acid diffusion coefficient effects on the acid penetration distance and etched-width distribution of a dolomite formation.

4.3 Leakoff Coefficient

Accurately estimated leakoff coefficient is important for obtaining correct fracture geometry. A low leakoff coefficient means that the fluid loss rate is low, resulting in a larger fracture volume. Different leakoff coefficients were tested assuming reaction rate limited, $D_A = 5\text{x}10^{-4}\ cm^2/s$, and fluid loss limited, $D_A = 10^{-5}\ cm^2/s$, cases. The input data listed in Tables 4.1 and 4.2 were used. As Figure 4.5 shows, in the reaction rate limited case, controlling the leakoff did not increase the acid penetration length, even though the fracture length increased. However, the acid penetration length increased significantly with the leakoff reduction in the fluid loss limited case.

It was assumed in these cases that the diffusion and leakoff coefficients were not related, but in reality, as the fluid viscosity increases, both the leakoff and diffusion coefficients decreases.

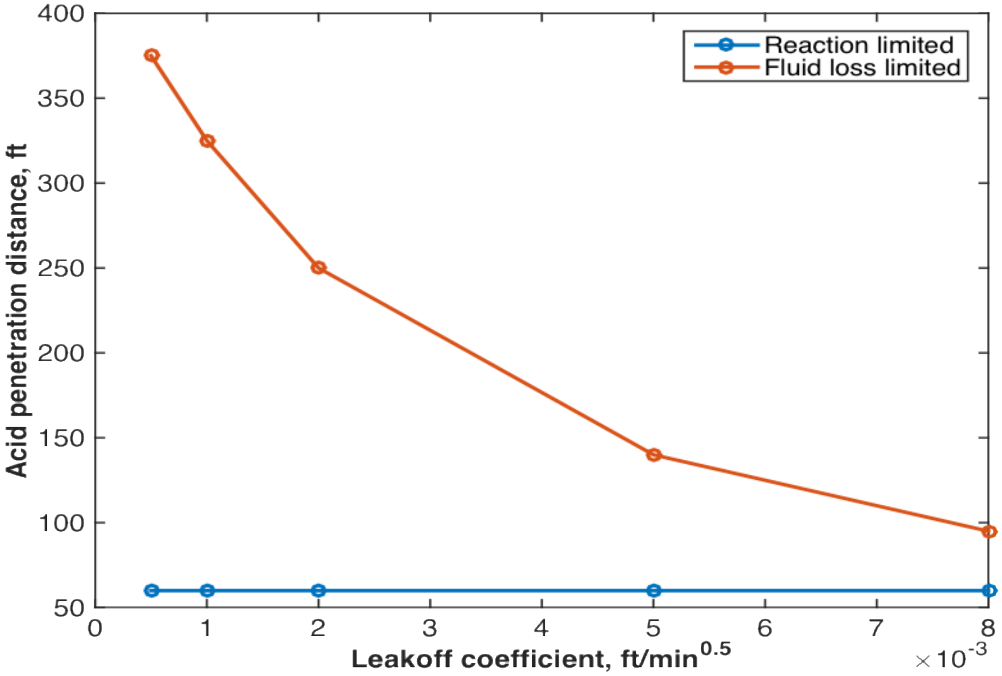

Figure 4.5: Leakoff coefficient effect on the acid penetration distance in the reaction and fluid loss limited cases.

4.4 Injection Rate

The acid injection rate effect was tested assuming a constant treatment volume of 800 bbl and a $5\text{x}10^{-5}$ cm^2/s acid diffusion coefficient. It was assumed that the acid diffusion coefficient was a function of the temperature and viscosity, while the injection rate had a negligible effect. The input data used in this case are listed in Tables 4.1 and 4.2. In general, a higher fluid injection rate results in a more efficient fracture, leading to a larger fracture size for the same fluid volume. Figure 4.6

shows that in this research, the acid penetration distance improved significantly with an increase in the injection rate at a given treatment volume. Injecting acid at higher rates reduced the residence time and increased the fracture width and length, allowing for a longer acid penetration distance. Even though the higher injection rate increased the fracture height, the effect was not significant enough to reduce the acid penetration distance, assuming the pay zone was bounded by stable layers (see Table 4.2). The fracture height created by the different injection rates was between 140 and 170 ft and the pay zone thickness was 120 ft. Most of the acid in this case was spent in the pay zones.

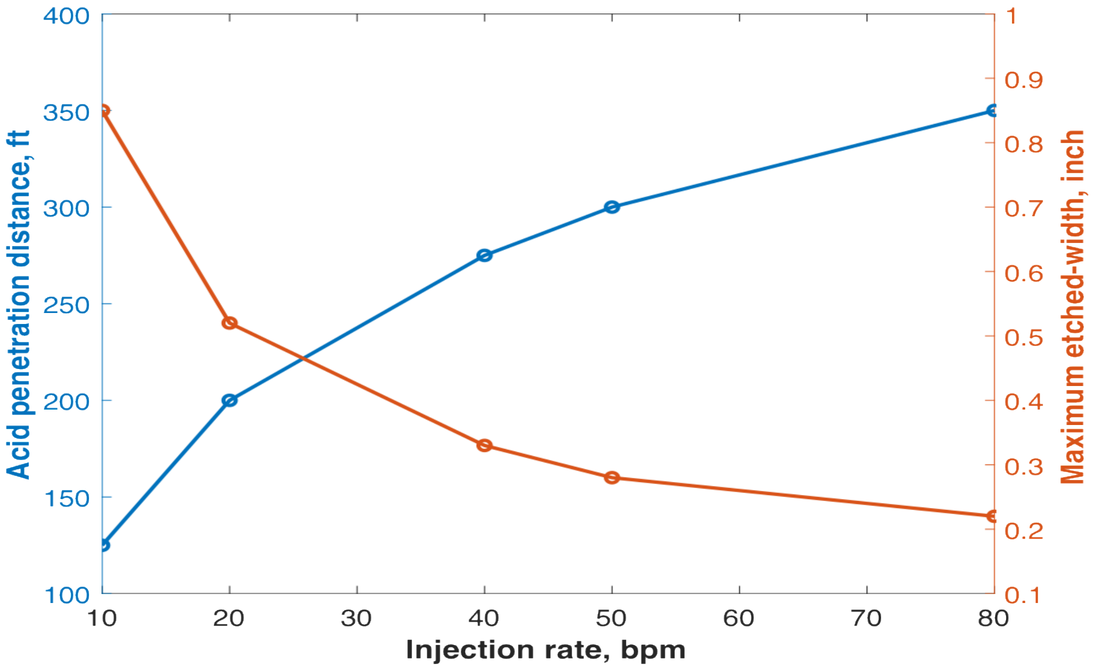

Figure 4.6: Injection rate effect on acid penetration distance and etched-width distribution, assuming a confined fracture.

Another case was investigated where the bounding layer stresses and toughness were reduced, representing a poorly bounded pay zone case. Figure 4.7 shows that the acid penetration length improved as the injection rates moved from low to moderate, and then reduced at higher rates. To understand this behavior, Figure 4.8 illustrates that the fracture height increased significantly at the expense of the fracture length at high injection rates. It also shows that a great volume of acid was lost to the non-reactive bounding layers, creating significantly less etching in the desired zones. The conclusion to be drawn from this result is that the formation rock properties should be studied carefully before deciding on the flow rate at which to inject the acid.

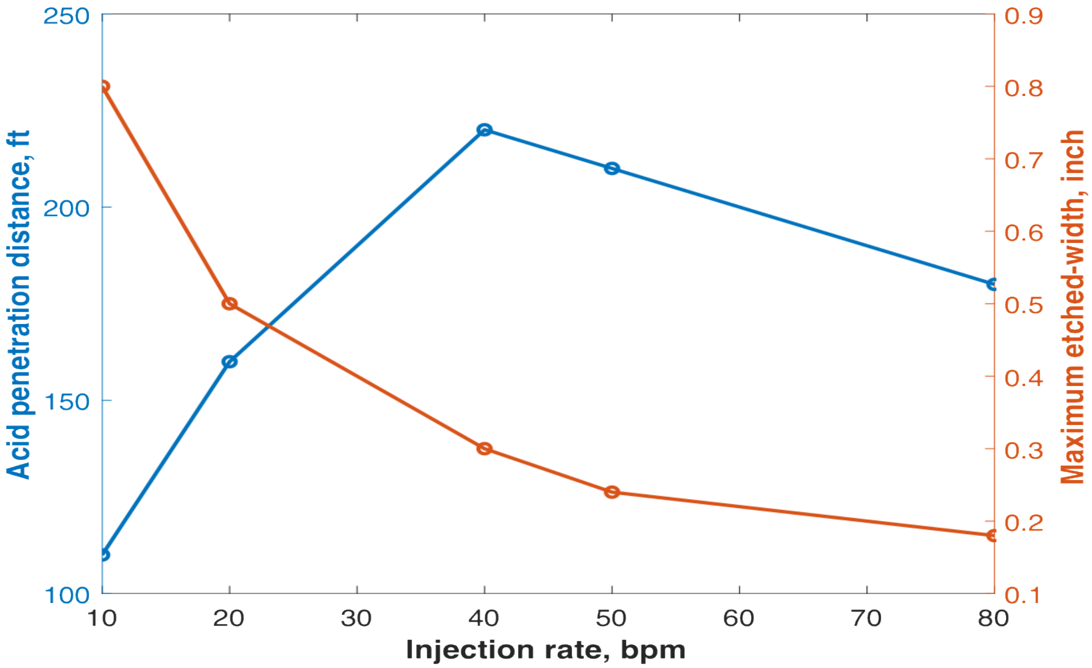

Figure 4.7: Injection rate effect on acid penetration distance and etched-width distribution, assuming a non-confined fracture.

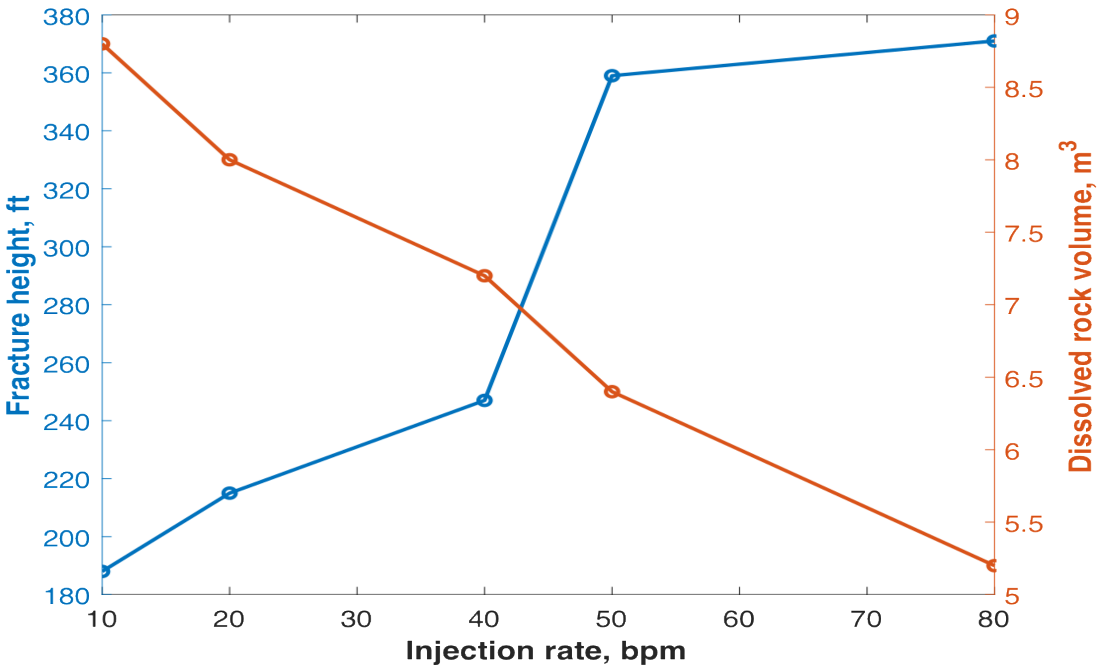

Figure 4.8: Injection rate effect on fracture height and etched-rock volume, assuming a non-confined fracture.

4.5 Acid Viscosity

Acid viscosity is the most complicated design parameter to study because it affects the diffusion and fluid loss coefficients, and thus the fracture geometry. In general, more viscous acid has a lower diffusion coefficient and better control over fluid loss. It also tends to create wider and larger height fractures. For the cases simulated in this section, the acid diffusion and leakoff coefficients were calculated based on a specified acid viscosity (see Table 4.1). As in the injection rate study, two cases were investigated, one assuming a well-bounded pay zone (see Table 4.2) and the other assuming a pay zone that was poorly bounded. For the well-bounded layers case, as the acid viscosity increased, the acid penetration distance increased and the etching profile became more uniform. In this case, increasing the acid viscosity also increased the fracture length and width without resulting in a significant increase in fracture height. It also lowered the acid diffusion coefficient, allowing the acid to travel longer distances. Figure 4.9 shows that the acid viscosity effect was dramatic when increased from 1 to 10 cp, where the acid penetration distance increased significantly. However, there was no obvious advantage to increasing the acid viscosity beyond 20 cp. For the poorly-bounded layers case, there was an improvement in the acid penetration distance until the viscosity reached 20 cp. After that, an increase in acid viscosity inversely affected the acid penetration distance (see Fig. 4.10). To illustrate this behavior, Figure 4.11 shows that the highly viscous acid caused significant growth in the fracture height at the expense of length. It also shows that a great volume of acid was lost to the bounded layers, resulting in a lower volume of etched rock. In practice, the formation layers properties should be studied carefully to decide what acid viscosity should be used.

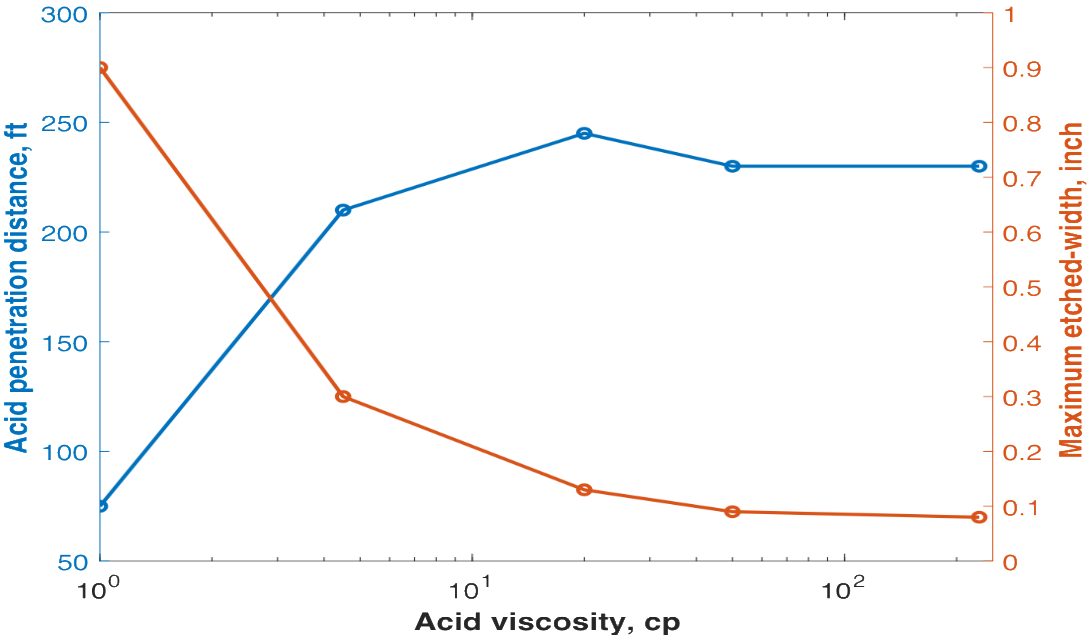

Figure 4.9: Acid viscosity effect on acid penetration distance and etched-width distribution, assuming a confined fracture.

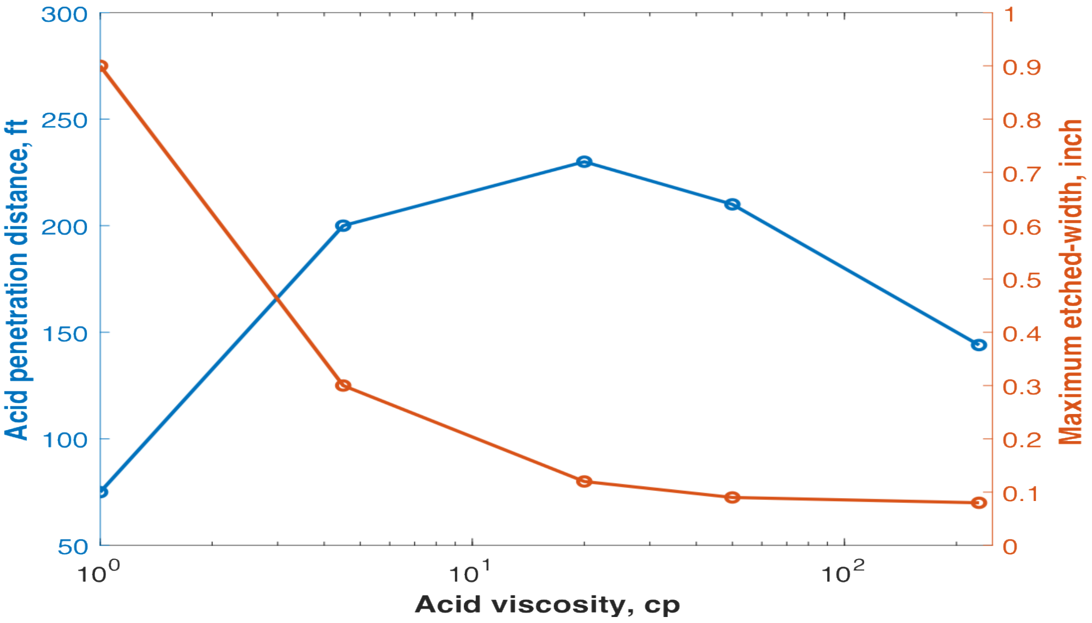

Figure 4.10: Acid viscosity effect on acid penetration distance and etched-width distribution, assuming a non-confined fracture.

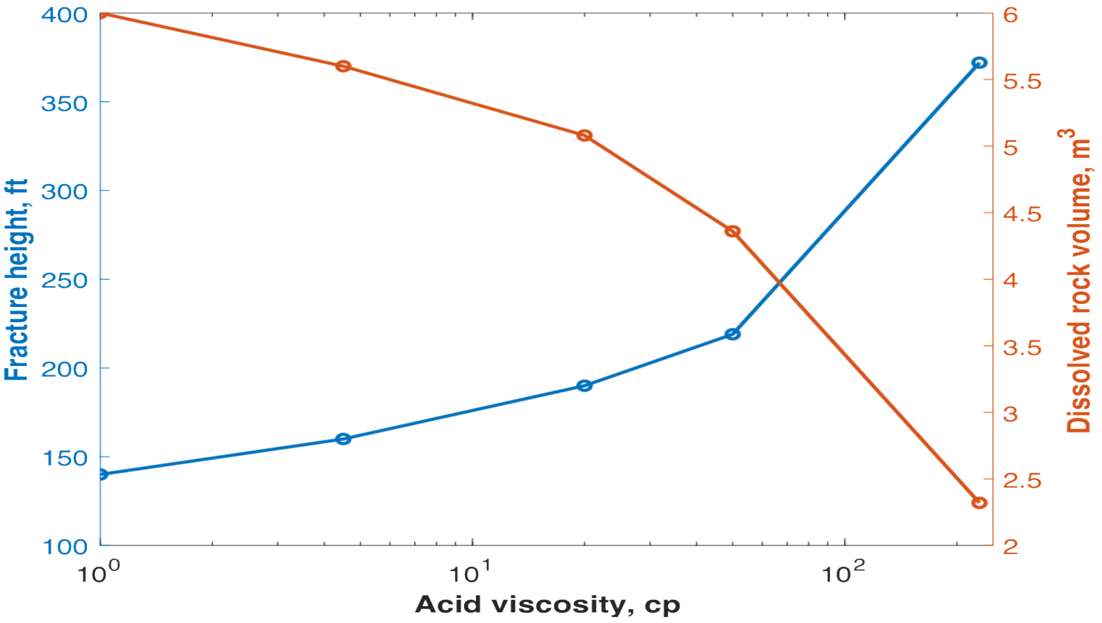

Figure 4.11: Acid viscosity effect on fracture height and etched-rock volume, assuming a non-confined fracture.

4.6 Acid Concentration

In this model, acid concentration represents the percentage of acid mass in a solution. The effect of the acid concentration on the diffusion coefficient was assumed to be negligible as compared to the viscosity and temperature effects. Acid concentrations ranging between 10% to 28% were tested assuming constant treatment volume. The pay zone mineralogy was dolomite and the acid diffusion coefficient in this case was 1x10^{-4} cm^2/s. The input data listed in Tables 4.1 and 4.2 were used in this study. Figure 4.12 indicates that the acid concentration changed the magnitude of the etching profile but did not affect the acid penetration distance. A similar study was done on a calcite formation and the same conclusion was reached.

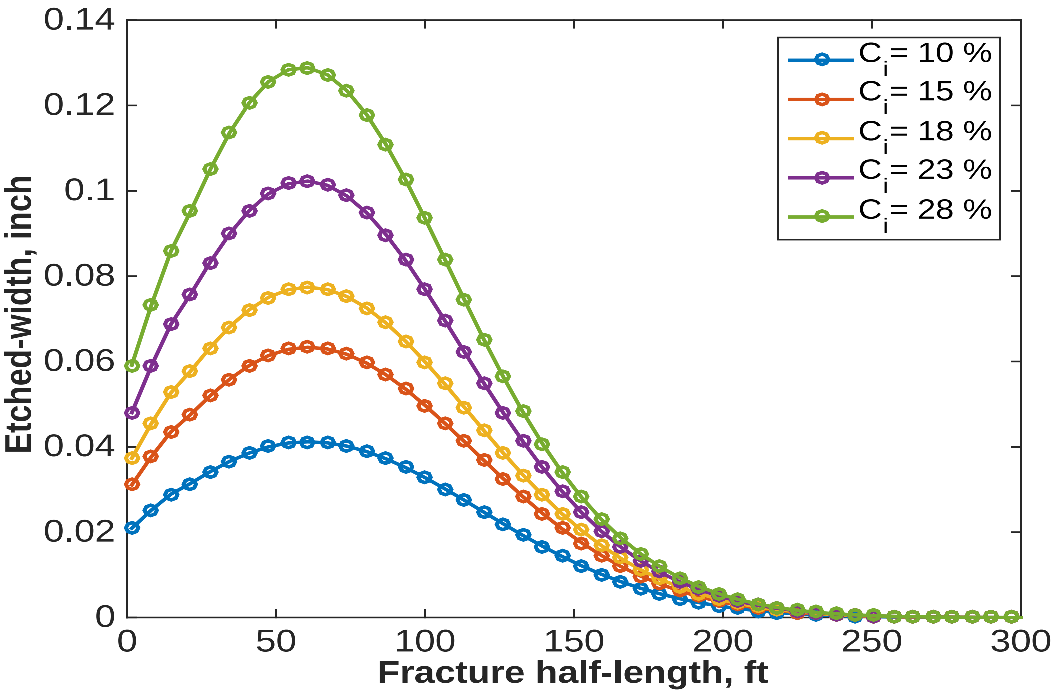

Figure 4.12: Acid concentration effect on acid penetration distance and etched-width distribution in a dolomite formation.

4.7 Acid/Formation Reactivity

The reaction kinetics between acid and a carbonate formation are a function of the acid type. Weak acids such as acetic and formic acids have lower reaction rates with carbonate minerals than does the stronger HCl acid. This model only considered the HCl acid reactions with calcite and dolomite rocks. The acid solution profiles across the fracture dimensions were different for calcite and dolomite formations for the same input data. Assuming a 1×10^{-4} cm^2/s acid diffusion coefficient and using the input data listed in Tables 4.1 and 4.2, the concentration profiles across the fracture width were determined (see Figs 4.13-4.14). Two conclusions could be drawn from the results. First, the acid was able to reach longer distances in the less reactive dolomite formation. Second, the concentration at the fracture wall was zero in the calcite formation and non-zero in the dolomite. The concentration gradient in the calcite formation was substantially steeper, resulting in a greater acid flux towards the fracture surfaces, and hence a greater acid-etched width (see Fig. 4.15).

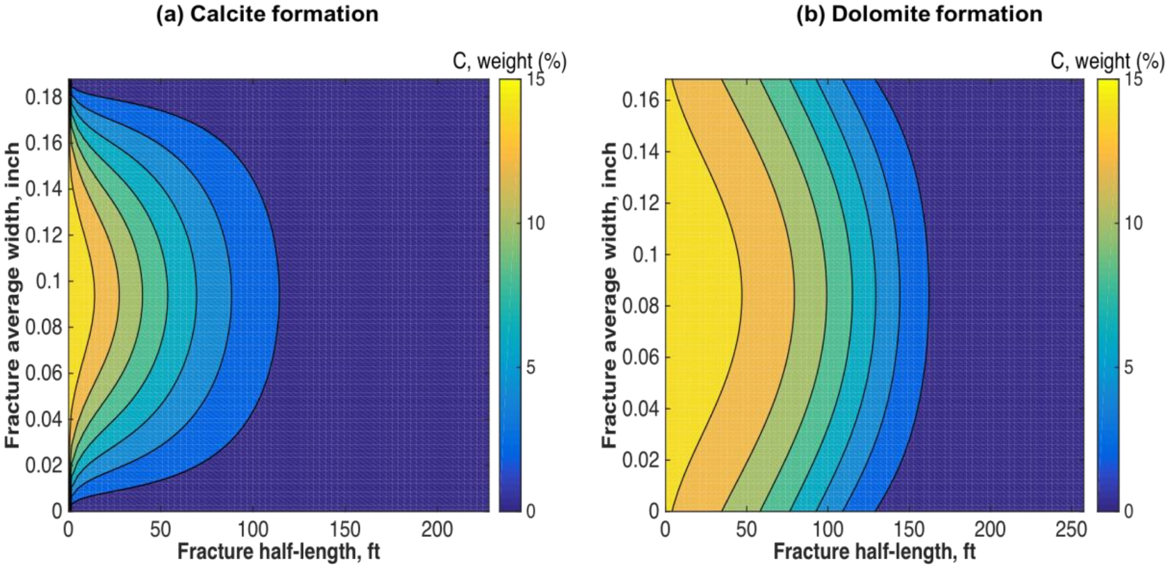

Figure 4.13: Acid concentration profiles across the fracture width.

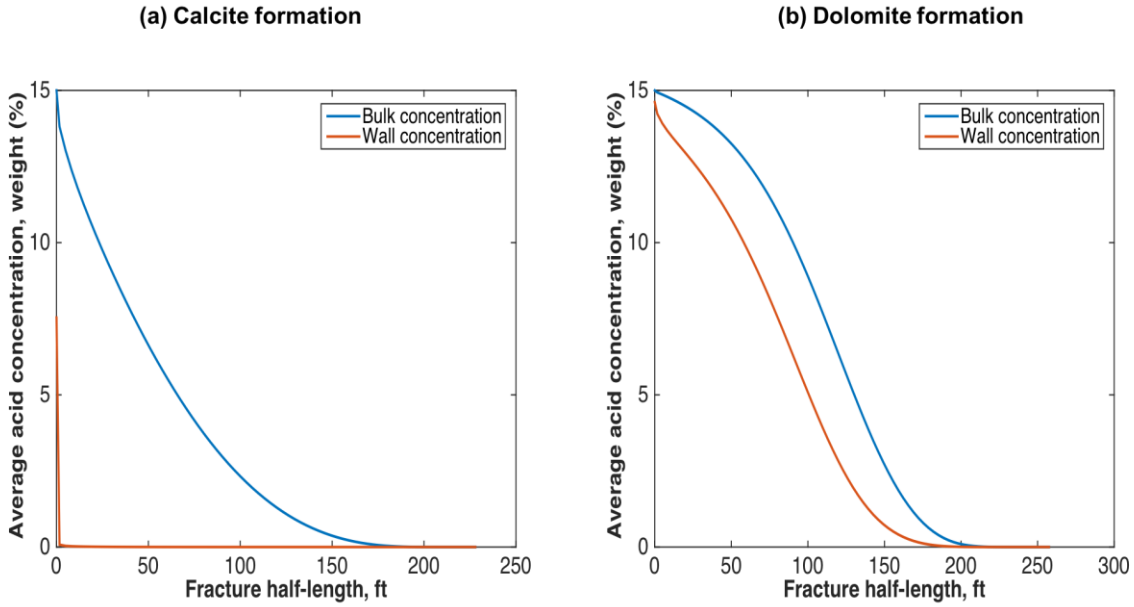

Figure 4.14: 1D bulk and wall acid concentration profiles.

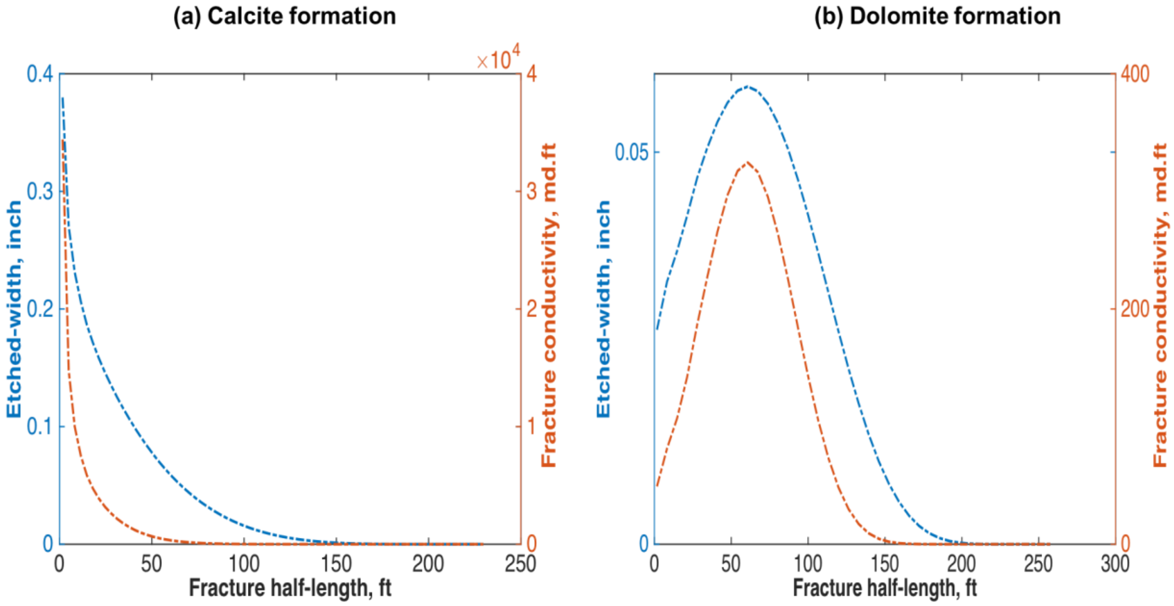

Figure 4.15: 1D etched-width and fracture conductivity profiles.

4.8 Acid Reaction During Fracture Closure

Most acid fracture models assume that the acid completely spent during injection. This is a good assumption for HCl acid reactions with calcite fracture surfaces. Straight acid reacts completely during injection in calcite formations. For retarded HCl acid systems, more than 80% of the acid reacts during injection in calcite formations and the rest reacts during closure. The remaining acid can be assumed to react proportionally along the fracture half-length, as many models have assumed. Proportional reaction assumes that the remaining acid reacts proportionally to the final acid concentration profile. Figure 4.16a shows etched-width profiles at a calcite formation when the acid was simulated during closure, and compares them to a proportional reaction case. The magnitudes do not exactly match, but the differences are small. The simulated case assumed a retarded acid system with a 10^{-5} cm^2/s diffusion coefficient. The magnitude difference between the two cases was zero when straight HCl acid was simulated.

The remaining acid may not react proportionally for the dolomite case. First, a sizeable fraction of the acid did not react at the fracture surfaces, but instead was lost to the formation; to determine the exact fraction, acid fracture had to be simulated during closure. Second, a reasonable fraction of the total injected acid volume reacted during closure as the acid temperature increased. The reaction rate between the acid and dolomite formation is very sensitive to the temperature profile. The simulated case showed that 72% of the acid injected reacted at the fracture surfaces, while the remaining was lost to the formation. Around 30% of the acid reacting at the fracture surfaces (72% of total injection) was consumed during the closure. These fractions changed significantly at different reservoir temperatures and acid diffusion coefficients. For instance, straight acid will be mostly reacted during injection in the dolomite formation. Figure 4.16b shows a significant difference in the etched-width magnitude between the simulated acid during fracture closure and the assumption of a proportional reaction. This proves that obtaining an accurate solution should involve acid simulation during fracture closure.

The simulated dolomite case showed that the fracture took approximately 10 minutes to close and almost the same amount of time for the acid to completely react. The acid may react completely before closure or the fracture may close before the acid is consumed, depending on the acid's reactivity and leakoff rate. Figure 4.17 includes the acid concentration profiles along the fracture width and length at different closure times. At each time step the fracture width decreased, as did the acid concentration. The final fracture width represents the average etched-width, assuming the fracture hydraulic width was zero at closure (see Fig. 4.17c). Figure 4.17d illustrates the 1D acid concentration profiles at different fracture closure times.

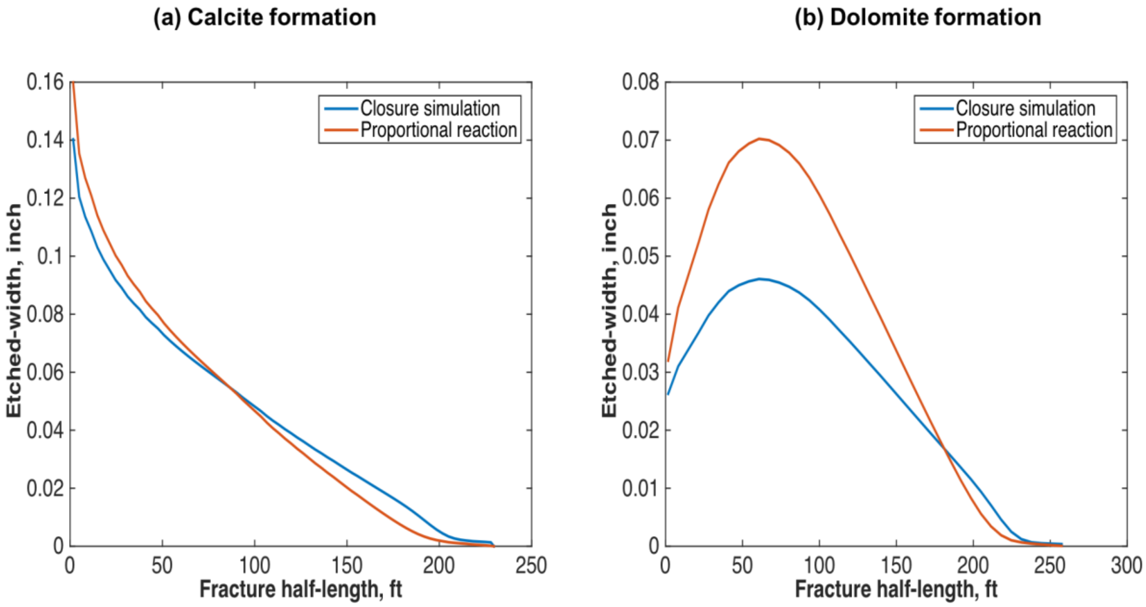

Figure 4.16: Acid etched-width profiles assuming a proportional reaction and simulating the remaining acid during closure.

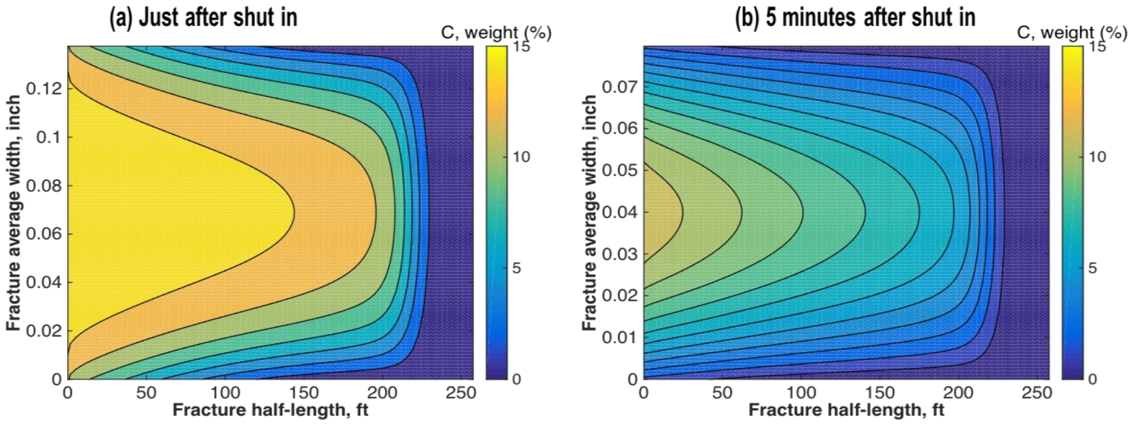

(a) Just after shut in

(b) 5 minutes after shut in

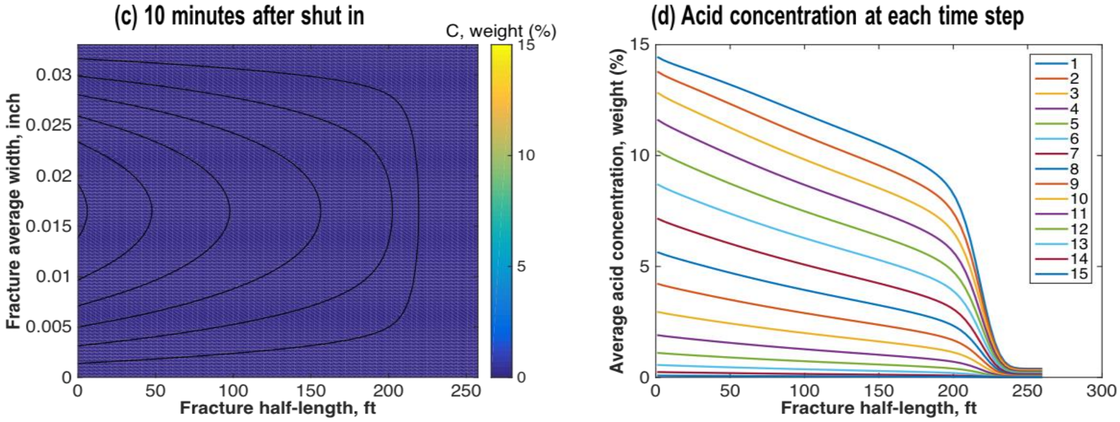

(c) 10 minutes after shut in

(d) Acid concentration at each time step

Figure 4.17: 1D and 2D acid concentration profiles during fracture closure at different time steps.

4.9 Fracture Propagation Coupling

To reduce simulation time, many models assume a constant fracture geometry calculated based on the injected fluid volume at the end of the treatment. One objective of the developed model was to test this assumption and compare it with the acid solution when coupled with fracture geometry propagation. Two cases were investigated, one with a high diffusion coefficient representing straight acid, $D_A = 5\text{x}10^{-4} cm^2/s$, and the other with a low diffusion coefficient representing a retarded acid system, $D_A = 10^{-5} cm^2/s$; both cases assumed a leakoff coefficient of 1x10^{-3}

ft/min$^{0.5}$. These cases were run assuming that the pay zone was made of calcite minerology. The first case was reaction limited and the second was fluid loss limited.

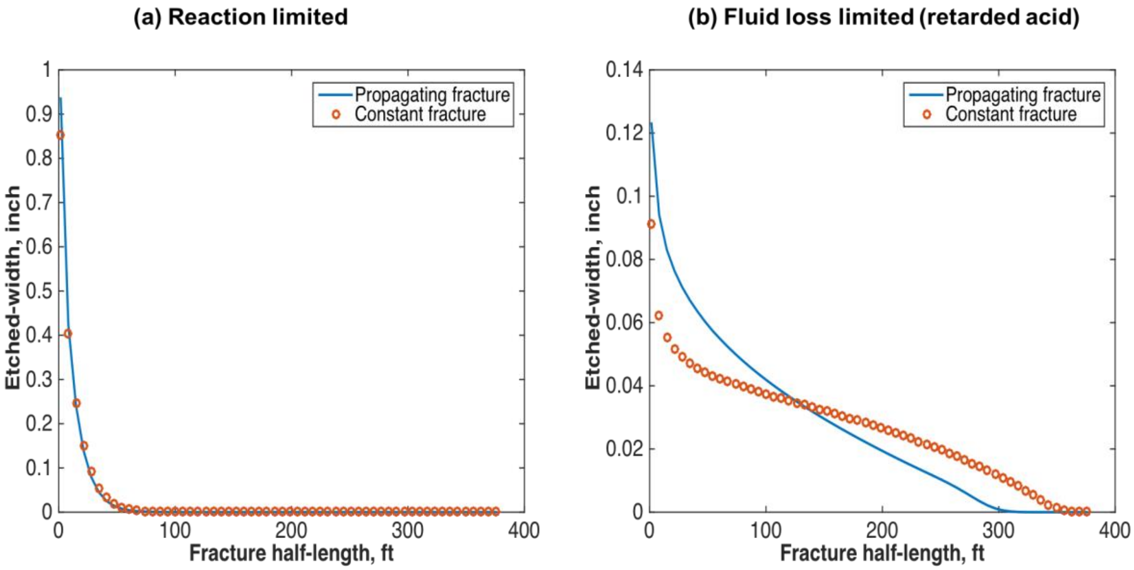

Figure 4.18: Comparison of etched-width profiles for the constant and propagating fracture assumptions, assuming a calcite formation.

Figure 4.18a shows no difference in the acid penetration distance and etched-width profile for the first case, while Figure 4.18b indicates a significant difference in the second case. For the first case, as the fracture propagated in the formation, the acid penetration distance did not increase because it was limited by the reaction rate. Hence, using a constant fracture geometry produced the same result as when the fracture propagation was coupled with the acid model. For the second case, the fracture propagation limited the acid penetration length at each time step. Figure 4.19 explains how the constant fracture assumption allowed for the acid to reach a longer distance than the length of the fracture at that time step. For instance, the second time step shows that the acid reached 150 ft inside the fracture for the constant fracture assumption (see Fig. 4.19a), but only 80 ft for the propagating fracture case (see Fig. 4.19b). Hence, assuming a constant fracture geometry will always result in overestimation of the length of acid penetration. In conclusion, coupling the fracture propagation shows a significant difference in the acid solutions (as compared to assuming a constant fracture geometry) when the process is described as fluid loss limited (see Fig. 4.18b).

One important conclusion is that a uniform etched-width distribution along the fracture length of a retarded HCl acid system cannot be achieved. For extremely retarded acid systems, a constant drop in the etched-width value, until zero is reached at the fracture tip, is theoretically obtainable (see Fig. 4.20). For moderately retarded systems, the etching profile was shown to decline towards the fracture end (see Fig. 4.18b). This is in contrast to the conventional non-coupled approach from which the uniform etching profile was obtained at moderate to high Peclet numbers.

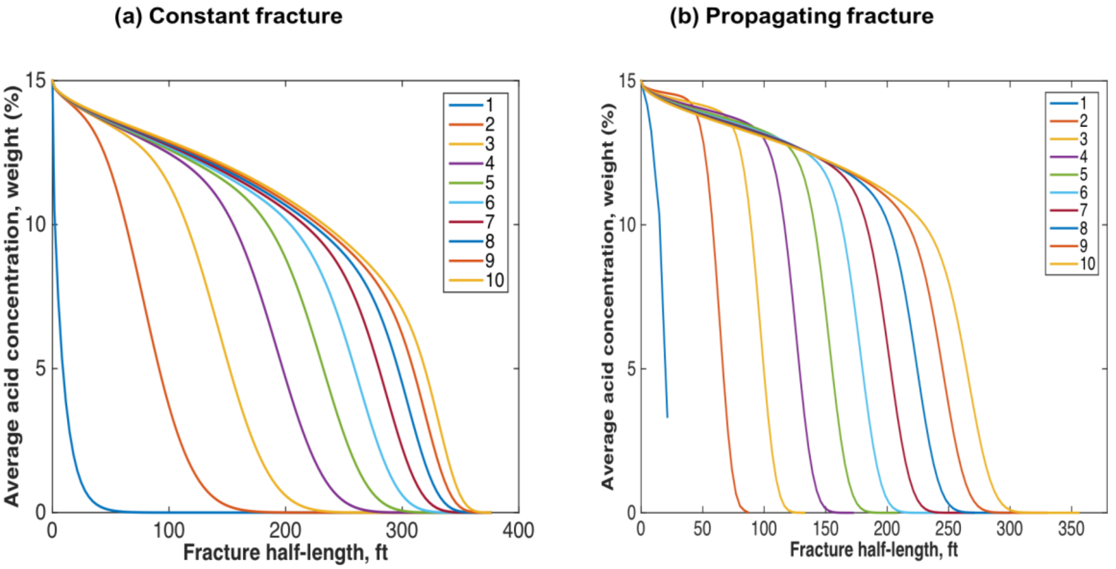

Figure 4.19: Comparison of acid concentrations for constant and propagating fracture assumptions at different time steps, assuming a calcite formation.

Similar cases were tested with dolomite formation. For the reaction limited case, a good match in the acid penetration distance between the coupled and non-coupled assumptions was observed, except for an offset in the etching magnitude (see Fig. 4.21a). However, the fluid loss limited case showed no matches in etching profile or acid penetration distance (see Fig. 4.21b). In general, a more accurate acid solution would require fracture propagation coupling at each time step.

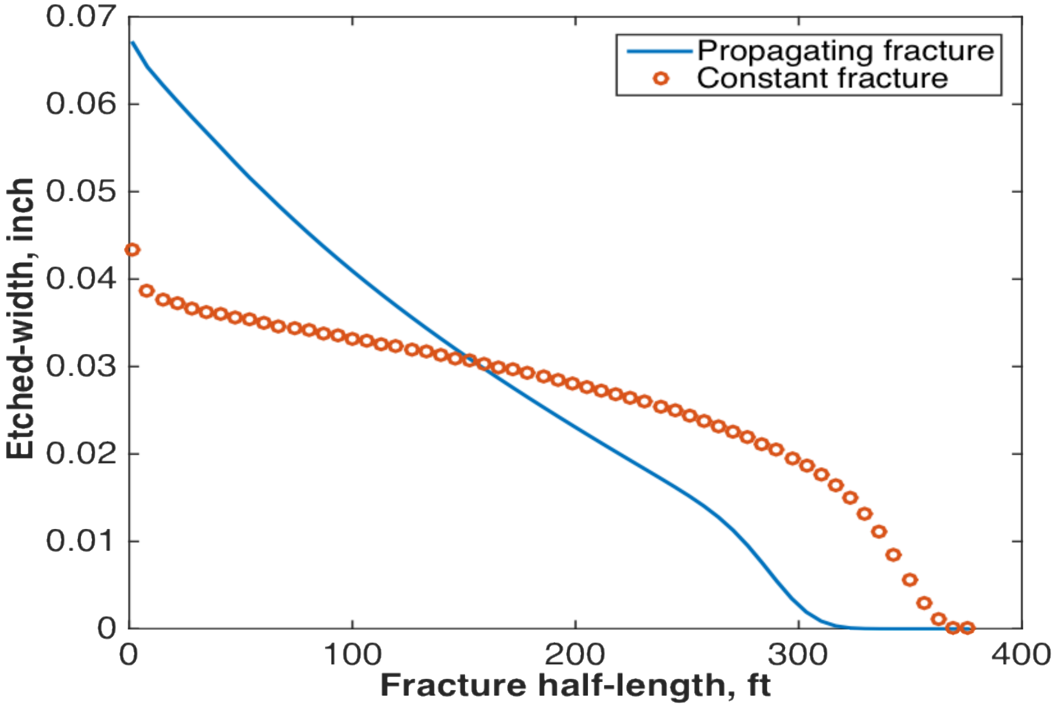

Figure 4.20: Comparison of etched-width profiles for constant and propagating fracture assumptions, assuming a calcite formation and extremely retarded acid system.

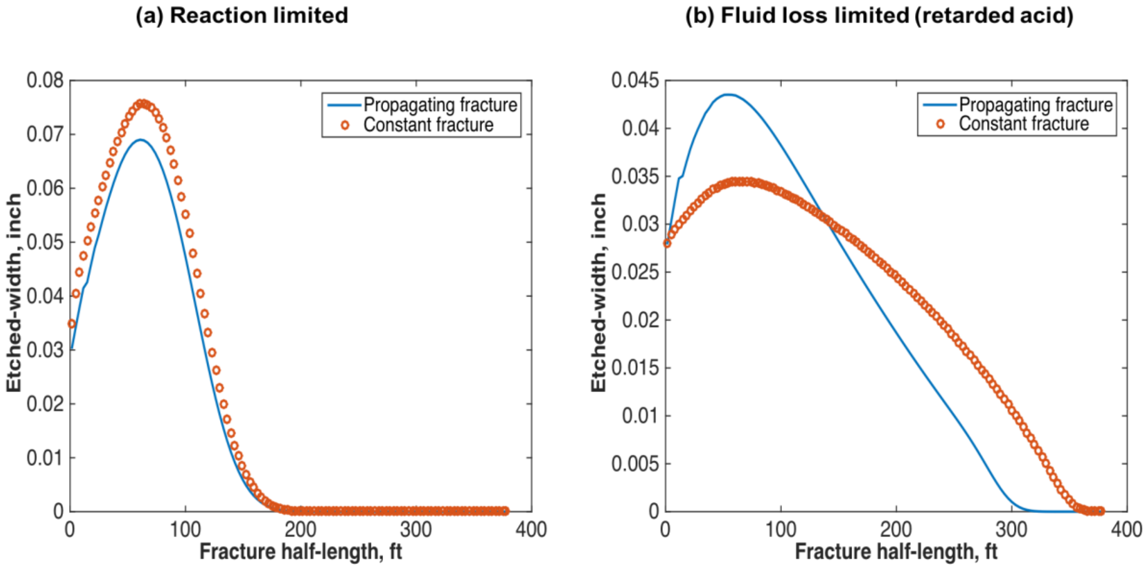

Figure 4.21: Comparison of etched-width profiles for constant and propagating fracture assumptions, assuming a dolomite formation.

4.10 Temperature Effects

Temperature impacts the acid solution, since both the acid diffusion coefficient and reaction rate constant are strong functions of temperature. However, the impact is different in calcite and dolomite formations. The temperature effects on the acid penetration distance and etching profile are described in this section. Some of the acid fracture models assumed an average fracture temperature instead of solving for the temperature distribution in order to save on simulation time. The effect of this assumption on the acid solution will be discussed below. Also, the significance of the heat of reaction on the temperature distribution, and hence on the acid solution, will be quantified. The input data listed in Tables 4.1 and 4.2 were used for this section.

4.10.1 Temperature Coupling versus Average Temperature

Two cases were investigated for this section of the research. The first solved for the temperature distribution assuming an 80.6 ^{o}F injected fluid temperature and 302 ^{o}F reservoir temperature, while the second case assumed a 191.3 °F constant average temperature. The acid diffusion coefficient was 5×10^{-5} cm^2/s and the leakoff coefficient was 10^{-3} $ft/min^{0.5}$. The two cases were first tested assuming calcite minerology for the pay zones. Figure 4.22a shows the temperature distribution along the fracture width and length at the final treatment time. Figure 4.22b illustrates a comparison of the two assumptions in terms of the etching profile. The temperature change in the calcite formation affected the diffusion coefficient but had a negligible effect on the reaction rate, because the reaction was considered infinite even at room temperature. The offset in the etching profiles between the two assumptions was due to the temperature's effect on the diffusion coefficient. The assumption of an average constant temperature in the calcite formations did not seem to be improper.

Figure 4.23a shows the temperature distribution in a dolomite formation at the final injection time step. Figure 4.23b indicates a match between the etching profiles for the two assumptions. Temperature changes in the dolomite formation had a significant impact on the diffusion coefficient and reaction rate constant. The maximum etching in the dolomite formations usually occurred away from the fracture entrance. This phenomenon occurred because the acid was heated while traveling inside the fracture. The reactivity of the acid increased significantly, and hence affected the etching magnitude. The etching profile then dropped from the maximum, because the acid concentration decreased in spite of the increase in acid temperature. This behavior could not be captured, assuming an average single temperature. To obtain an accurate acid solution in a dolomite formation, the temperature profile should be coupled with the acid model.

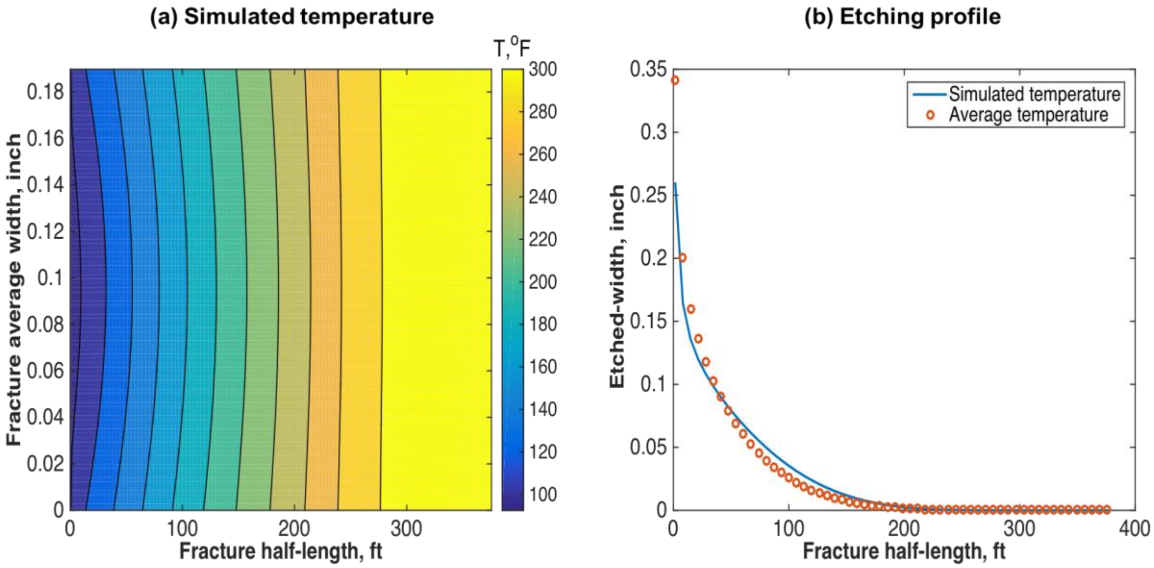

Figure 4.22: Fracture temperature solution and comparison of the etching profiles for assumptions of average and simulated temperatures in a calcite formation.

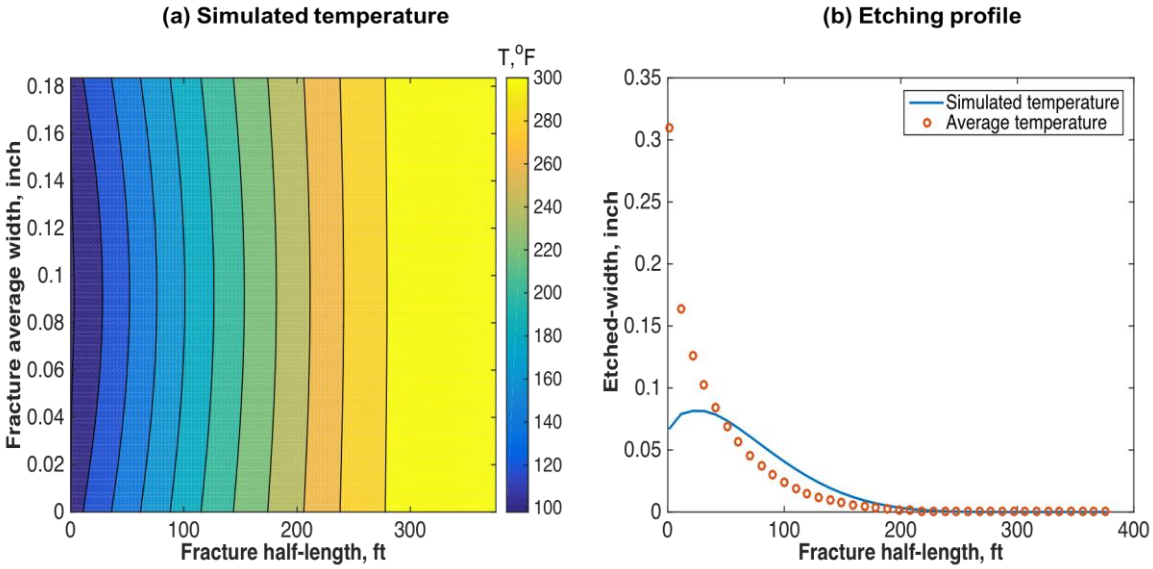

Figure 4.23: Fracture temperature solution and comparison of etching profiles for assumptions of average and simulated temperatures in a dolomite formation.

4.10.2 Reservoir Temperature Effects on Fracture Surface Etching Distribution

In this section, the reservoir temperature was altered while the injected acid temperature was held constant at 80.6 ^{o}F, in order to observe changes in the etching distribution profiles for calcite and dolomite formations. The acid diffusion coefficient was 5x10^{-5} cm^{2}/s and the leakoff coefficient was 1x10^{-3} ft/min$^{0.5}$. Figure 4.24a shows the etching profile and Figure 4.24b indicates the total volume of dissolved rock at the fracture surface at different reservoir temperatures in the calcite formation. The conclusion was that the reservoir temperature had a negligible effect on the etching profile of the calcite formation.

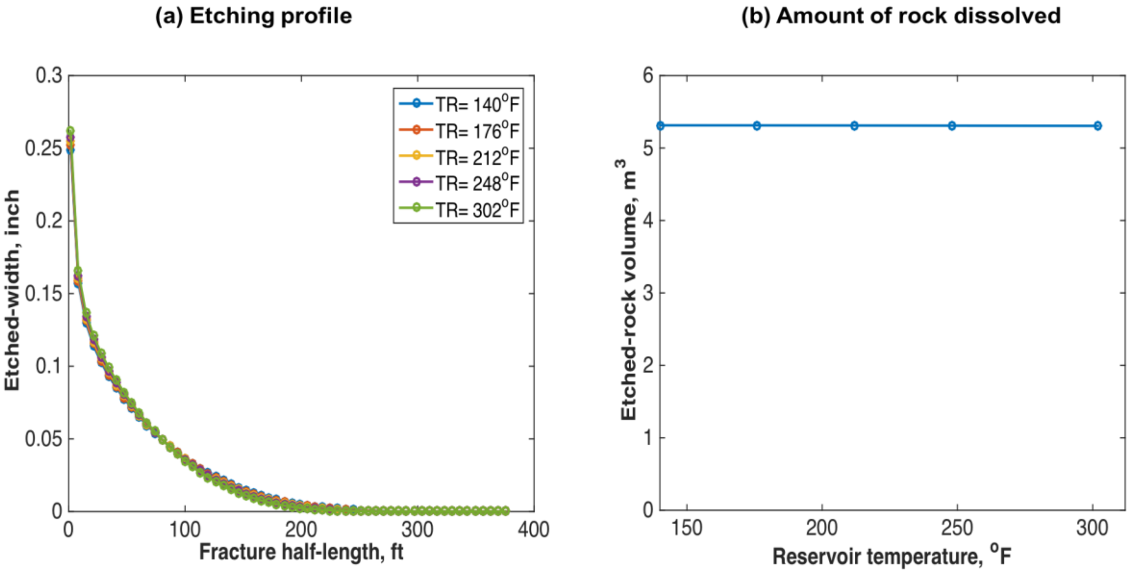
(a) Etching profile

(b) Amount of rock dissolved

Figure 4.24: Etching profile and amount of rock dissolved at different reservoir temperatures, assuming calcite mineralogy.

The reservoir temperature effect on the dolomite formation is shown in Figure 4.25. As the reservoir temperature increased, the acid penetration distance decreased and the etching magnitude increased (see Fig. 4.25a). The maximum etching location was closer to the fracture entrance at higher reservoir temperatures. Also, the amount of rock dissolved was a function of the reservoir temperature. Larger amounts of rock were dissolved at higher temperatures, leaving less acid to create wormholes (see Fig 4.25b). This signifies the importance of temperature coupling in dolomite formations.

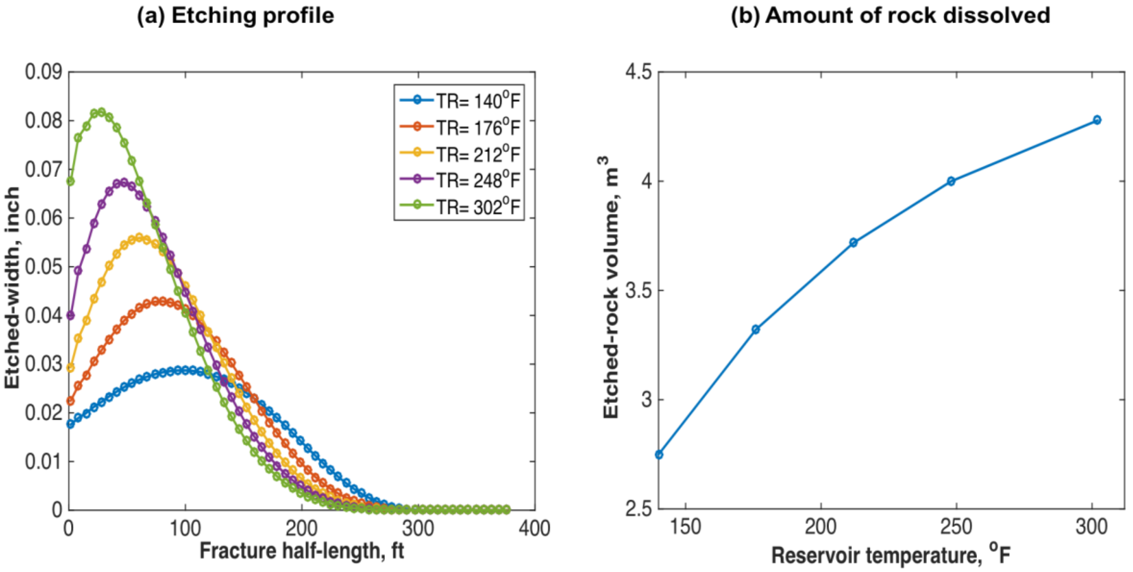

Figure 4.25: Etching profile and amount of rock dissolved at different reservoir temperatures, assuming dolomite mineralogy.

4.10.3 Heat of Reaction Effects

Heat is generated from the exothermic HCl acid reacting with the carbonate formations. The heat of reaction affects the temperature distribution of the acid injected inside the fracture. The effect of an increase in the temperature profile from the heat of reaction on the etching profile is described in this section. The acid diffusion coefficient was 5x10^{-5} cm^2/s and the leakoff coefficient was

10^{-3} ft/min$^{0.5}$. Figure 4.26 shows the temperature distribution and difference between the heat of reaction and no heat of reaction assumptions. The temperature difference went up to 12 ^{o}F around the middle of the fracture in the calcite formation case (see Fig. 4.26b). Figure 4.27 shows the results for the dolomite formation case where the maximum temperature difference went up to 13 ^{o}F. The difference in magnitude was a function of the heat of reaction value, reaction kinetics, acid concentration, and reservoir temperature. Guo et al. (2014) reported that the temperature increase attributable to heat of reaction will not exceed 15 ^{o}C (27 ^{o}F). The location of the maximum temperature difference was a function of the acid diffusion coefficient. Higher acid diffusion coefficients resulted in near fracture entrance maximum temperature difference.

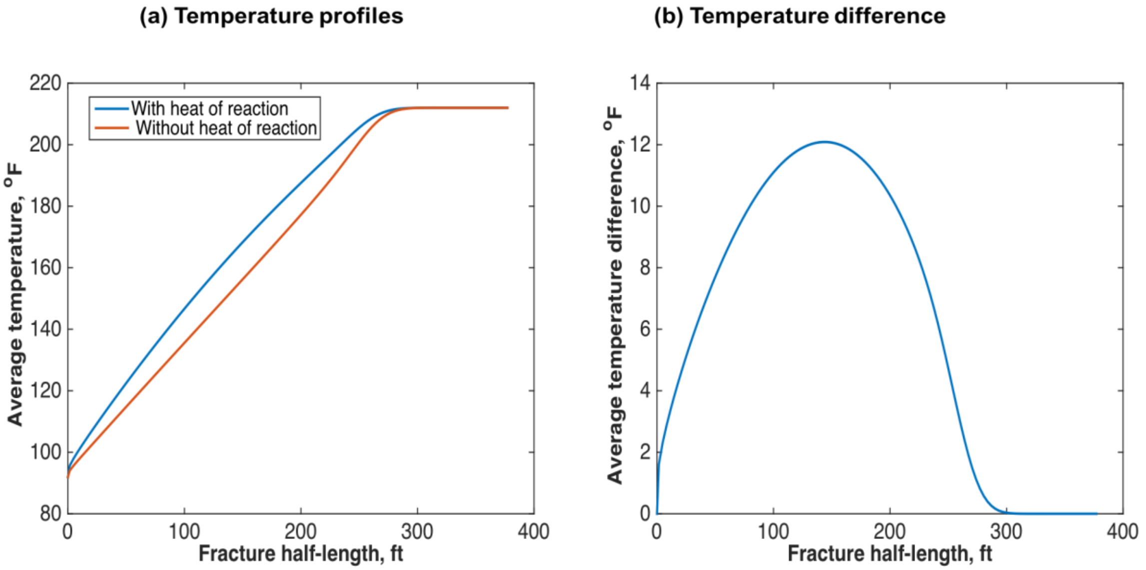

Figure 4.26: Differences in temperature profiles caused by the heat of reaction in a calcite formation.

Figure 4.28 shows the effect of the heat of reaction on the etching profile. As expected, the effect on the calcite formation was negligible (see Fig. 4.28a). However, there was a noticeable effect on the etching magnitude in the dolomite formation case (see Fig 4.28 b). Thus, it can be concluded that it is good practice to include the heat of reaction when simulating acid reactions in dolomite formations.

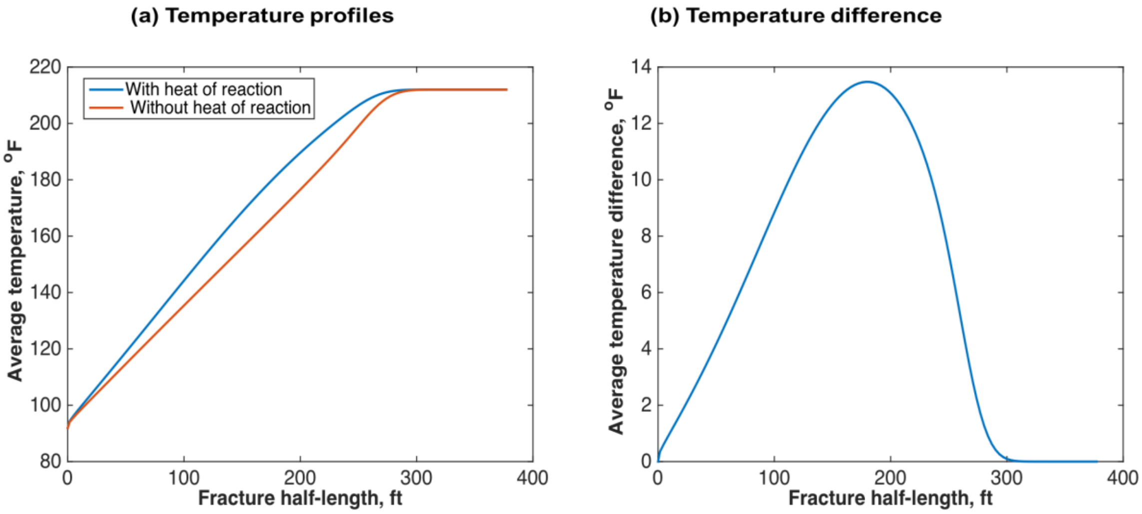

Figure 4.27: Differences in temperature profiles caused by the heat of reaction in a dolomite formation.

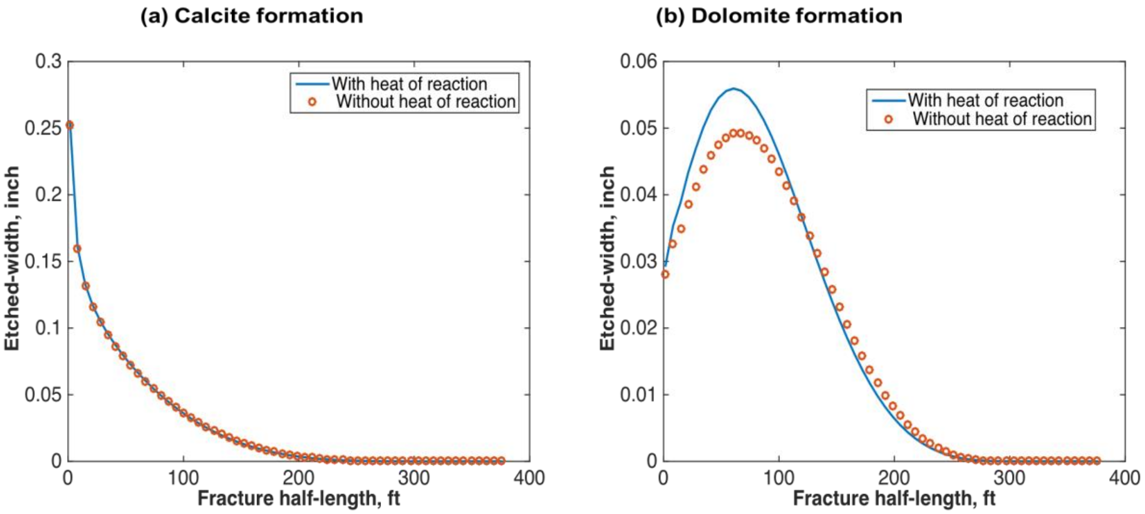

Figure 4.28: Differences in etching profiles caused by the heat of reaction.

4.11 Effect of Pad Fluid

Viscous pad fluid was injected as the first stage to create the fracture, before the second stage of acid injection. The pad fluid was believed to enhance acid penetration through leakoff control, formation cooling, and by creating a wider fracture. The simplified assumption in this model was that the viscous fingering of acid through the pad fluid attributable to a contrast in viscosity was negligible. The pad fluid input data are shown in Table 4.3. The acid, reservoir, and formation properties are shown in Tables 4.1 and 4.2. The acid diffusion coefficient was 10^{-5} cm^2/s and the pad and acid leakoff coefficients were calculated in the model. A high reservoir temperature, $T_R = 302\ °F$, was assumed to study the pad fluid cooling effect.

Table 4.3: Input Data for the First Stage Pad Fluid

Pad Properties		
Input Data	**SI Unit**	**Field Unit**
Density, ρ	1000 Kg/m^3	62.4 lb$_m$/ft^3
Injection rate, q_i	.08 m^3/s	30 bpm
Treatment time, t_e	600 s	10 min
Power law exponent, n	0.9	
Consistency index, K	0.005 lb$_f$.s^n/ft^2	
Spurt loss, S_p	0 m	0 gal/ft^2
Fluid loss multiplier outside pay zone, f_m	0.25	
Opening time distribution factor, κ	1.5	
Pad heat capacity, c_p	4.13 KJ/(Kg.^{o}C)	0.964 Btu/(lbm.^{o}F)
Pad thermal conductivity, k	6x10^{-4} KJ/(s.m. ^{o}C)	0.347 Btu/(hr.ft. ^{o}F)
Pad temperature at surface, T_s	27 ^{o}C	80.6 ^{o}F

Two cases were studied, one assuming the acid was injected in the first stage and the other assuming the acid was injected in the second stage, after pad fluid injection. For both cases, the acid treatment volume and design parameters are the same. Figure 4.29a shows that the pad fluid did two things; first, a more uniform etching profile was obtained. Second, the acid penetration distance was greatly enhanced. It improved from 220 ft to approximately 300 ft because of the injection of the pad fluid. The more uniform etching was obtained because a wider fracture was created. Also, the acid penetration was not restricted by geometry propagation since the pad fluid had already created the fracture. This means that an acid system can create a more uniform etching if pad fluid is injected as the first stage. This more uniform etching is not theoretically possible, as discussed in Section 4.8, without pad fluid creating the fracture. The improvement in acid penetration can be explained by the pad fluid creating a longer and wider fracture.

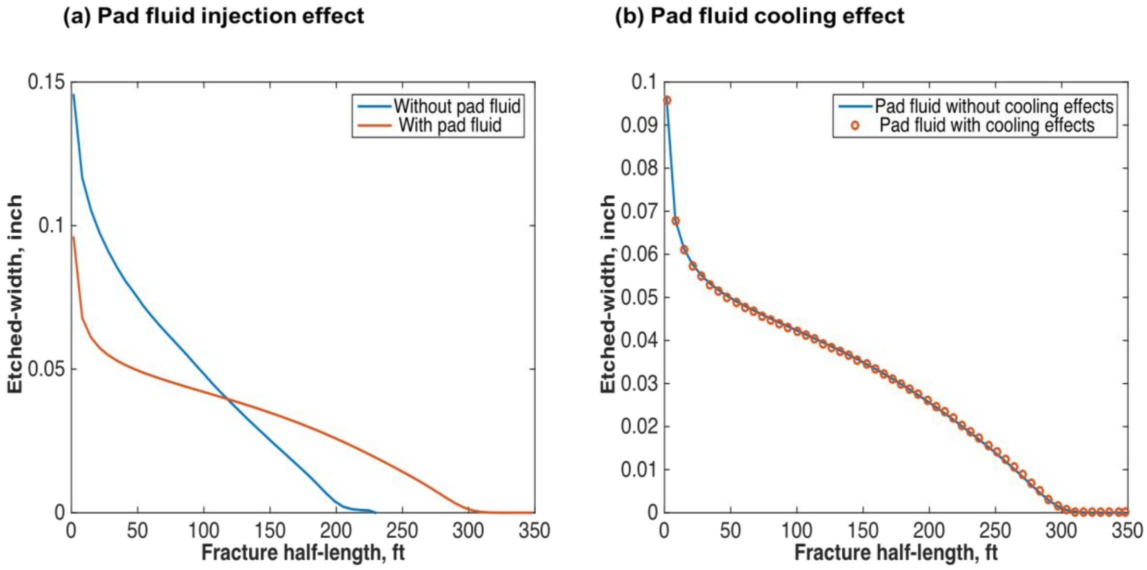

Figure 4.29: First stage pad fluid effects on the etched width profile of a calcite formation.

Pad fluid also tends to cool down the formation around a fracture. To understand this effect, two cases were investigated; the first assumed that the pad fluid cooled down the formation and the second assumed a constant reservoir temperature during pad fluid injection. Figure 4.29b indicates that the pad fluid's cooling effect in the calcite formation had no impact on the etching profile or acid penetration distance.

The same study was done with the assumption that the pay zones were made of dolomite. Similarly, the pad fluid contributed to a longer acid penetration distance and more uniform etching profile (see Fig. 4.30a). However, the pad fluid's cooling effect does not explain the change in etching profile (see Fig. 4.30b). To understand why this cooling did not impact the acid solution in the temperature-sensitive dolomite formation, the bulk temperature profiles were investigated. Figure 4.31a shows the transient acid temperature profiles during acid injection, assuming that the pad fluid did not cool the formation, while Figure 4.31b considers the cooling effect. Looking at the first 50 ft of the fracture length (see Fig 4.30), the pad's cooling affected only the early temperature profiles. After the fourth temperature profile, the difference between the two cases was negligible. Figure 4.32 shows the volume of etched rock at different acid injection times for the two cases. Only a small amount of rock was etched early on, when the temperature difference was significant. Most of the reaction occurred later when the temperature difference between the two cases was not significant.

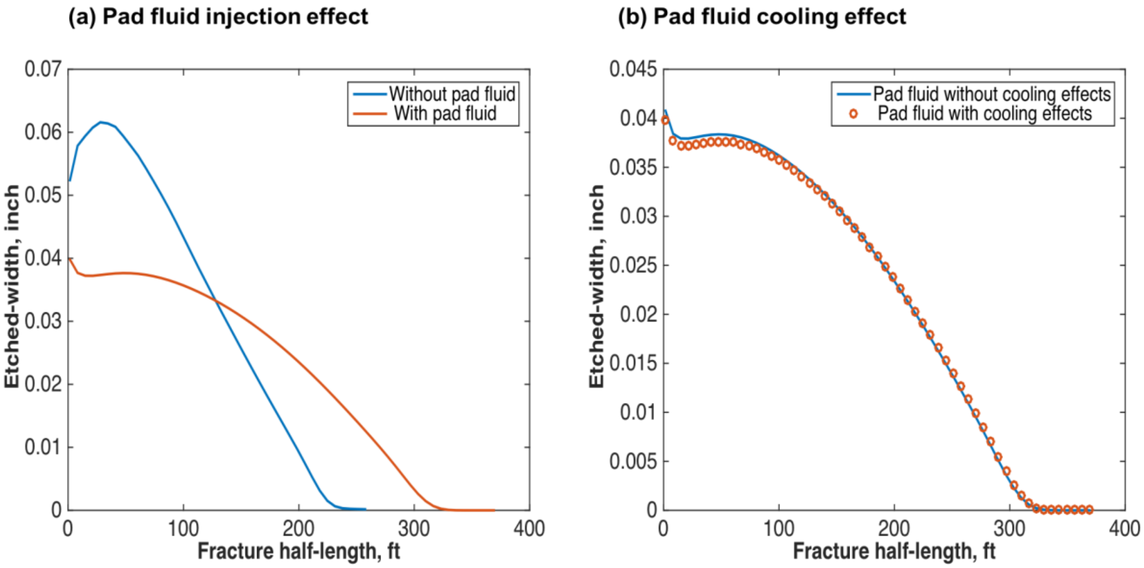

Figure 4.30: First stage pad fluid effects on the etched width profile of a dolomite formation.

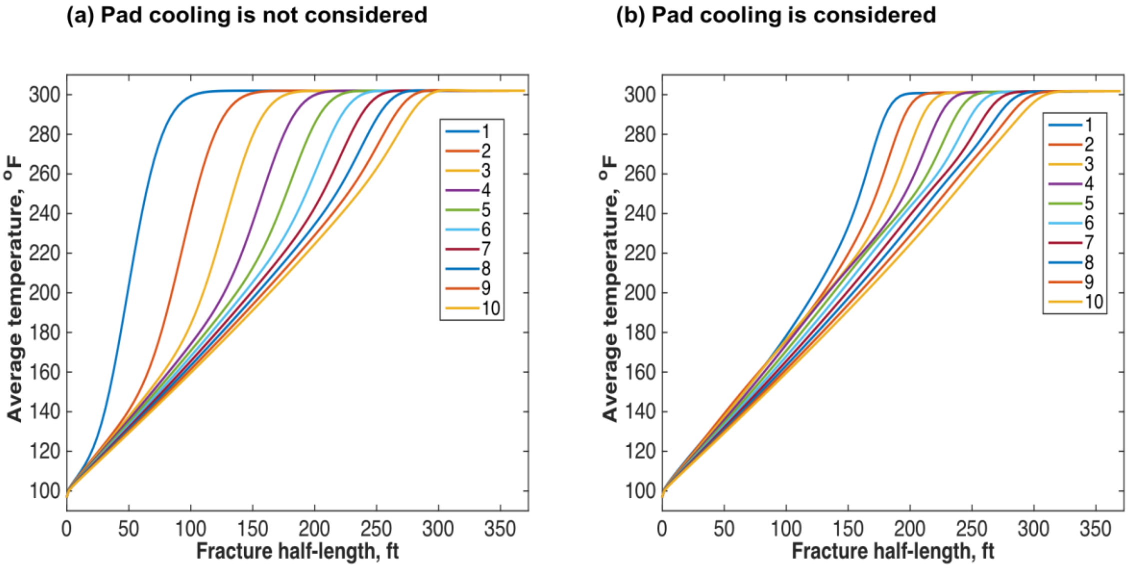

Figure 4.31: Acid temperature profiles at different time steps to quantify the first stage pad fluid's cooling magnitude.

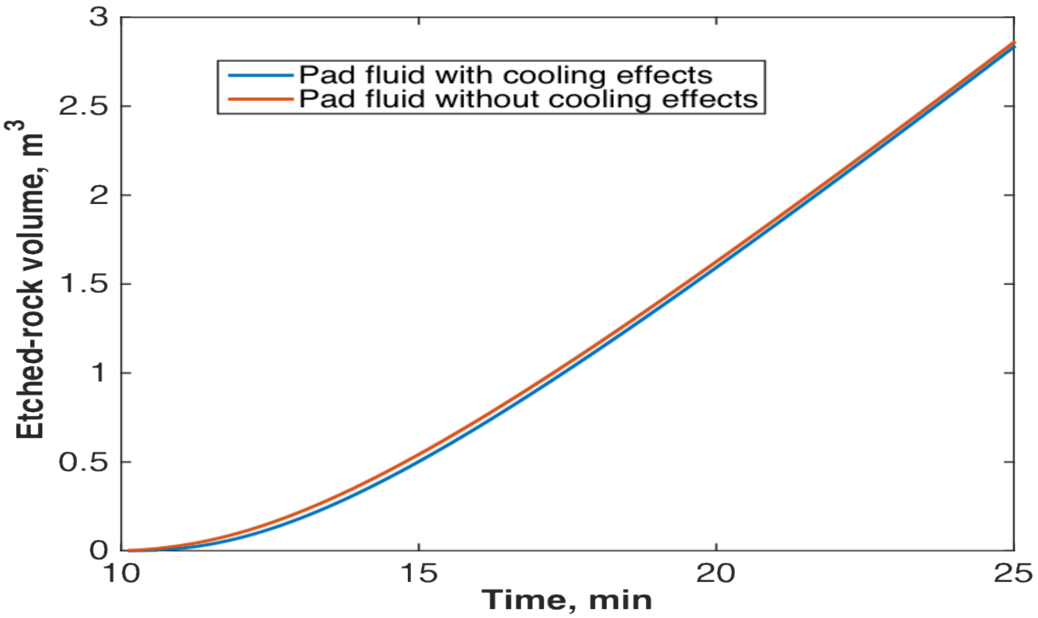

Figure 4.32: Pad fluid effect on the amount of etched rock at the fracture surfaces.

In general, the injection of pad fluid will improve acid penetration and generate a more uniform etching profile by creating wider and longer fractures. However, this change in the etching profile is not caused because of the pad fluid's cooling effects. It is important to note that if the pay zone is bounded by unstable layers, selection of the pad fluid's viscosity and injection rate should be considered carefully to prevent growth to an undesired height, as discussed in Sections 4.4 and 4.5.

4.12 Water Flush Effects

The fracture is usually flushed with water as a final stage, to reduce corrosion from acid traces in the wellbore. This may also enhance the acid penetration distance. In this section, the viscous fingering effect was not modeled and the fracture was assumed to stay open during water injection. The properties of the injected water are shown in Table 4.4.

Table 4.4: Input Data for the Last Stage Water Flush

Water Flush Properties		
Input Data	**SI Unit**	**Field Unit**
Density, ρ	1000 Kg/m^3	62.4 lb$_m$/ft^3
Injection rate, q_i	0.08 m^3/s	30 bpm
Treatment time, t_e	600 s	10 min
Power law exponent, n	1.0	
Consistency index, K	0.0002 lb$_f$.s^n/ft^2	
Spurt loss, S_p	0 m	0 gal/ft^2
Fluid loss multiplier outside pay zone, f_m	0.25	
Opening time distribution factor, κ	1.5	
Pad heat capacity, c_p	4.13 KJ/(Kg.^{o}C)	0.964 Btu/(lbm.^{o}F)
Pad thermal conductivity, k	6x10^{-4} KJ/(s.m. ^{o}C)	0.347 Btu/(hr.ft. ^{o}F)
Pad temperature at surface, T_s	27 ^{o}C	80.6 ^{o}F

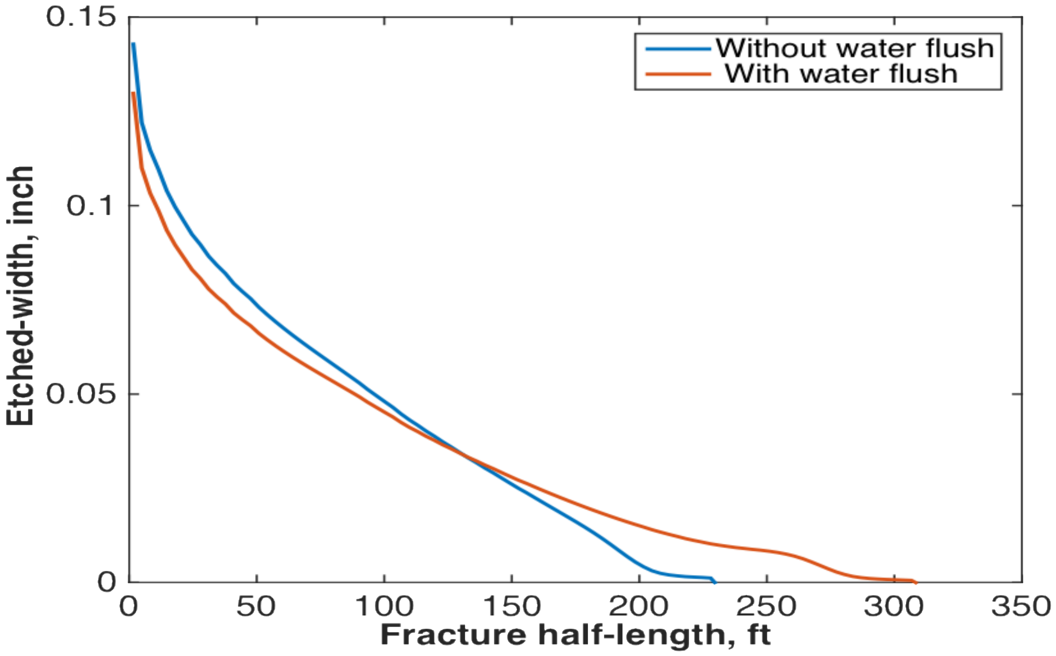

Figure 4.33: Water flush effect on the acid etched-width profile.

As discussed above, acids with high diffusion coefficients (such as straight acid) react completely during acid injection. Hence, a water flush does not improve the acid penetration distance for straight acid injected in calcite or dolomite formations. More retarded acid systems such as gelled and emulsified acids don't react completely during injection, which leaves space for water to push accumulated acid further into the fracture. The simulated case used gelled acid with a 10^{-5} cm^2/s diffusion coefficient injected into a calcite formation and followed by a water flush. The input data used in this simulation can be found in Tables 4.1 and 4.2. Figure 4.33 shows that the water flush considerably improved the acid penetration. Figure 4.34 illustrates how the water pushed the acid deeper inside the fracture at different time steps.

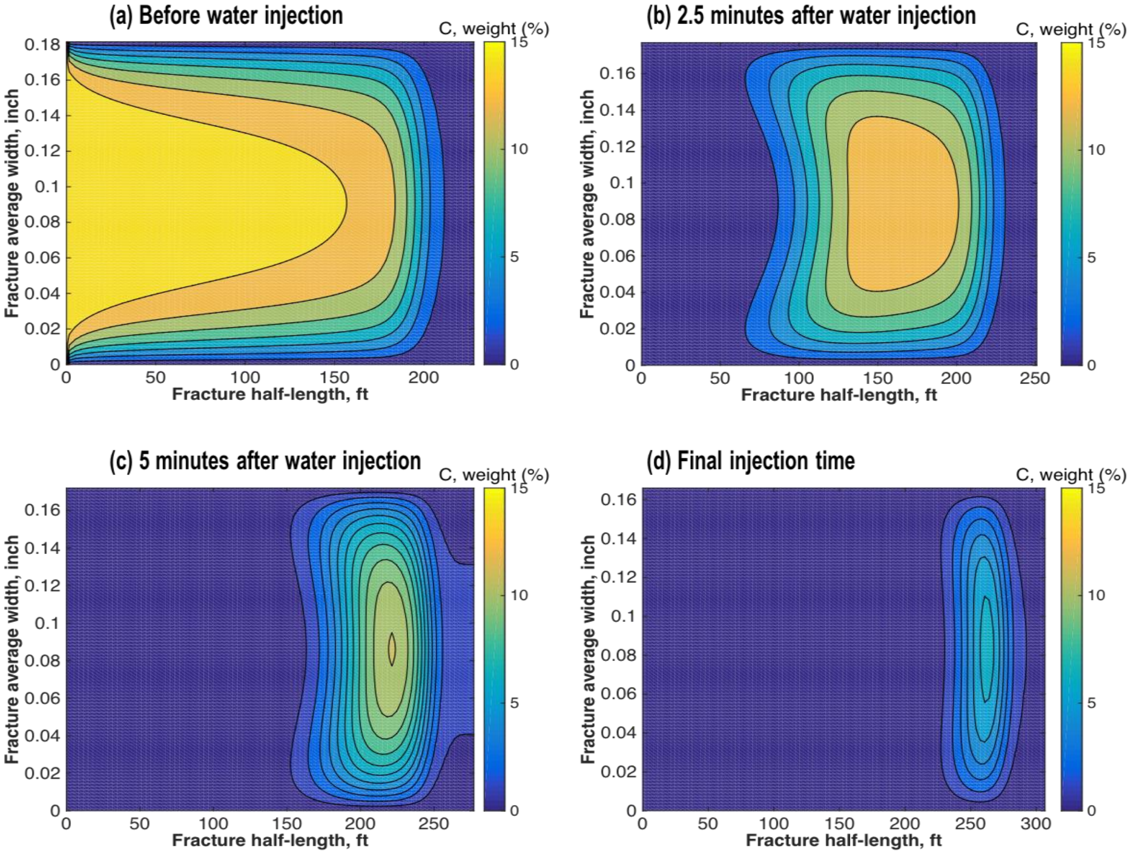

Figure 4.34: Water pushing the acid deeper inside the fracture.

4.13 Laminated Formations

Many carbonate formations are known for having different mineralogy distributions along the bedding direction. This is caused by different depositional environments encountered at various geological time scales. In this section, the pay zone was assumed to contain four layers, in the following order: dolomite, shale, calcite, and dolomite. The layers' information for this case is shown in Table 4.5. The acid diffusion coefficient was 10^{-5} cm^2/sec and the other input properties are shown in Table 4.1. Figure 4.35 shows the acid concentration, etched-width, conductivity, and temperature distribution along the fracture height and half-length. The acid concentration did not

Table 4.5: Formation Layers Input Data

Layer Number	**Top of Layer (ft)**	**Layer Thickness (ft)**	**Stress (psi)**	**Toughness (psi.inch$^{0.5}$)**	**Young's Modulus (psi)**
1	0	7900	6000	2200	$4.5x10^6$
2	7900	100	5500	1200	$4.5x10^6$
3	8000	30	4300	1100	$4.5x10^6$
4	8030	30	4000	1000	$4.5x10^6$
5	8060	30	4000	1000	$4.5x10^6$
6	8090	30	4300	1100	$4.5x10^6$
7	8120	40	5500	1200	$4.5x10^6$
8	8160	500	6000	2200	$4.5x10^6$
Layer Number	**Poisson's Ratio**	**Perforation**	**Minerology**	**Porosity**	**Permeability (md)**
1	0.25	No	Shale	0.10	1.5
2	0.25	No	Shale	0.08	1.2
3	0.25	Yes	Dolomite	0.14	1.0
4	0.25	Yes	Calcite	0.14	1.0
5	0.25	Yes	Shale	0.14	1.0
6	0.25	Yes	Dolomite	0.14	1.0
7	0.25	No	Shale	0.13	0.5
8	0.25	No	Shale	0.10	0.1

change in the non-reactive shale layer (see Fig. 4.35a). The etched-width was at its maximum in the most reactive calcite formation, hence the fracture conductivity (see Figs. 4.35c and 4.35d). The acid required a longer distance to reach the reservoir temperature in the shale formation because no heat of reaction was generated (see Fig. 4.35b).

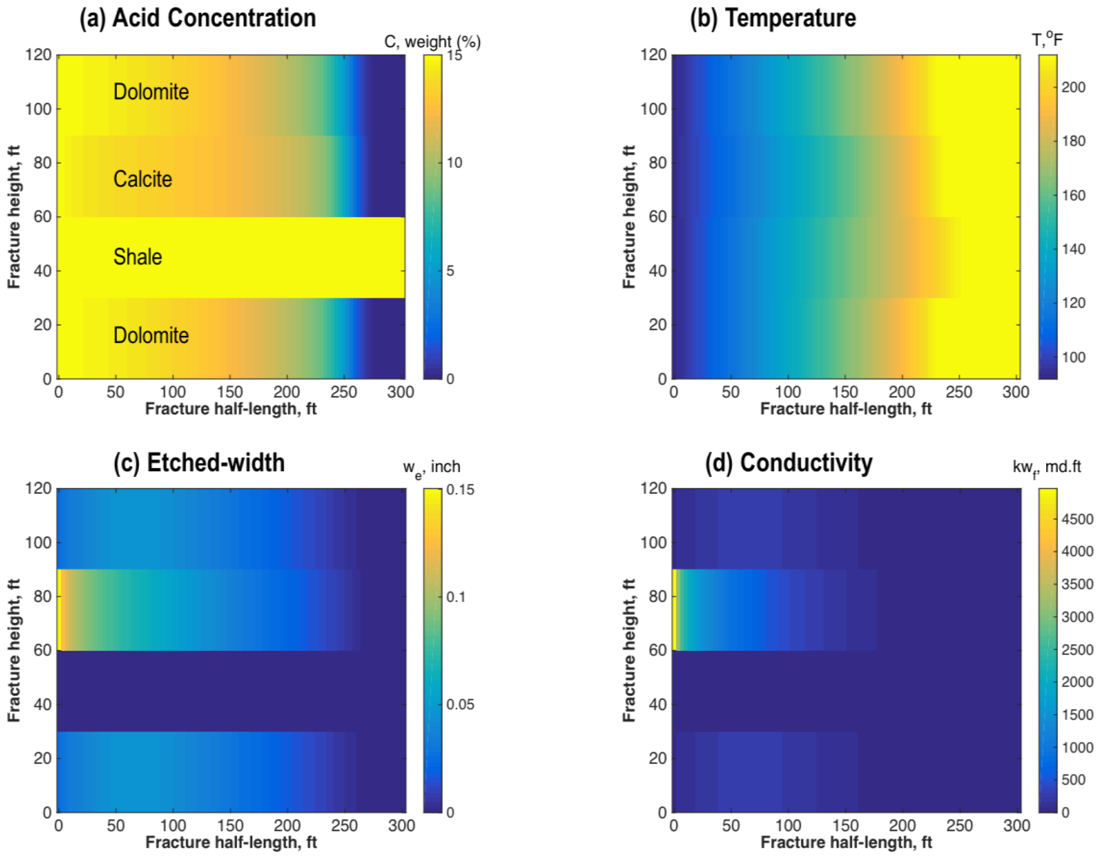

Figure 4.35: Acid, temperature, etched width, and conductivity solution across the fracture half-length and height for the multi-layer formation case.

As the fracture closes, the fracture temperature increases until it reaches the reservoir temperature. The temperature increase in each layer is a function of the etched-width distribution and heat of reaction. Since a post flush is usually used as the final stage, the warming near the fracture entrance is not affected by the heat of reaction, but rather by the etched-width magnitude. Wider segments of the fracture need longer time to warm up because a larger amount of cold fluid is being heated. This behavior can be used to identify the reactivity of each layer based on transient temperature measurements taken while the fracture closes. Behind casing sensors can be used to do this job. The fracture entrance etched-width distribution along the fracture height can also be calculated by minimizing the error between the measured and calculated temperatures. To understand the warming behavior of a laminated formation, a similar case was run with a water flush as the final stage (see Table 4.4). Figure 4.36a shows the warming behavior at the fracture entrance at different closure times. There was a noticeable temperature difference between the different layers during the fracture closure at the fracture's entrance. Shale took less time to warm compared to carbonate since no etching occurred (see Fig. 4.36b). Because the etching was at its maximum at the calcite layer, it required the longest time to warm up to the reservoir temperature. It is important to mention that the temperature difference between the layers might be amplified because of the assumption of no convection on fracture height direction.

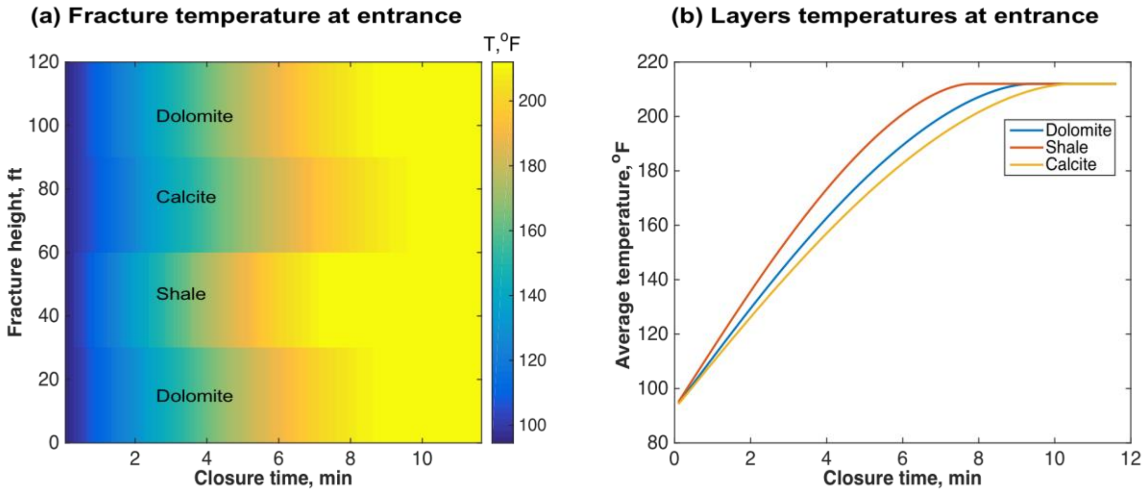

Figure 4.36: Temperature differences among the different layers during fracture closure.

CHAPTER V

OPTIMIZATION CASE STUDY

Changing design parameters such as the injection rate, acid concentration, acid viscosity, and stages of fluid injection can also significantly change fracture productivity. Due to its complexity, optimizing acid fracture operation has not received as much attention as proppant fracturing. Economides et al. (2002) suggested a unified design methodology for proppant fracturing by introducing the proppant number concept, N_p. For a given amount of proppant, there is an optimum fracture length and width that will result in a fracture with maximum productivity. Hence, fluid viscosity, injection rate, and pumping schedule should be designed to achieve that optimum fracture. One major issue with acid fracturing is predicting the fracture permeability or conductivity. Acid fracture permeability is impossible to predict accurately and variations can be dramatic along the fracture half-length. Ravikumar et al. (2015) used the proppant number concept for acid fracture optimization. Using a proppant number requires an average fracture conductivity value. Thus, the validity of using a single average conductivity is investigated in the following section.

5.1 Arithmetic Mean Conductivity

As presented in Chapter 4, acid fracturing results in a variable distribution of fracture conductivity along its surfaces. The joined reservoir simulator was used to test the validity of averaging the acid fracture conductivity. An arithmetic mean was used in this case to average the conductivity distribution. The case was tested for an acid fracture in a homogenous calcite pay zone and assuming that the acid had low, medium, or high diffusion coefficients. Different diffusion coefficients resulted in different conductivity distribution profiles. Tables 4.1 and 4.5 were used as input data, except that the pay zone was made of calcite minerology. The leakoff coefficient was 10^{-3} ft/min$^{0.5}$ and the diffusion coefficients were 5x10^{-4}, 10^{-5}, and 10^{-6} cm^{2}/s. Figure 5.1 shows that the predicted fracture productivity obtained using an average conductivity contradicted that obtained from the distributed fracture conductivity. The average conductivity approach showed that the least-retarded acid (straight acid, in this case) gave the best productivity. However, when the distributed conductivity profile was used as input into the reservoir simulator, the same acid system gave the lowest fracture productivity. It was observed that the distribution of fracture conductivity had an impact on the productivity, as the assumption of a single average conductivity could not estimate. Figure 5.1b shows that the range of productivity error produced by using a single average conductivity was not negligible. The maximum error occurred in the high acid diffusion coefficient case, where fracture conductivity was the least uniform. The range of error could be more significant if the formation is laminated. In conclusion, using a 3D reservoir simulator that captures fracture surface conductivity distribution is essential to the correct estimation of acid fracture productivity.

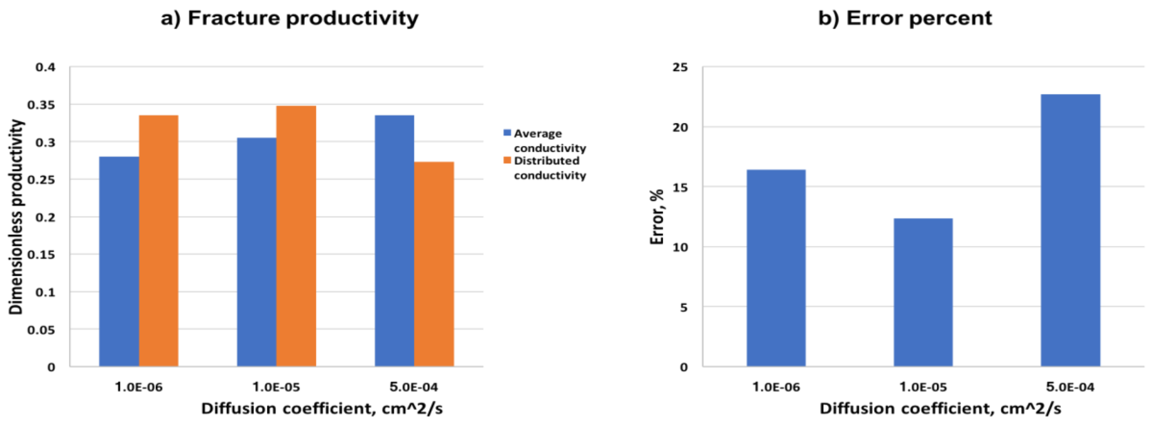

Figure 5.1: Effect of averaging acid fracture conductivity on fracture productivity.

5.2 Optimum Treatment Volume

One question that needs to be answered regarding optimizing an acid fracturing job is what treatment volume of acid should be invested. All acid fracture conductivity correlations assume that larger etching profiles result in higher conductivity and, hence, better productivity. That means that larger volumes of acid injection should increase fracture productivity. However, this assumption is inaccurate for cases in which rocks are weakened by the acid reaction. The rock weakening effect was not captured by the conductivity correlations in the literature and was not considered in this study. To determine the optimum acid treatment volume, a chart of the acid treatment volume versus fracture productivity should be generated.

In this research, the chart was produced using Tables 4.1 and 4.5 as input data, assuming a 10^{-3} ft/min$^{0.5}$ leakoff coefficient and 10^{-5} cm^2/s acid diffusion coefficient. The simulated reservoir was assumed to have a 250 m length and 250 m width. Different acid treatment volumes were simulated to estimate the corresponding fracture productivity. Figure 5.2 shows two slopes, one sharp slope at relatively small treatment volumes and another flat slope at large treatment volumes. Initially, fracture productivity increased significantly with the increase in acid volume. Then, there was a point where the increase in acid volume did not correspond to the considerable increase in productivity. This occurred because the fracture was already almost fully penetrating the simulated reservoir volume (SRV) with high conductivity. An engineer might choose a treatment volume where the curve’s first slope begins changing, after which an increase in cost (treatment volume) would not be justified by the productivity increase. In this case, the optimum treatment volume would be around 10^5 gallon. This is the treatment volume where no sharp improvement in productivity is expected by exceeding it. However, an economic analysis should be incorporated to precisely determine the amount of acid that should be invested. The productivity versus treatment chart is specific to the reservoir and specified design conditions. Changing the design parameters would change the optimum treatment volume. However, using the optimized design parameters can produce the same productivity improvement with the lowest treatment volume.

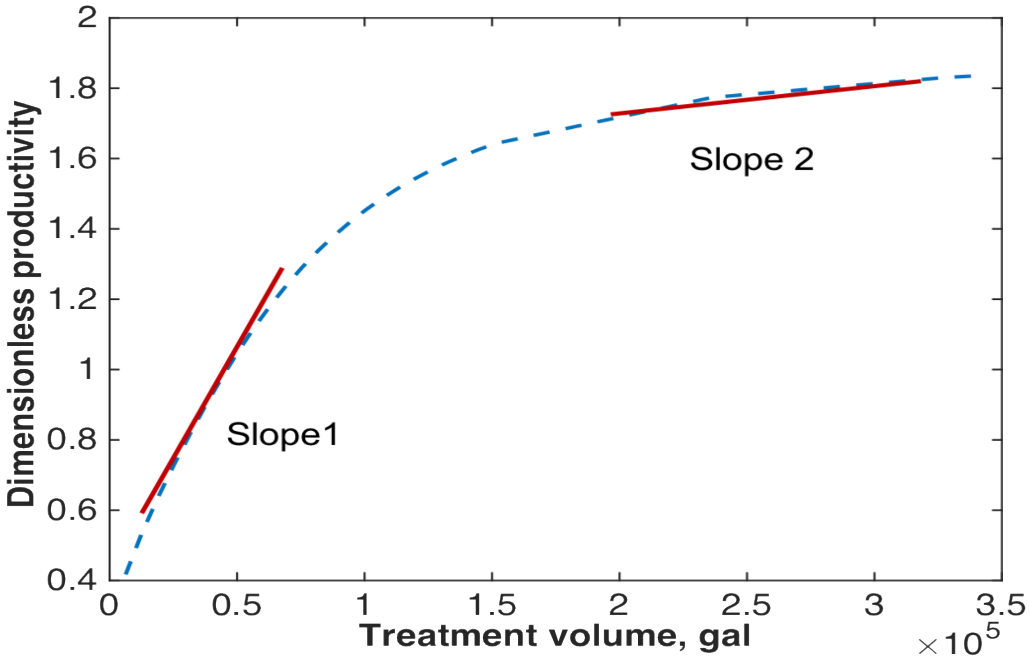

Figure 5.2: Optimum acid treatment volume chart.

5.3 Case Study

It is necessary to study the reservoir properties to achieve the appropriate acid fracturing design. Given a certain acid treatment volume, a variation of acid penetration lengths and conductivity distributions can be created. Acid penetration length and etched-width magnitude are usually inversely related at a certain acid volume. Tight reservoirs are more productive with long fractures, while high permeability reservoirs perform better with high conductivity fractures. A reservoir simulator should be used to determine the optimal etching profiles for a certain formation and acid treatment volume. The design parameters should then be changed accordingly to achieve a favorable etched-width profile.

Table 5.1: Fluid Treatment Schedule for the Optimization Case Study

Stage	Flow Rate (bpm)	Injection Time (min)	Consistency Index $(\mathbf{lb_f.s^n/ft^2})$	Power Law Exponent	Acid Concentration (wt.%)
Viscous Pad	60	10	0.005	0.85	0
Gelled Acid	60	30	0.0009	0.9	15
Water Flush	60	5	0.00002	1.0	0

Table 5.2: Formation Layer's Properties for the Optimization Case Study

Layer Number	Top of Layer (ft)	Layer Thickness (ft)	Stress (psi)	Toughness (psi.inch$^{0.5}$)	Young's Modulus (psi)
1	0	7900	5500	2200	4.5x10^{6}
2	7900	100	4550	1200	4.5x10^{6}
3	8000	120	4300	1100	4.5x10^{6}
4	8120	40	4600	1200	4.5x10^{6}
5	8160	500	6000	2200	4.5x10^{6}
Layer Number	**Poisson's Ratio**	**Perforation**	**Minerology**	**Porosity**	**Permeability (md)**
1	0.25	No	Shale	0.10	1.0
2	0.25	No	Shale	0.08	1.0
3	0.25	Yes	Calcite	0.14	1.0
4	0.25	No	Shale	0.13	1.0
5	0.25	No	Shale	0.10	1.0

A synthetic case study was created for this research, assuming a relatively good permeability reservoir. The acid fracture was initially designed at a high injection rate for high viscosity fluids. The input data are shown in Tables 5.1 to 5.2. Viscous pad fluid was first injected to create the fracture, then gelled acid was used to etch the fracture walls. Finally, water was injected to reduce corrosion and push the acid deeper into the formation.

The dimensions of the created fracture at the final injection time step were 520 ft for the half-length, 263 ft for the fracture height, and 0.16 in for the average fracture width. The apparent viscosities of the fluids were 103 cp for the viscous pad, 25 cp for the gelled acid, and 1 cp for the water flush. The leakoff coefficients and acid diffusion coefficient were calculated in the simulator. The calculated gelled acid diffusion coefficient at room temperature was $8\text{x}10^{-6}$ $\text{cm}^2\text{/s}$, while the leakoff coefficients for each fluid stage were $1.4\text{x}10^{-3}$ $\text{ft/min}^{0.5}$, $2.3\text{x}10^{-3}$ $\text{ft/min}^{0.5}$, and $2.9\text{x}10^{-3}$ $\text{ft/min}^{0.5}$. Figure 5.3a shows the fracture width along the fracture height at the fracture entrance as the fracture propagated. The red lines represent the pay zone, which was a calcite formation. The fracture width was larger at the top of the pay zone and decreased towards the lower tip, representing an asymmetric case. The red curve in Figure 5.3b shows the fracture net pressure during injection; the blue curve is the net pressure during shutdown. The net pressure first increased as the pad fluid was injected, then stabilized during the gelled acid treatment, and slightly dropped during the water flush. Then, the net pressure decreased while the fracture was closing after shut-in. Figure 5.4 shows the 2D and averaged 1D etched-width and conductivity distribution profiles. The variations in acid etched-width along the fracture height were due to the variable fracture width. The retarded acid penetrated around 480 ft of the created fracture half-length. The initial dimensionless productivity of the wellbore, J_0, before creating the fracture was around 0.16.

The fracture improved the productivity of the wellbore to around 0.75, approximately a 4.7-fold increase.

It is possible to optimize the fracture productivity for the same treatment volume. Understating that the reservoir permeability, 1 md, is relatively high, an engineer might design a shorter and more conductive fracture, which in turn might improve wellbore productivity. The fluids viscosities, injection rate, and acid concentration could be altered in a such way that they create a favorable fracture. The following sections show how the design parameters can be changed to achieve a more productive fracture.

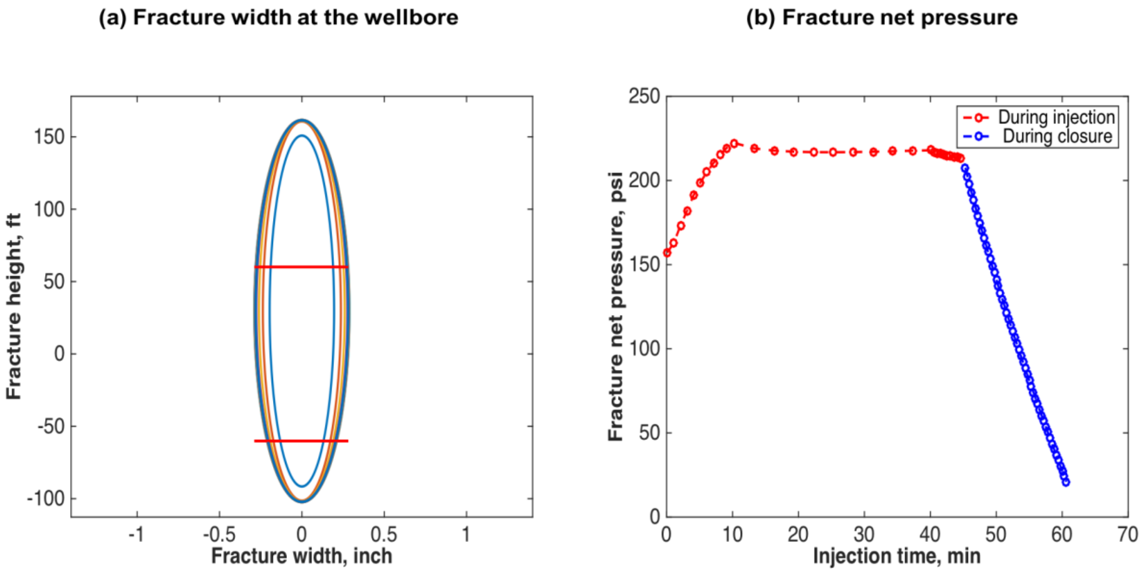

Figure 5.3: Fracture geometry and net pressure during treatment time.

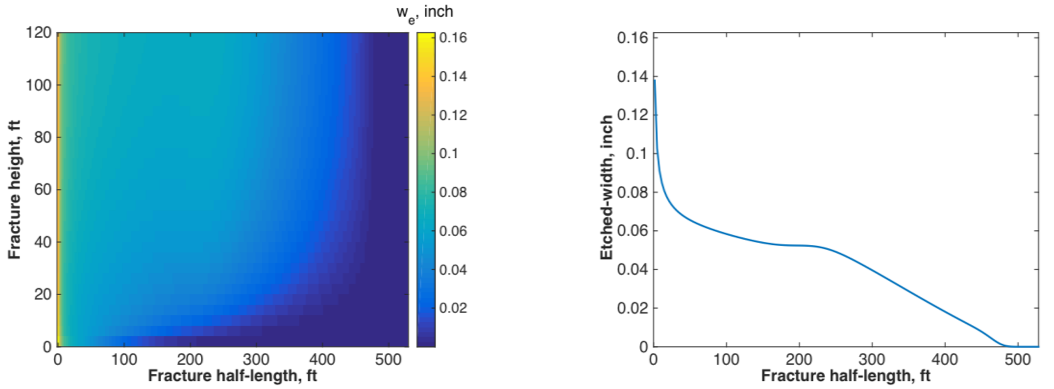

(a) 2D etched-width profile

(b) 1D average etched-width profile

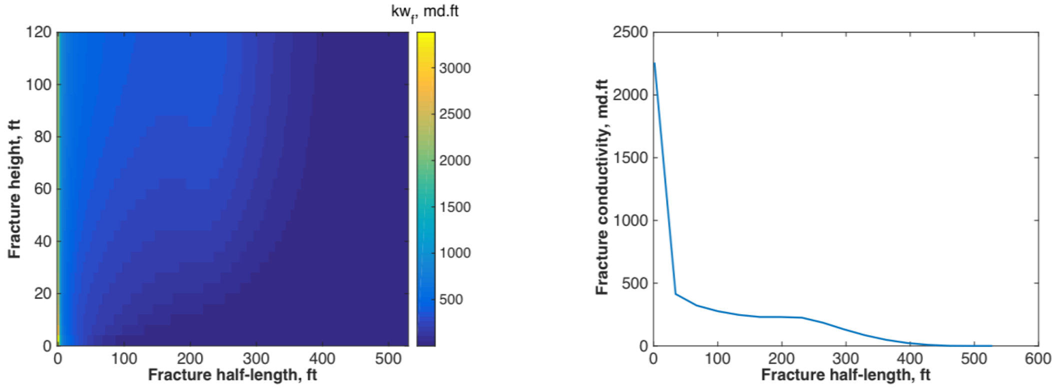

(c) 2D conductivity profile

(d) 1D average conductivity profile

Figure 5.4: 2D and 1D etched-width and fracture conductivity profiles.

5.3.1 Optimizing Fluid Viscosity

In the original case, pad and gelled acid large viscosities helped creating a large height fracture. In this case, the pay zone was bounded by unstable layers, meaning that the fluid viscosities needed to be carefully studied. A substantial amount of acid was lost to undesirable layers reducing the etching in a calcite formation. For this research, a case was simulated where the pad fluid and gelled acid viscosities were reduced to 9 cp and 5 cp compared to the original case by reducing the consistency indices to 0.0005 and 0.0002 $lb_f . s^n/ft^2$, respectively. Reducing the viscosities resulted in higher acid diffusion and leakoff coefficients. The calculated acid diffusion coefficient at room temperature was 4x10^{-5} cm2/s, while the leakoff coefficients for each stage were 2.4x10^{-3}

ft/min$^{0.5}$, 2.6x10^{-3} ft/min$^{0.5}$, and 2.7x10^{-3} ft/min$^{0.5}$, respectively. In this case, the created fracture was less efficient; however, the height, 226 ft, was smaller, thus reducing the acid lost to the undesirable layers. Since the created average width, 0.09 in, was smaller and the diffusion coefficient larger, the acid penetration distance was reduced to 350 ft in favor of higher etching and a better conductivity profile (see Fig. 5.5). This combination of acid penetration distance and fracture conductivity profile resulted in better well productivity, 0.95, representing a 27% improvement over the initial case.

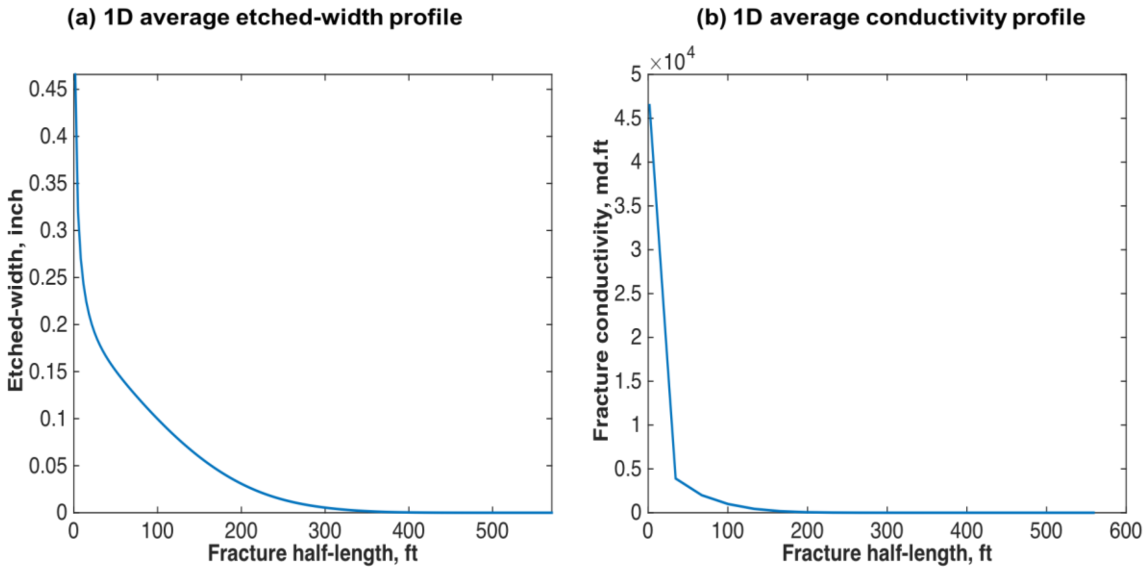

Figure 5.5: Etched-width and conductivity profiles for the optimized fluid viscosities case.

5.3.2 Optimizing the Injection Rate

Another way to achieve a favorable acid penetration length and conductivity profile is by changing the injection rate. The case simulated for this research assumed that the injection rate was reduced by half for all stages, 30 bpm, without changing the treatment volumes. The diffusion and leakoff coefficients did not change significantly with the change in injection rate, even though a less efficient fracture was created. As discussed above, reducing the injection rate reduces the acid penetration and increases the etched-width magnitude and, hence, the fracture conductivity (see Fig. 5.6). The fractured wellbore dimensionless productivity increased to 0.9. As compared to the original case, this represented a 21% increase in productivity, which was attributable to the better design of the etched-width profile along the acid penetration length.

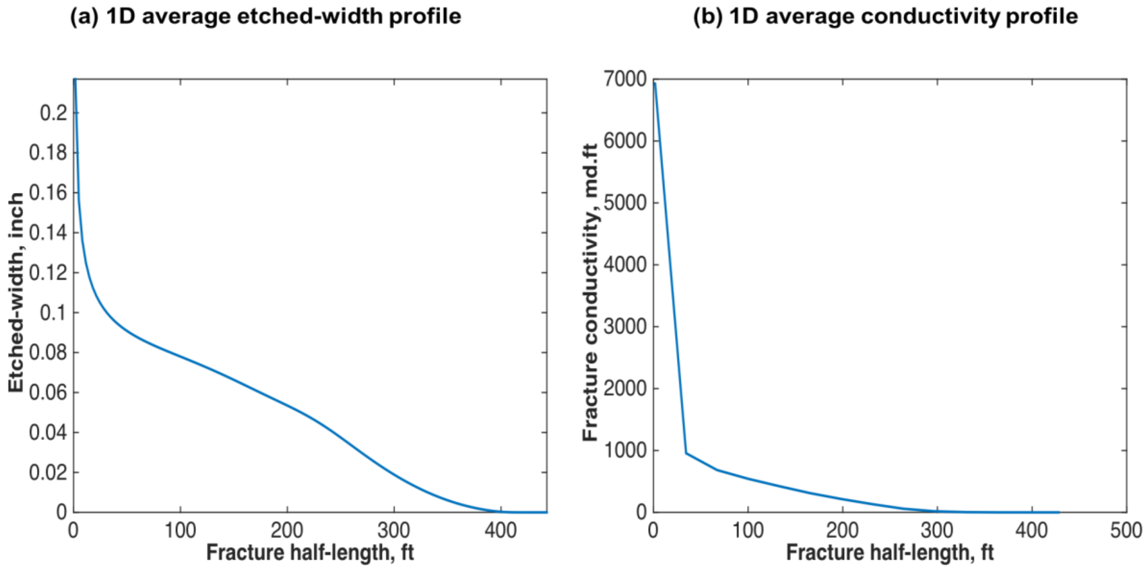

Figure 5.6: Etched-width and conductivity profiles for the optimized injection rate case.

5.3.3 Optimizing Acid Concentration

In the original case, the simulation was based on a 15% acid weight concentration. In this case, the acid concentration increased to 28%. This was accomplished by reducing the gelled acid mixture volume while keeping the HCl acid amount constant. The treatment time of the gelled acid was reduced to around 16 minutes because of the reduction in total treatment volume. The calculated diffusion and leakoff coefficients were close to the original case. A minor increase in the etching profile at around 200 ft occurred because the remaining concentrated acid reacted mostly at that location during fracture closure that happened after water flush (see Fig. 5.7). The magnitude of the etching profile is comparable to the original case, while the acid penetration is shorter. The produced fracture productivity is also comparable to the original case. However, the gelled acid treatment volume was reduced significantly to produce the same result.

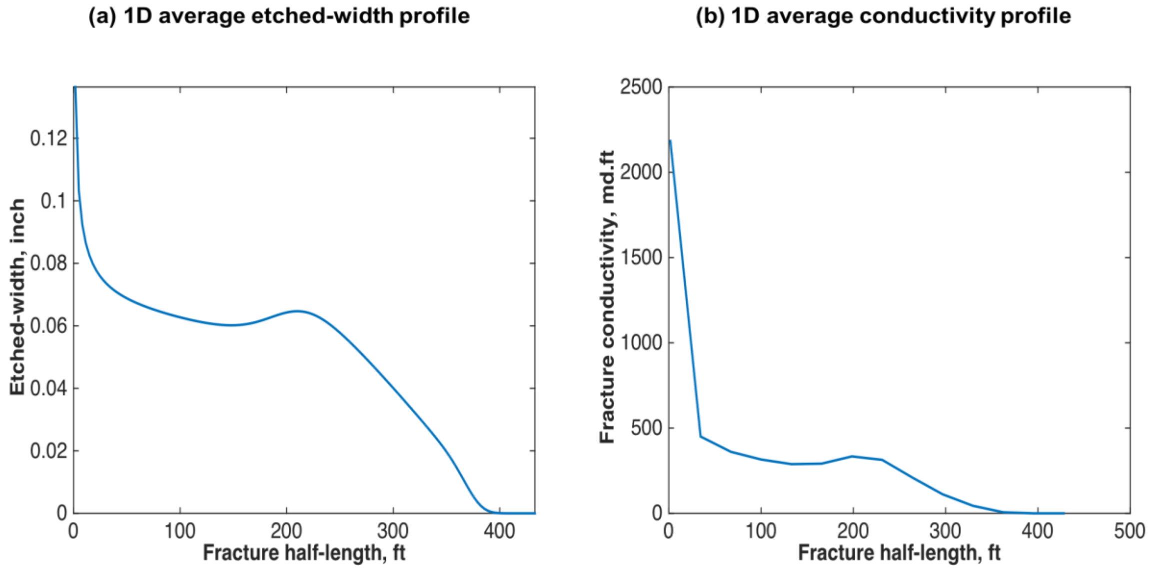

Figure 5.7: Etched-width and conductivity profiles for the optimized acid concentration case.

In this chapter, injection rates, fluids viscosity, and acid concentration were changed to produce a favorable acid penetration length and etched-width profile, from which fracture productivity was increased and acid treatment volume was reduced. For the studied case, the reservoir permeability was relatively high and the pay zone bounding layers unstable. The most favorable fracture had a higher etched-width magnitude, which came at the expense of the acid penetration distance (see Fig. 5.5). For cases in which reservoir permeability is low and the pay zone is located between stable layers, a longer acid penetration distance (at the expense of the etching magnitude) should be targeted by changing the design parameters accordingly.

CHAPTER VI

SUMMARY AND RECOMMENDATIONS

6.1 Model Summary

The developed model integrated an acid model with fracture propagation, heat transfer, and reservoir models. It included injection of multiple fluid systems that were either reactive (i.e., straight, emulsified, and gelled acids) or non-reactive (i.e., pad fluid and flush). The model incorporated multiple layer formations with different rock and kinetic properties. Leakoff was calculated for each layer and the wormhole effect was included if a reaction took place. When the injection stopped, acid concentration and etching were solved as the fracture closed. As the final etching profile was drawn, conductivity was calculated using a correlation that considered formation heterogeneity. Finally, well productivity was numerically calculated by simulating the reservoir fluid flow and considering the obtained fracture with variable conductivity.

The sensitivity analysis indicated that wider and shorter height fractures and lower acid diffusion coefficients resulted in longer acid penetration distances. Lower leakoff coefficients contributed to longer acid penetration if the acid injection was described as fluid loss limited. Higher injection rates and acid viscosity led to a higher acid penetration distance in contained pay zones. In poorly bounded pay zones, certain injection rates and acid viscosities resulted in a decreasing acid penetration distance because of an excessive fracture height increase. Longer acid penetration resulted in more uniform etched-width profiles. The acid concentration at a certain treatment volume had no impact on the acid penetration distance, but significantly affected the etched-width profile. The maximum etched-width value was at the fracture entrance for calcite formations but away from entrance for dolomite formations.

Straight HCl acid reacted primarily during injection in calcite formations. However, a significant amount of acid was consumed during fracture closure when retarded acid systems were used, especially in dolomite formations. The model shows that obtaining accurate acid solutions requires simulating the acid reaction during fracture closure. Some simulated cases showed that more than 30% of fracture surface etching occurred during closure.

The model illustrates the significance of coupling fracture propagation with an acid model. The model showed that injection of a first-stage retarded HCl acid systems would not produce a uniform etched-width distribution along the fracture half-length in calcite formations. For extremely high Peclet numbers representing very retarded acid systems, a constant drop (until reaching zero) in the etched-width value at the fracture tip is theoretically obtainable. For lower Peclet numbers, the etching profile was shown to significantly decline towards the fracture end. This is in contrast to the conventional non-coupled approach from which a roughly constant etching profile is obtained at moderate to high Peclet numbers. It was also observed that the simulation of retarded acid injection in non-coupled constant fracture geometry overestimated the acid penetration distance. However, coupling fracture propagation for straight HCl acid injection did not result in a noticeable difference, as compared to acid solutions at a constant geometry.

It was found that using an average temperature for HCl acid injection in calcite formations is reasonable. Nevertheless, the temperature profile should be coupled to obtain an accurate solution when dolomite formations are considered. The reservoir temperature had a negligible effect on the etching profile and acid penetration distance when the HCl acid reacted with calcite minerals. However, the effect was significant in dolomite formations. The heat of reaction was found to produce less than a 15 °F temperature increase in the simulated cases. The heat of reaction did not affect the acid solution for calcite formations, and the effect was negligible for dolomite formations.

Pad fluid injection enhanced the acid penetration distance by creating longer and wider fractures. However, the pad’s cooling effect did not significantly contribute to acid penetration enhancement. A more uniform etching profile was created when pad fluid was used to create the fracture. The reason is that traveling acid was not restricted by fracture propagation. A water flush can also enhance the acid penetration distance by pushing the remaining acid further inside the fracture. However, straight HCl acid flushing did not result in a better acid penetration length, as the acid was mostly consumed while being injected.

Evaluating acid fracture design requires coupling a reservoir simulator that considers fracture conductivity variations along the fracture surfaces. It was observed that using a single average fracture conductivity did not accurately explain the productivity of acid fractures. Also, for a certain acid treatment volume, there was an optimum etching distribution and acid penetration length that corresponded to the reservoir’s level of permeability and size. This optimum profile was obtained by changing the injection rates, viscosities, acid concentration, and pad and flush volumes. It was also found that for certain simulated reservoir volume (SRV), there was an optimum acid treatment volume. Exceeding that volume did not significantly contribute to an improvement in productivity.

6.2 Recommendations for Future Work

The model assumed that the fracture propagated as acid was injected. Field cases have shown that a fracture may close during acid injection because of excessive wormholes growing from the fracture surfaces. The model should be modified to capture this phenomenon.

Viscous fingering occurs when the viscosity contrast between two injected fluids is high. In homogenous formations, high and low viscosity stages are frequently alternated to provide differential etching. Acid fingering through viscous pad fluid is believed to create channels that enhance non-uniform etching behavior. This phenomenon was not considered in this model; a piston-like flow between the different stages was assumed.

Coupling the acid fracture and reservoir models showed that there was an optimum acid treatment volume. This volume was determined by observing the slope change in fracture productivity versus the treatment volume plot. The treatment volume could be reduced by optimizing the design parameters. An optimization procedure that considers variable fracture conductivity should be implemented to determine the optimum design parameters.

REFERENCES

Aljawad, M. S., Zhu, D., and Hill, A. D. 2016. Modeling Study of Acid Fracture Fluid System Performance. Paper SPE 179109 presented at the SPE Hydraulic Fracturing Technology Conference, The Woodlands, Texas, 9-11 February.

Barron, A., Hendrickson, A., and Wieland, D. 1962. The Effect of Flow on Acid Reactivity in a Carbonate Fracture. *JPT* **14**(4): 409-415.

Berman, A.S. 1953. Laminar Flow in Channels with Porous Walls. *J. Appl. Phys*. **24**(9): 1232-1235.

Carter, R.D. 1957. Appendix to Optimum Fluid Characteristics for Fracture Extension. *In Dill. and Prod. Prac.,* ed. G.C Howard and C.R. Fast. API 267.

Cleary, M. P. 1980. Comprehensive Design Formulae for Hydraulic Fracturing. Paper SPE 9259 presented at the Annual Technical Conference and Exhibition, Dallas, Texas, 21-24 September.

Cleary, M. P., Kavvadas, M., and Lam, K. Y. 1983. Development of a Fully Three-Dimensional Simulator for Analysis and Design of Hydraulic Fracturing. Paper SPE/DOE 11631 presented at the Low Permeability Gas Reservoirs Symposium, Denver, Colorado, 14-16 March.

Coulter, A.W., Alderman, E.N., Cloud, J.E., et al. 1974. Mathematical Model Simulates Actual Well Conditions in Fracture Acidizing Treatment Design. Paper SPE 5004 presented at the Annual Fall Meeting of the Society of Petroleum Engineers of AIME, Houston, Texas, 6-9 October.

Dake, L. P. 2001. *The Practice of Reservoir Engineering (Revised Edition).* Elsevier Science, New York City.

De Rozieres, J. 1994. Measuring Diffusion Coefficients in Acid Fracturing Fluids and Their Application to Gelled and Emulsified Acids. Paper SPE 28552 presented at the SPE Annual Technical Conference and Exhibition, New Orleans, Louisiana, 25-28 September.

Deng, J., Mou, J., Hill, A.D., and Zhu, D. 2012. A New Correlation of Acid-Fracture Conductivity Subject to Closure Stress. *SPE Prod. & Oper.* **27**(2): 158-169.

Dysart, G. R. and Whitsitt, N. F. 1967. Fluid Temperature in Fractures. Paper SPE 1902 presented at the Annual Fall Meeting of the Society of Petroleum Engineers of AIME, Houston, Texas, 1-4 October.

Economides, M., Oligney, R., and Valko, P. 2002. *Unified Fracture Design*. Orsa Press, Alvin, Texas.

Economides, M.J., Hill, A.D., and Ehlig-Economides, C. 1994. *Petroleum Production Systems*. Upper Saddle River, New Jersey: Prentice Hall, PTR.

Gangi, A. F. 1978. Variation of Whole and Fractured Porous Rock Permeability with Confining Pressure. *International Journal of Rock Mechanics and Mining Sciences & Geomechanics Abstracts* **15**(5): 249-257.

Geertsma, J. and De Klerk, F. 1969. A Rapid Method of Predicting Width and Extent of Hydraulically Induced Fractures. *JPT* **21**(12): 1571-1581.

Gong, M., Lacote, S., and Hill, A. D. 1999. New Model of Acid-Fracture Conductivity Based on Deformation of Surface Asperities. *SPEJ* **4**(3), 206-214.

Guo, J., Liu, H., Zhu, Y. et al. 2014. Effects of Acid–Rock Reaction Heat on Fluid Temperature Profile in Fracture During Acid Fracturing in Carbonate Reservoirs. *Journal of Petroleum Science and Engineering* **122**: 31-37.

Hill, A.D., Zhu, D., and Wang, Y. 1995. The Effect of Wormholing on the Fluid-Loss Coefficient in Acid Fracturing. *SPE Prod. Fac.* **10**(4): 257-263.

Kalfayan, L.J. 2007. Fracture Acidizing: History, Present State, and Future. Paper SPE 106371 presented at the SPE Hydraulic Fracturing Technology Conference, College Station, Texas, 29-31 January.

Khristianovic, S.A. and Zheltov, Y.P. 1955. Formation of Vertical Fractures by Means of Highly Viscous Liquid. Paper 6132 presented at the 4th World Petroleum Congress, Rome, 6–15 June.

Lamb, H. 1932. *Hydrodynamics,* sixth edition. New York: Dover Publications, Inc.

Lee, J., Rollins, J. B., and Spivey, J. P. 2003. *Pressure Transient Testing*. SPE Textbook Series Vol. 9.

Lee, M. H. and Roberts, L. D. 1980. Effect of Heat of Reaction on Temperature Distribution and Acid Penetration in a Fracture. *SPEJ* **20**(6): 501-507.

Liu, S. and Valkó, P. P. 2015. An Improved Equilibrium-Height Model for Predicting Hydraulic Fracture Height Migration in Multi-Layered Formations. Paper SPE 173335 presented at the Hydraulic Fracturing Technology Conference, The Woodlands, Texas, 3-5 February.

Lo, K.K. and Dean, R.H. 1989. Modeling of Acid Fracturing. *SPE Prod. Eng.* **4**(2): 194-200.

Lyons, J., Nasrabadi, H., and Nasr-El-Din, H. A. 2016. A Novel Pore-Scale Thermal-Fracture-Acidizing Model with Heterogeneous Rock Properties. *SPEJ* **21**(1): 280-292.

McGuire, W. J. and Sikora, V. J. 1960. The Effect of Vertical Fractures on Well Productivity. *JPT* **12**(10): 72-74.

Meyer, B. R. 1986. Design Formulae for 2-D and 3-D Vertical Hydraulic Fractures: Model Comparison and Parametric Studies. Paper SPE 15240 presented at the Unconventional Gas Technology Symposium, Louisville, Kentucky, 18-21 May.

Meyer, 2014. Fracturing Simulation. Mfrac Software.

Morita, N., Whitfill, D. L., and Wahl, H. A. 1988. Stress-Intensity Factor and Fracture Cross-Sectional Shape Predictions from a Three-Dimensional Model for Hydraulically Induced Fractures. *JPT* **40**(10): 1329-1342.

Mou, J., Zhu, D., and Hill, A.D. 2010. Acid-Etched Channels in Heterogeneous Carbonates–A Newly Discovered Mechanism for Creating Acid-Fracture Conductivity. *SPEJ* **15**(2): 404-416.

Nierode, D.E. and Kruk, K.F. 1973. An Evaluation of Acid Fluid Loss Additives, Retarded Acids, and Acidized Fracture Conductivity. Paper SPE 4549 presented at the SPE Annual Fall Meeting, Las Vegas, Nevada, 30 September – 3 October.

Nolte, K. G. 1979. Determination of Fracture Parameters from Fracturing Pressure Decline. Paper SPE 8341 presented at the SPE Annual Technical Conference and Exhibition, Las Vegas, Nevada, 23-26 September.

Nolte, K. G. 1986. A General Analysis of Fracturing Pressure Decline with Application to Three Models. *SPE Formation Evaluation* **1**(6): 571-583.

Nordgren, R. P. 1972. Propagation of a Vertical Hydraulic Fracture. *SPEJ* **12**(4): 306-314.

Oeth, C. V., Hill, A. D., and Zhu, D. 2014. Acid Fracture Treatment Design with Three-Dimensional Simulation. Paper SPE 168602 presented at the SPE Hydraulic Fracturing Technology Conference, The Woodlands, Texas, 4-6 February.

Penny, G.S. and Conway, M.W. 1989. Chapter 8, Fluid Leakoff. In *Recent Advances in* Hydraulic Fracturing, eds. J.L. Gidley, S.A. Holditch, D.E. Nierode, and R.W. Veatch, Jr., 388-393. Richardson, Texas: Society of Petroleum Engineers.

Perkins, T. K. and Kern, L. R. 1961. Widths of Hydraulic Fractures. *JPT* **13**(9): 937-949.

Perry, R. H., Green, D. W., and Maloney, J. O. 1997. *Perry's Handbook of Chemical Engineering*, seventh edition. New York City: McGraw-Hill.

Pournik, M., Zhu, D., and Hill, A. D. 2009. Acid-Fracture Conductivity Correlation Development Based on Acid-Etched Fracture Characterization. Paper SPE 122333 presented at the European Formation Damage Conference, Scheveningen, Netherlands, 27-29 May.

Ramey Jr, H. J. 1962. Wellbore Heat Transmission. *JPT* **14**(4): 427-435.

Raymond, L. R. and Binder Jr, G. G. 1967. Productivity of Wells in Vertically Fractured, Damaged Formations. *JPT* **19**(1): 120-130.

Ravikumar, A., Marongiu-Porcu, M., and Morales, A. 2015. Optimization of Acid Fracturing with Unified Fracture Design. Paper SPE presented at Abu Dhabi International Petroleum Exhibition and Conference, Abu Dhabi, UAE, 9-12 November.

Roberts, L.D. and Guin, J.A. 1975. A New Method for Predicting Acid Penetration Distance. *SPEJ* **15**(4): 277-286.

Romero, J., Gu, H., and Gulrajani, S.N. 2001. 3D Transport in Acid-Fracturing Treatments: Theoretical Development and Consequences for Hydrocarbon Production. *SPE Prod. & Fac.* **16**(2): 122-130.

Schechter, Robert S. *Oil Well Stimulation*. Englewood Cliffs, New Jersey: Prentice-Hall, Inc., 1992.

Seth, G., Reynolds, A.C. and Mahadevan, J. 2010. Numerical Model for Interpretation of Distributed-Temperature-Sensor Data During Hydraulic Fracturing. Presented at the SPE Annual Technical Conference and Exhibition, Florence, Italy, 19-22 September.

Settari, A. 1993. Modeling of Acid-Fracturing Treatments. *SPE Prod. & Fac.* **8**(1): 30-38.

Settari, A., Sullivan, R.B., and Hansen, C. 2001. A New Two-Dimensional Model for Acid-Fracturing Design. *SPE Prod. & Fac.* **16**(4): 200-209.

Sneddon, I. N. 1946. The Distribution of Stress in the Neighbourhood of a Crack in an Elastic Solid. *Proc., Roy. Soc. A* **187**(1009): 229-260.

Terrill, R.M. 1965. Heat Transfer in Laminar Flow Between Parallel Porous Plates. *International Journal of Heat and Mass Transfer* **8**(12): 1491-1497.

Valko, P. and Economides, M.J. 1995. *Hydraulic Fracture Mechanics*. Chichester, England: Jon Wiley & Sons.

Walsh, J.B. 1981. Effect of Pore Pressure and Confining Pressure on Fracture Permeability *International Journal of Rock Mechanics and Mining Sciences & Geomechanics Abstracts* **18**(5): 429-435.

Wattenbarger, R. A., El-Banbi, A. H., Villegas, M. E., et al. 1998. Production Analysis of Linear Flow into Fractured Tight Gas Wells. Paper SPE 39931 presented at the Rocky Mountain Regional/Low-Permeability Reservoirs Symposium, Denver, Colorado, 5-8 April.

Wheeler, J. A. 1969. Analytical Calculations for Heat Transfer from Fractures. Paper SPE 2494 presented at the Improved Oil Recovery Symposium, Tulsa, Oklahoma, 13-15 April.

Whitsitt, N. F. and Dysart, G. R. 1969. Effect of Temperature on Stimulation Design. Paper SPE 2497 presented at the Annual Fall Meeting of the Society of Petroleum Engineers of AIME, Denver, Colorado, 28 September -1 October.

Williams, B.B. and Nierode, D.E. 1972. Design of Acid Fracturing Treatments. *JPT* **24**(7): 849-859.

Williams, B.B., Gidley, J.L., and Schechter, R.S. 1979. *Acidizing Fundamentals*. Dallas, Texas: Society of Petroleum Engineers of AIME.

NOMENCLATURE

A	Fracture cross-sectional area
$[A]$, $[B]$	Reactants concentrations
A_f	Fracture surface area
a	Viscosity behavior-dependent constant
B	Formation volume factor
B_s	Ratio of average to wellbore net pressure after shut-in
$\bar{C}$	Average acid concentration
C_A	Acid concentration
C_c	Reservoir zone leakoff coefficient
C_{eq}	Acid equilibrium concentration
C_i	Initial acid concentration
C_L	Leakoff coefficient
$C_{L,eq}$	Equivalent leakoff coefficient
$\bar{C}_{Li}$	ith fluid average leakoff coefficient
C_v	Invaded zone leakoff coefficient
C_{vc}	The combined coefficient of C_c and C_v
$C_{v,wh}$	Invaded zone leakoff coefficient with including wormholes effect
C_w	Acid concentration at the fracture walls
C_w	Wall building leakoff coefficient
C_1, C_2	Nierode-Kruk correlation’s constants
c	Fracture half-height

c_f	Formation rock compressibility
c_{ma}	Matrix heat capacity
c_P	Heat capacity
c_r	Reservoir fluid compressibility
c_t	Formation’s total compressibility
D	Vertical wellbore depth
D_A	Effective mixing acid diffusion coefficient
$DREC$	Dissolved rock equivalent conductivity
d_{midf}	Middle fracture location
d_{ref}	Reference depth
E	Young’s modulus
$\grave{E}$	Plane strain modulus
E_x	Total energy flux in x direction
e_x	Internal and kinetic energy flux in x direction
f_a	Fraction of leaking acid reacting at the fracture walls
$f_{calcite}$	Fraction of calcite in the formation
f_m	Fluid loss multiplier outside pay zone
$f(t)$	Pressure decline function
G	Shear modulus
g	Gravity acceleration
$g(\delta)$	Function resulted from integrating $f(\delta)$
g_G	Geothermal gradient
h_f	Fracture height

h_j	jth formation layer's thickness
h_l	Heat transfer coefficient
h_{pay}	Pay zone thickness
J	Wellbore productivity
J_A	Acid flux by diffusion
K	Flow consistency index
K_I	Stress intensity factor at the fracture tips
K_{IC}	Layers' toughness
k	Fluid thermal conductivity
k_{ef}	Relative permeability of the effluent fluid
k_g	Mass transfer coefficient
k_{ma}	Matrix thermal conductivity
k_p	Reservoir fluid permeability
$\bar{k}_p$	Average reservoir permeability
k_r	Reaction rate constant
L_x	Reservoir length
L_y	Reservoir width
MW	Molecular weight
m_w	Slope of the filtrate volume to square root time curve
N_A	Total mass (or molar) flux of acid
Nt	Number of time steps
NX	Number of x-direction grids
NY	Number of y-direction grids

NZ	Number of z-direction grids
N_{Pe}	Peclet number
n_{ps}	Number of produced species
N_{Re_L}	Leakoff Reynold's number
n	Flow behavior index,
n_r	Reaction exponent,
n_{rs}	Number of reacting species
$\bar{P}$	Average reservoir pressure
P_{net}	Fracture net pressure
P_r	Reservoir pressure
P_{ref}	Reference pressure
P_w	Wellbore pressure
p	Fluid pressure
Q_{ibt}	Number of pore volumes for acid to breakthrough
q	Fluid flow rate
q	Production rate
q_i	Fluid injection rate
q_L	Leakoff rate per unit length
q_r	Heat flux from the reservoir
q_x	Conductive heat flux in x direction
R	Rate of reaction in moles per unit time
R	Universal gas constant
RES	Rock impediment strength

$R_{v,A}$	Mass (or molar) rate of the acid reaction per unit volume
r	Reaction rate in moles per unit surface area and time
r_w	Wellbore radius
r_1	Inner casing or tubing radius
r_2	Outer casing radius
S_p	Spurt loss coefficient
T	Temperature
T_b	Ambient temperature
T_D	Dimensionless Temperature
T_I	Injected fluid temperature at wellbore perforations
T_{ma}	Matrix temperature
T_s	Injected fluid temperature at the surface
T_R	Reservoir temperature
T_W	Temperature at the fracture walls
t	Time
t_e	Total time of acid injection
U	Internal energy
U_t	Overall heat transfer coefficient
u	Velocity in the x direction
u_{avg}	Average fluid velocity
u_{in}	Velocity at the inlet
V_{acid}	Acid volume
V_{rock}	Volume of porous rock dissolved

$\hat{V}$	Specific volume
v	Poisson's ratio
v	Stoichiometric coefficient
v	Velocity in the y direction
$\bar{v}_L$	Average leakoff velocity
$\overline{w}$	Fracture's average width
$\widetilde{w}$	Average fracture etched-width
w_e	Etched-width
w_i	Ideal fracture width
wk_f	Fracture conductivity
$w_{\max,0}$	Maximum fracture width at entrance
x	Fracture's length direction
x_f	Fracture half-length
y	Fracture's width direction
z	Fracture's height direction

Greek

α, β	Mou-Deng correlation's constants
β	Gravimetric dissolving power
$\dot{\gamma}$	Shear rate
ΔE	Activation energy
ΔH_f	Heat of formation
ΔH_r	Heat of reaction

δ	Dimensionless shut-in time
η	Dimensionless position at the width direction
κ	Opening time distribution factor
$\lambda_{D,x}$	Correlation length in horizontal direction
$\lambda_{D,z}$	Correlation length in vertical direction
λ_n , G_n	Terrill’s solution eigenvalues
μ	Apparent fluid viscosity
μ_{ef}	Effluent fluid viscosity
μ_r	Reservoir fluid viscosity
ρ	Fracture fluid density
ρ_{ma}	Formation matrix density
ρ_r	Reservoir fluids’ density
σ_c	Closure stress
σ_D	Normalized permeability standard deviation
σ_i	ith formation layer’s minimum horizontal stress
τ	Shear stress
$\tau(x)$	Time when the fracture reached position x
φ	Formation porosity
$\mathcal{X}$	Dissolving power

Subscripts

$+$	Upper fracture tip
$-$	Lower fracture tip

i	Formation’s layer, Fluid system
j	Formation’s layer
t	Total
0	Initial, Reference

APPENDIX A

MATHEMATICAL FORMULATION

This appendix discusses the mathematical formulation of the convection diffusion partial differential equations (PDEs) used in this research. This formulation was employed to solve for both the acid concentration and temperature profiles. The finite volume method was used to discretize the partial differential equation.

A.1 Grid Deployment

The first step in solving any partial differential equation is determining the meshing type and how the grid points are deployed. In this research, regular-shaped rectangular grid blocks were used to mesh the solution domain. Figure A.1 shows an example of how the solution domain was gridded. This illustration shows a 3 x 3 grid blocks. The grid blocks represent the control volume where mass and energy are conserved. The circles signify the locations of the concentration and temperature points, while the arrows denote the locations of the velocity vectors. The temperature and concentration points are deployed at the center of the control volumes except at the boundaries, while the velocities are deployed at the control volume boundaries. This arrangement is called “staggered” when the velocity points are not located at the concentration or temperature points. The number of grid blocks, temperature or concentration points, and velocity points are related as follows:

$$\begin{gathered} NX = 3, NY = 3 \\ NXC = NX + 2, \qquad NYC = NY + 2 \end{gathered} \tag{A.1}$$

$$NXu = NX + 1, \qquad NYu = NY + 2$$

$$NXv = NX + 2, \qquad NYv = NY + 1$$

where NXC is the number of concentration or temperature points in x direction, NYC is the number of concentration or temperature points in y direction, NXu is the number of x direction velocity points in the x direction, NYu is the number of x direction velocity points in the y direction, NXv is the number of y direction velocity points in the x direction, and NYv is the number of y direction velocity points in the y direction.

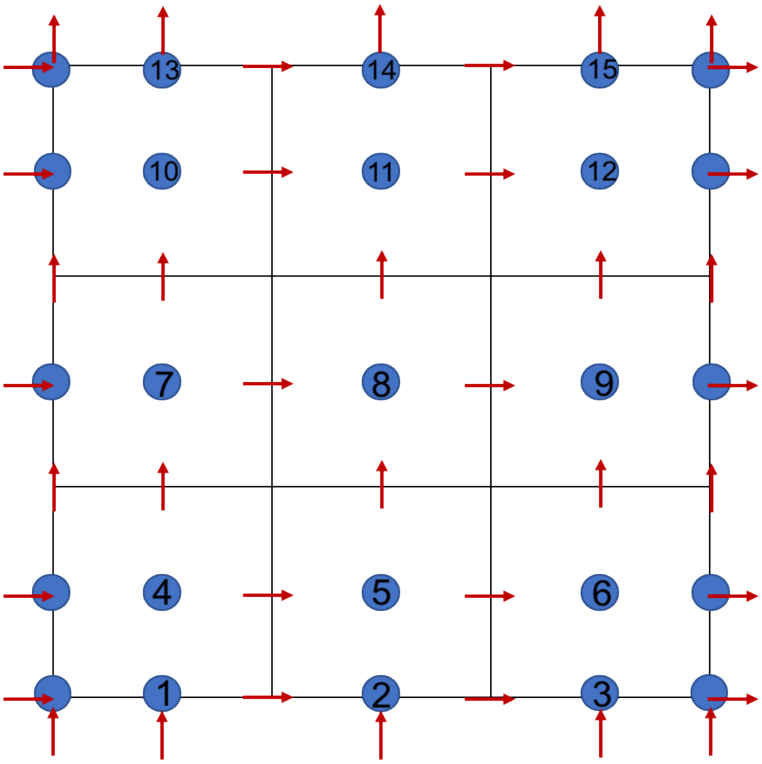

Figure A.1: Control volume and grid point deployment in the solution domain.

A.2 Interior Domain Discretization

Assuming the control volume shown in Figure A.2, the convection diffusion equation (Eq. A.2) was discretized using the finite volume method. This was done by integrating the equation over the control volume and assuming that the concentration or temperature was constant over that volume. The capital letters in Figure A.2 represent the concentration locations and the small letters are the velocity locations.

$$\frac{\partial C}{\partial t} + \frac{\partial (uC)}{\partial x} + \frac{\partial (vC)}{\partial y} = \frac{\partial}{\partial x}(\Gamma \frac{\partial C}{\partial x}) + \frac{\partial}{\partial y}(\Gamma \frac{\partial C}{\partial y}) \qquad \text{(A.2)}$$

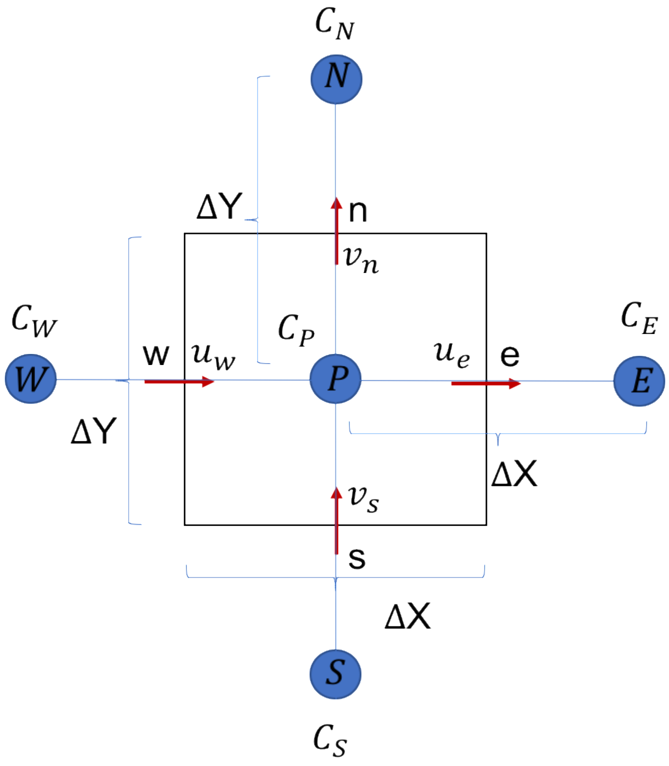

Figure A.2: Control volume showing the concentration and velocity point locations.

The transient term was integrated as follows:

$$\int_s^n \int_w^e \frac{\partial C}{\partial t} dxdy = \int_s^n \int_w^e \frac{C_P^{m+1} - C_P^m}{\Delta t}\, dxdy = \frac{C_P^{m+1} - C_P^m}{\Delta t} \Delta x \Delta y \qquad \text{(A.3)}$$

where n is north, s is south, e is east, w is west, P is the center, and m is the time step. The first convection term was integrated in a similar fashion:

$$\int_s^n \int_w^e \frac{\partial (uC)}{\partial x} dxdy = \left[(uC)_e - (uC)_w\right] * \Delta y \qquad \text{(A.4)}$$

Assuming a central difference scheme, the concentrations at the control volume boundaries were evaluated as follows:

$$(uC)_e = \frac{u_e(C_E + C_P)}{2} \qquad \text{(A.5)}$$

$$(uC)_w = \frac{u_w(C_W + C_P)}{2} \qquad \text{(A.6)}$$

where E is east and W is west. The second convection term was evaluated as follows:

$$\int_s^n \int_w^e \frac{\partial (vC)}{\partial y} dxdy = \left[(vC)_n - (vC)_s\right] * \Delta x \qquad \text{(A.7)}$$

The concentrations at the control volume boundaries were evaluated as follows:

$$(vC)_n = \frac{v_n(C_N + C_P)}{2} \qquad \text{(A.8)}$$

$$(vC)_s = \frac{v_s(C_S + C_P)}{2} \qquad \text{(A.9)}$$

where N is north and S is south. The first diffusion term was integrated over the control volume as follows:

$$\int_s^n \int_w^e \frac{\partial}{\partial x} (\Gamma \frac{\partial C}{\partial x})\, dxdy = \left[\left(\Gamma \frac{\partial C}{\partial x}\right)_e - \left(\Gamma \frac{\partial C}{\partial x}\right)_w\right] * \Delta y \qquad \text{(A.10)}$$

The gradients at the control volume boundaries were evaluated as follows:

$$\left(\Gamma \frac{\partial C}{\partial x}\right)_e = \Gamma_e \frac{(C_E - C_P)}{\Delta x} \qquad \text{(A.11)}$$

$$\left(\Gamma\frac{\partial C}{\partial x}\right)_w = \Gamma_w\frac{(C_P - C_W)}{\Delta x} \tag{A.12}$$

The second diffusion term was integrated over the control volume as follows:

$$\int_s^n\int_w^e \frac{\partial}{\partial y}(\Gamma\frac{\partial C}{\partial y})\,dxdy = \left[\left(\Gamma\frac{\partial C}{\partial y}\right)_n - \left(\Gamma\frac{\partial C}{\partial y}\right)_s\right] * \Delta x \tag{A.13}$$

The gradients at the control volume boundaries were evaluated as follows:

$$\left(\Gamma\frac{\partial C}{\partial x}\right)_n = \Gamma_n\frac{(C_N - C_P)}{\Delta y} \tag{A.14}$$

$$\left(\Gamma\frac{\partial C}{\partial x}\right)_s = \Gamma_s\frac{(C_P - C_S)}{\Delta y} \tag{A.15}$$

Putting the integrated terms together and assuming a fully implicit scheme led to the following:

$$\begin{aligned} C_P^{m+1}&\left[\frac{\Delta x\Delta y}{\Delta t} + \frac{u_e}{2}\Delta y - \frac{u_w}{2}\Delta y + \frac{v_n}{2}\Delta x - \frac{v_s}{2}\Delta x + \frac{\Gamma_e\Delta y}{\Delta x} - \frac{\Gamma_w\Delta y}{\Delta x}\right.\\ &\left.+\frac{\Gamma_n\Delta x}{\Delta y} - \frac{\Gamma_s\Delta x}{\Delta y}\right]\\ &= C_E^{m+1}\left[-\frac{u_e}{2}\Delta y + \frac{\Gamma_e\Delta y}{\Delta x}\right] + C_W^{m+1}\left[\frac{u_w}{2}\Delta y + \frac{\Gamma_w\Delta y}{\Delta x}\right]\\ &+ C_N^{m+1}\left[-\frac{v_n}{2}\Delta x + \frac{\Gamma_n\Delta x}{\Delta y}\right] + C_S^{m+1}\left[\frac{v_s}{2}\Delta x + \frac{\Gamma_s\Delta x}{\Delta y}\right]\\ &+ C_P^m[\,\frac{\Delta x\Delta y}{\Delta t} \end{aligned} \tag{A.16}$$

The following variables were defined as follows:

$$F_e = u_e\Delta y,\qquad F_w = u_w\Delta y,\qquad F_n = v_n\Delta x,\qquad F_s = v_s\Delta x \tag{A.17}$$

$$D_e = \frac{\Gamma_e\Delta y}{\Delta x},\qquad D_w = \frac{\Gamma_w\Delta y}{\Delta x},\qquad D_n = \frac{\Gamma_n\Delta x}{\Delta y},\qquad D_s = \frac{\Gamma_s\Delta x}{\Delta y} \tag{A.18}$$

$$P_e = \frac{F_e}{D_e},\qquad P_w = \frac{F_w}{D_w},\qquad P_n = \frac{F_n}{D_n},\qquad P_s = \frac{F_s}{D_s} \tag{A.19}$$

From Eq. A.16, the following coefficients were defined as follows:

$$a_E = -\frac{F_e}{2} + D_e \tag{A.20}$$

$$a_W = \frac{F_w}{2} + D_w \tag{A.21}$$

$$a_N = -\frac{F_n}{2} + D_n \tag{A.22}$$

$$a_S = \frac{F_s}{2} + D_s \tag{A.23}$$

$$a_P^0 = \frac{\Delta x \Delta y}{\Delta t} \tag{A.24}$$

$$b = a_P^0 \, C_P^m \tag{A.25}$$

$$a_P = a_E + a_W + a_N + a_S + a_P^0 + (F_e - F_w) + (F_n - F_s) \tag{A.26}$$

From applying the continuity equation, the coefficient in Eq. A.26 was written as:

$$a_P = a_E + a_W + a_N + a_S + a_P^0 \tag{A.27}$$

The discretized equation for each control volume was then written as:

$$a_P C_P^{m+1} = a_E C_E^{m+1} + a_W C_W^{m+1} + a_N C_N^{m+1} + a_S C_S^{m+1} + b \tag{A.28}$$

The coefficients in Eq. A.28 that were defined in Eqs. A.20 to A.27 were based on the central difference scheme, but could be written in a general form, as follows (Patankar, 1980):

$$a_E = D_e \, A(|P_e|) + [\![-F_e, 0]\!] \tag{A.29}$$

$$a_W = D_w \, A(|P_w|) + [\![0, F_w]\!] \tag{A.30}$$

$$a_N = D_n \, A(|P_n|) + [\![-F_n, 0]\!] \tag{A.31}$$

$$a_S = D_s \, A(|P_s|) + [\![0, F_s]\!] \tag{A.32}$$

For the central difference scheme:

$$A(|P|) = 1 - 0.5\,|P| \tag{A.33}$$

For the upwind scheme:

$$A(|P|) = 1 \tag{A.34}$$

For the power law scheme:

$$A(|P|) = [\![0, (1 - 0.1|P|^5)]\!] \tag{A.35}$$

The power law scheme was used in this model since it performed better at low and high Peclet numbers. The central difference was accurate only at low Peclet numbers, while the upwind scheme was accurate at high Peclet numbers.

Special attention must be paid to the boundary grid blocks. For instance, let's assume the west boundary grid blocks were discretized. As Figure A.3 shows, the distance between C_P and C_W was $\Delta x/2$. Hence, the following needed to be modified:

$$D_w = \frac{\Gamma_w \Delta y}{\Delta x/2} \tag{A.36}$$

A similar approach was applied to the other boundaries' grid blocks.

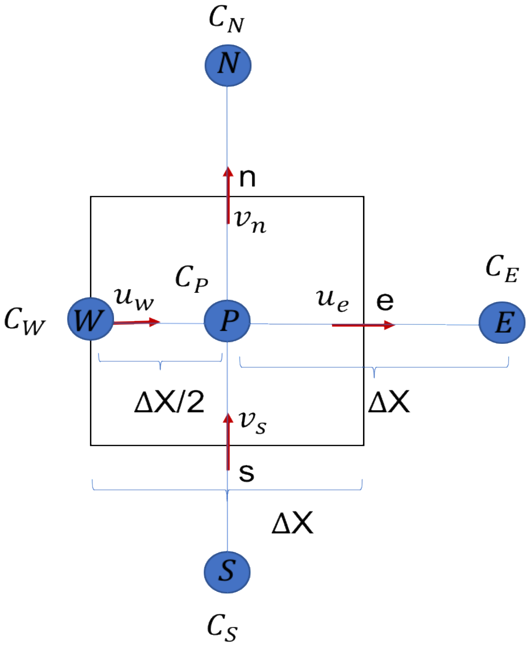

Figure A.3: West boundary control volume concentration and velocity point locations.

This formulation was applied to both the acid concentration and temperature solutions. Regarding the acid solution, Γ is the acid diffusion coefficient D_A, while for the temperature solution case, Γ is equal to $\frac{k}{\rho c_p}$.

A.3 Boundary Domain Discretization

In the previous section, the interior points were discretized. However, the boundary points had to be treated differently.

A.3.1 Inlet Boundary

At inlet, both the concentration and temperature are specified. Hence, no equations needed to be formulated. However, the discretized equation for the center point at the same grid block was modified as follows:

$$a_P C_P^{m+1} = a_E C_E^{m+1} + \ a_W C_i + a_N C_N^{m+1} + a_S C_S^{m+1} + b \tag{A.37}$$

The equation could then be rewritten as:

$$a_P C_P^{m+1} = a_E C_E^{m+1} \ + a_N C_N^{m+1} + a_S C_S^{m+1} + \grave{b} \tag{A.38}$$

where

$$\grave{b} = \ a_W C_i + b \tag{A.39}$$

The inlet for the temperature solution was treated similarly.

A.3.2 Wall Boundaries

Equations needed to be formulated and discretized for the wall boundaries. The acid concentration wall boundary condition was:

$$-D_A \frac{\partial C}{\partial \mathrm{y}}\bigg|_w = \mathrm{k_r}(C_w)^{\mathrm{n_r}}(1-\varphi) \tag{A.40}$$

This boundary condition is non-linear. The following was applied to linearize it:

$$(C_w^{m+1})^{\mathrm{n_r}} = (C_w^{m+1})^1 * (C_w^{m+1})^{\mathrm{n_r}-1} = (C_w^{m+1})^1 * (C_w^{m})^{\mathrm{n_r}-1} \tag{A.41}$$

The wall concentration was divided into explicit and implicit terms, where the non-linearity was transferred to the explicit term, making the boundary condition linear. According to Figure A.4, the discretized equation was written as:

$$\frac{-D_A(C_P^{m+1} - C_S^{m+1})}{\frac{\Delta \mathrm{y}}{2}} = \mathrm{k_r} C_P^{m+1}(C_P^m)^{(\mathrm{n_r}-1)}(1-\varphi) \tag{A.42}$$

The equation was then rearranged to obtain the following:

$$a_P C_P^{m+1} = a_S C_S^{m+1} \tag{A.43}$$

where

$$a_P = 1 + \frac{\mathrm{k_r}(C_P^m)^{(\mathrm{n_r}-1)}(1-\varphi)}{\frac{2D_A}{\Delta \mathrm{y}}} \tag{A.44}$$

$$a_s = 1 \tag{A.45}$$

The south wall boundary condition was treated similarly.

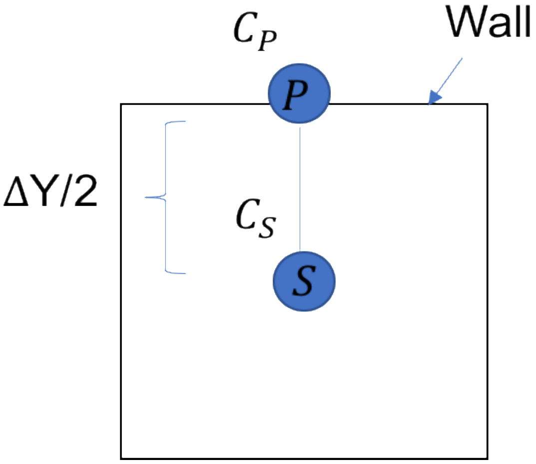

Figure A.4: North wall boundary control volume showing the concentration point locations.

The wall boundary condition for the temperature problem is linear as follows

$$-k\frac{\partial T}{\partial y}\bigg|_w = \beta + q_r(t) \tag{A.46}$$

where

$$\beta = |r * (\Delta H_r)| \tag{A.47}$$

The reservoir heat flux was written as:

$$q_r(t) = \alpha(T_R - T_W) \tag{A.48}$$

where

$$\alpha = \sqrt{\frac{(\rho_{ma}c_{ma}k_{ma})}{\pi t}} * \left[e^{-\xi^2} - \sqrt{\pi}\xi\, erfc(\xi)\right] \tag{A.49}$$

The boundary condition was discretized for the north wall boundary condition as follows:

$$\frac{-k(T_S^{m+1} - T_P^{m+1})}{\frac{\Delta \mathrm{y}}{2}} = \beta + \alpha(T_R - T_P^{m+1}) \tag{A.50}$$

The equation could then be written in this form:

$$a_P T_P^{m+1} = a_S T_S^{m+1} + b \tag{A.51}$$

where

$$a_P = \alpha + \frac{2k}{\Delta y} \tag{A.52}$$

$$a_S = \frac{2k}{\Delta y} \tag{A.53}$$

$$b = \beta + \alpha T_R \tag{A.54}$$

The south boundary condition was treated similarly.

A.3.3 Outlet Boundary

The acid and temperature gradients at the outlet were assumed to be zero. Hence, the boundary points were evaluated as follows:

$$C_P^{m+1} = C_W^{m+1} \tag{A.55}$$

For the center point at the outlet grid blocks (the point before the outlet point), the east coefficient was equal to zero, $a_E = 0$. The discretized equation was written as:

$$a_P C_P^{m+1} = a_W C_W^{m+1} + a_N C_N^{m+1} + a_S C_S^{m+1} + b \tag{A.56}$$

The outlet boundary points weren’t included in the matrix assembly because it did not affect the solution. Hence, to reduce the computation time, the outlet points were evaluated after inverting the matrix.

A.4 Matrix Assembly

The final step in solving any partial differential equation is assembling the discretized equation into matrix form. Then, the matrix can be solved using matrix inversion methods. In this model, MATLAB’s built-in backslash was used to invert the matrix. A matrix should be in the following form:

$$Ax = b \tag{A.57}$$

where A is the coefficient’s matrix, x is the unknown variables, and b is the constants. The matrix for this research was assembled assuming the grid deployment in Figure A.1. The matrix was made of 15 unknowns in this example, as the inlet was specified and the outlet could be calculated after solving the matrix. The assembly of the acid concentration problem is shown in Figure A.5, where the first and last three rows represent wall boundaries and the rest are interior points.

	A															x	b
	1	2	3	4	5	6	7	8	9	10	11	12	13	14	15		
1	a_{P1}			$-a_{N1}$												C_1	0
2		a_{P2}			$-a_{N2}$											C_2	0
3			a_{P3}			$-a_{N3}$										C_3	0
4	$-a_{S4}$			a_{P4}	$-a_{E4}$		$-a_{N4}$									C_4	$\grave{b}_4$
5		$-a_{S5}$		$-a_{W5}$	a_{P5}	$-a_{E5}$		$-a_{N5}$								C_5	b_5
6			$-a_{S6}$		$-a_{W6}$	a_{P6}			$-a_{N6}$							C_6	b_6
7				$-a_{S7}$			a_{P7}	$-a_{E7}$		$-a_{N7}$						C_7	$\grave{b}_7$
8					$-a_{S8}$		$-a_{W8}$	a_{P8}	$-a_{E8}$		$-a_{N8}$					C_8	b_8
9						$-a_{S9}$		$-a_{W9}$	a_{P9}			$-a_{N9}$				C_9	b_9
10							$-a_{S10}$			a_{P10}	$-a_{E10}$		$-a_{N10}$			C_{10}	$\grave{b}_{10}$
11								$-a_{S11}$		$-a_{W11}$	a_{P11}	$-a_{E11}$		$-a_{N11}$		C_{11}	b_{11}
12									$-a_{S12}$		$-a_{W12}$	a_{P12}			$-a_{N12}$	C_{12}	b_{12}
13										$-a_{S13}$			a_{P13}			C_{13}	0
14											$-a_{S14}$			a_{P14}		C_{14}	0
15												$-a_{S15}$			a_{P15}	C_{15}	0

Figure A.5: Matrix assembly for the acid concentration based on the grid deployment in Figure A.1.

APPENDIX B

ACID PENETRATION LENGTH ESTIMATION BY WELL TESTING METHODS

As illustrated in this study, an etching profile declining along the length is generated if a fracture in a calcite formation is treated with HCl acid. The curve's declining slope is a function of the acid system type, as straight acid shows the sharpest decline in slope. Fracture conductivity is a strong function of the etching profile, where the decline in fracture conductivity is sharper than the etched-width decline. The conventional well testing method has been found to under-predict the acid penetration length. Current well testing methods assume a uniform fracture conductivity, which is not a good assumption to make for acidized fractures.

A joined reservoir simulator was used to generate wellbore pressure data as a function of the production time, based on the variable fracture conductivity created by the acid model. Acid penetration length and conductivity were estimated from the linear and bilinear regimes of pressure diagnostic plots. After multiple cases were simulated, it was determined that the acid penetration length was consistently underestimated by 10% to 30%. The linear flow regime could not capture the low conductivity segment at the fracture end.

The etched-width profile in Figure B.1a, along with the corresponding conductivity distribution, were exported to the reservoir simulator. Bottomhole well pressure data were generated versus production time in a log-log scale (see Fig. B.2). The Figure shows both the early bilinear and later linear regimes. Fracture conductivity was calculated from the bilinear regime, as follows (Lee et al., 2003):

$$wk_f\sqrt{k} = \left(\frac{44.1qB\mu}{m_{bf}h}\right)^2\left(\frac{1}{\varphi\mu c_t}\right)^{0.5} \tag{B.1}$$

where

$$m_{bf} = 4\Delta\acute{p}_w/\sqrt[4]{\Delta t} \tag{B.2}$$

Acid penetration distance was calculated from the linear regime as follows:

$$x_f\sqrt{k} = \frac{4.064qB}{m_{lf}h}\left(\frac{\mu}{\varphi c_t}\right)^{0.5} \tag{B.3}$$

where

$$m_{lf} = 2\Delta\acute{p}_w/\sqrt{\Delta t} \tag{B.4}$$

The calculated acid penetration distance was around 206 ft, while the actual acid penetration distance from Figure B.1a was around 275 ft. In this case, well testing under-predicted the acid penetration distance by 25%.

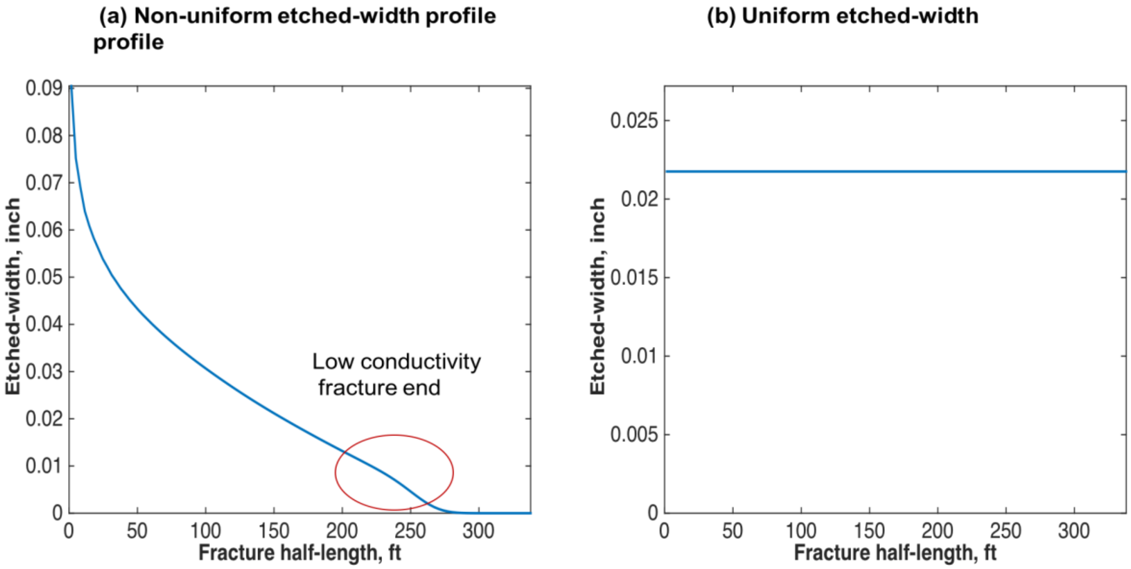

Figure B.1: Etched-with profile assuming uniform and non-uniform cases.

Another case was run where the fracture was assumed to have a uniform average etched-width along the entire fracture length, as shown in Figure B.1b. The uniform conductivity was 272 md.ft and the fracture half-length was 340 ft. Figure B.3 was used to calculate the fracture conductivity and acid penetration distance. The calculated fracture conductivity was 270 md.ft and the fracture half-length was 342 ft. The calculated values precisely matched the case exported to the reservoir simulator. Conventional well testing methods were determined to be accurate when predicting fracture half-length and conductivity in uniform conductivity fractures. For extremely non-uniform fracture conductivity (such as acid fractures), conventional well testing methods consistently underestimated the acid penetration distance.

Table B.1: Input Data for Calculating Fracture Half-length and Conductivity

Input	**Value**	**Unit**
Oil viscosity, μ	0.8	cp
Production rate, q	100	STB/d
Formation volume factor, B	1.3	Res.bbl/STB
Pay zone thickness, h	120	ft
Porosity, φ	0.1	
Total compressibility, c_t	0.00000156	1/psi
Reservoir permeability, k	0.1	md

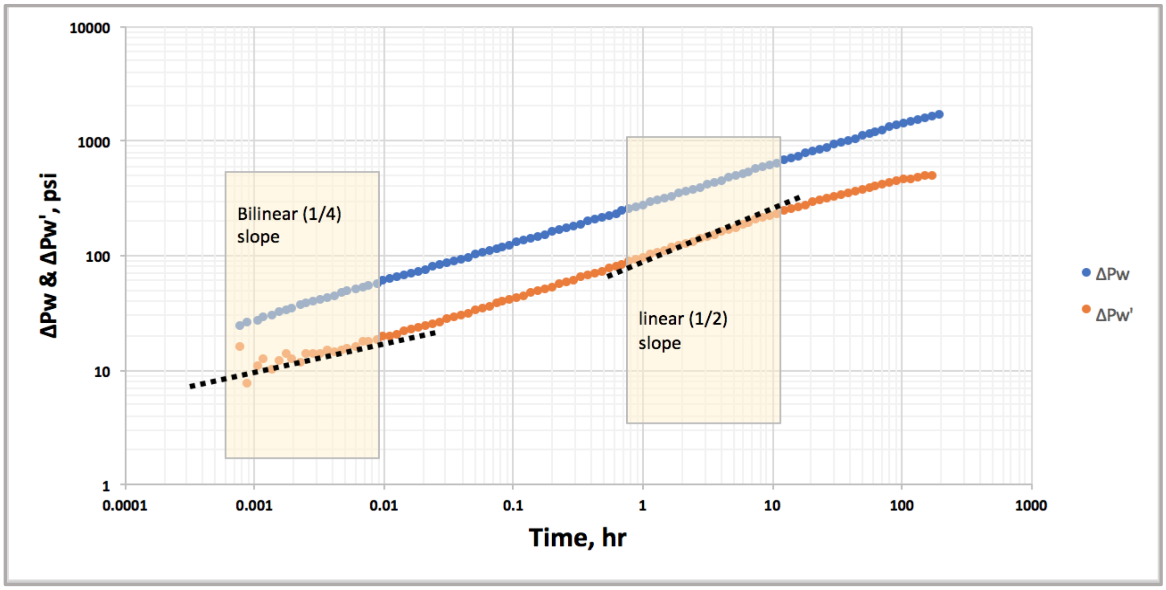

Figure B.2: Pressure drawdown test for a non-uniform fracture conductivity profile.

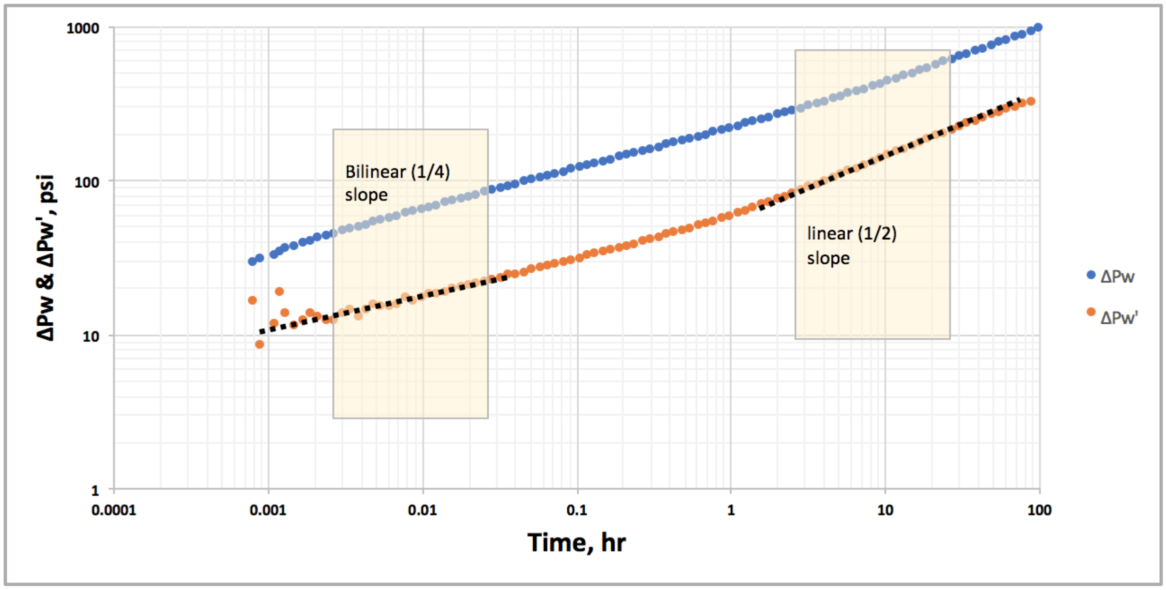

Figure B.3: Pressure drawdown test for a uniform fracture conductivity profile.